Growth Kinetics of Self-assembled Structures of Perylene and Naphthalene Derivatives by Thermal Evaporation and Their Characterizations

A Thesis Submitted to

Indian Institute of Technology Guwahati

For the Degree of

Doctor of Philosophy

By

Arindam Pal

Department of Physics

Indian Institute of Technology Guwahati

Guwahati-781039, India

October 2012

TH-1132_08612114

Dedicated To

……*My Beloved Parents*

TH-1132_08612114

STATEMENT

This work contained in this thesis "**Growth Kinetics of Self-assembled Structures of Perylene and Naphthalene Derivatives by Thermal Evaporation and Their Characterizations**" has been carried out by me at Indian Institute of Technology Guwahati under the supervision of Dr. D. K. Goswami, Associate Professor, Department of Physics, Indian Institute of Technology Guwahati. This work has not been submitted elsewhere for the award of any degree.

Arindam Pal

Senior Research Scholar

Department of Physics

Indian Institute of Technology Guwahati

Guwahati-781039, Assam

TH-1132_08612114

DR. DIPAK KUMAR GOSWAMI
Associate Professor
Tel: +91-361-258-2722
Fax: +91-361-258-2749 / 2690762
Email: dkg@iitg.ernet.in

भारतीय प्रौद्योगिकी संस्थान गुवाहाटी
INDIAN INSTITUTE OF TECHNOLOGY GUWAHATI
Department of Physics
Guwahati – 781039, Assam

CERTIFICATE

This is to certify that the thesis entitled "Growth Kinetics of Self-Assembled Structures of Perelyne and Naphthalene Derivatives by Thermal Evaporation and Their Characterizations" which is being submitted by Arindam Pal in partial fulfillment of the degree of Doctor of Philosophy in Science (Physics) of Indian Institute of Technology Guwahati, Guwahati is a record of his own research work carried out by him. He has carried out his investigations for the last four years on the subject matter of the thesis under my guidance at Indian Institute of Technology Guwahati, Guwahati. The matter embodied in the thesis has not been submitted for the award of any other degree by him or by anybody else.

Dr. Dipak Kumar Goswami
Indian Institute of Technology Guwahati
Guwahati

TH-1132_08612114

TH-1132_08612114

ACKNOWLEDGEMENT

The research reported here is the result of years of hard work and it is not possible without the help of numerous people. It is the time for showing gratitude to those persons for their help and support.

Firstly I would like to express my deep gratitude to my thesis supervisor Dr. D. K. Goswami for his constant support, encouragement and guidance during these years. I am sincerely indebted to him for accepting me as PhD student. During these years of work I have learned a lot from him. My discussions with him not only help me to solve any problem in work, but also help me a lot to understand the physics behind the phenomenon. I wish to thank him for giving me total freedom in my work to achieve the goal. I am grateful to you for introducing me to the MBE community and providing me the opportunity to be a part of this community.

I would like to thank my Doctoral Committee members, Prof. P.K. Giri (Chairman), Dr. D. Pal and Dr. P. K. Iyer for their review of my work and their constructive criticism and valuable suggestions. Especially Prof. P. K. Giri because of some of the cases I have taken his lab facility.

Next I am thankful to Prof B. N. Dev for his invaluable support in research. Because of him I can use MBE and be a part of MBE community. He helps me with his valuable discussion in my research work.

I would like to thank Dr S. S. Bag and Dr. P. K. Iyer for providing me synthesized and purified organic molecule whatever I deposited in my research work.

I am also thankful to our Head of the Department and other faculty members of Physics, members of Central Instruments Facilities and Center for Nanotechnology for providing a research friendly atmosphere with up–

TH-1132_08612114

to–date research facilities. I am grateful to Indian Institute of Technology Guwahati for providing the fellowship and such a good accommodation in this beautiful campus. A special thanks to the scientific officers, Dr. Sidananda Sarma, Indrajit Talukdar, Kaustubh Acharya, Kula K. Senapati, Chandan Borgohain and Madhurjya Borah for their help and co-operation to complete my work. I am also thankful to Central Workshop, Department of Mechanical Engineering for the fabrication of essential components used in my experimental setup.

I would like to express my appreciation and thanks to my friends and lab-mates for their helps and good company. I should mention one of my close friend, Soumen for the enjoyable company since my university days. He is always helpful for any kind of work or any discussion about Physics. He helps me a lot for lot of experimental work. I am very much thankful to my juniors Murali and Subbrao for their help in different experimental work. I would thankful to Ramesh for his jolly and enjoyable company.

It is my pleasant duty to acknowledge the help provided by my senior and juniors in IACS especially Rajib Da, Jagadish and Debolina. They help me a lot to understand the operation of MBE and STM.

Finally I wish to express my deep sense of gratitude to my father and mother for their love, blessing and constant encouragement to pursue higher study. I would like to thank to my brother because every time and in every point of my life he encourage me and help me to take right decision. This thesis dedicated to my parents and brother.

Arindam Pal

IIT Guwahati

TH-1132_08612114

CONTENTS

Synopsis……………………………………………………… VII

List of Publications………………………………………….. XVI

Chapter I: **Introduction**……………………………………… 1

1.1 Organic Semiconductors.. 1

1.2 Fundamental of Thin Film Growth................................. 3

1.2.1 Inorganic Thin Film Growth.................................. 3

1.2.2 Organic Thin Film Growth..................................... 6

1.3 Organic Molecules.. 10

1.4 References... 13

Chapter II: **Experimental techniques and data analysis…….** 17

2.1 Growth Techniques of self-assembled

Organic Structures……………………………………. 18

2.1.1 Substrate Preparation ……………………………… 18

2.1.2 Thin Film Growth Techniques………………….... 18

2.1.3 Evaporation of organic molecules………………....22

2.2 Characterization Techniques…………………………..24

2.2.1 Structural Characterizations…………………………24

A. Scanning Tunneling Microscopy (STM)…………....24

B. Atomic Force Microscopy (AFM)……………….... 27

C. X-ray Scattering……………...…………………..… 30

D. Field-Emission Scanning Electron Microscopy…..... 36

E. Transmission Electron Microscopy……………..…. 37

2.2.2 Spectroscopic Measurements……………….………38

A. UV-Vis Spectroscopy………………………………39

TH-1132_08612114

B. Photoluminescence Spectroscopy…………………….…. 39

C. Time–Resolved Photoluminescence Spectroscopy….41

2.3 Designing and development of photocurrent and

photoresponse measurement setup…………………… 42

2.4 Statistical analysis of rough surfaces…………………..43

2.4.1 Calculation of correlation functions

from AFM images…………………………………....46

2.5 References…………………………………………… 49

Chapter III: **Growth of TC-PTCDI-C_8 films on SiO_2 surface.** 53

3.1 Introduction………………………………………………53

3.2 Experimental…………………………………………... 55

3.3 Results and Discussions ………………………………56

3.3.1 RT Growth of TC-PTCDI-C_8 on SiO_2

substrate at room temperature……………………... 56

A. AFM Results………………………………….. 56

B. X-ray reflectivity Results……………………… 56

3.3.2 Growth of TC-PTCDI-C_8 on SiO_2

substrate at 75°C substrate temperature…………… 58

A. AFM Results………………………………….. 58

B. X-ray reflectivity Result……………………… 60

C. Statistical Analysis of Surface Morphology….. 65

3.4 Conclusions…………………………………………… 69

3.5 References………………………………………….... 71

TH-1132_08612114

Chapter IV: **Growth of flat top Ag mounds on Si(111)-(7×7) reconstructed surfaces**………… 75

4.1 Introduction……………………………………………….75

4.2 Experimental…………………………………………... 77

4.2.1 Clean Surfaces of Silicon………………………….. 77

4.2.2 Si(111) surface reconstruction…………………….. 78

4.2.3 Growth of Ag on Si……………………………….... 79

4.3 Results and Discussions………………………………. 80

4.3.1 Morphological Analysis…………………………… 80

4.3.2 Statistical analysis of surface morphology………… 82

4.4 Conclusions…………………………………………… 89

4.5 References…………………………………………….....91

Chapter V: **PTCDI-Ph on SiO2 Surfaces: Growth of long molecular terraces**……………………….. 95

5.1 Introduction…………………………………………….95

5.2 Experimental…………………………………………... 96

5.3 Results and Discussions………………………………..97

5.3.1 Studies of surface morphology…………………… 97

5.3.2 Structural Characterizations……………………….101

5.3.3 Optical Characterizations………………………… 103

A. Absorption property……………………………….....103

B. Photoluminescence properties……………………... 104

C. Time-Resolved Photoluminescence properties……..106

5.3.4 Photoresponse of Molecular Terraces……………..108

TH-1132_08612114

5.4 Conclusions ………………………………………….. 111

5.5 References……………………………………...113

Chapter VI: **Self-assembled growth of organic ribbons**…….. 115

6.1 Introduction……………………………………………115

6.2 Experimental Details ………………………………... 115

6.3 Results and Discussions ……………………………116

6.3.1 Study of morphology………………………….... 116

6.3.2 Optical characterizations………………………..121

6.4 Conclusions ……………………………………….....129

6.5 References ……………………………………………131

Chapter VII: **Summery and Conclusions**……………………. 133

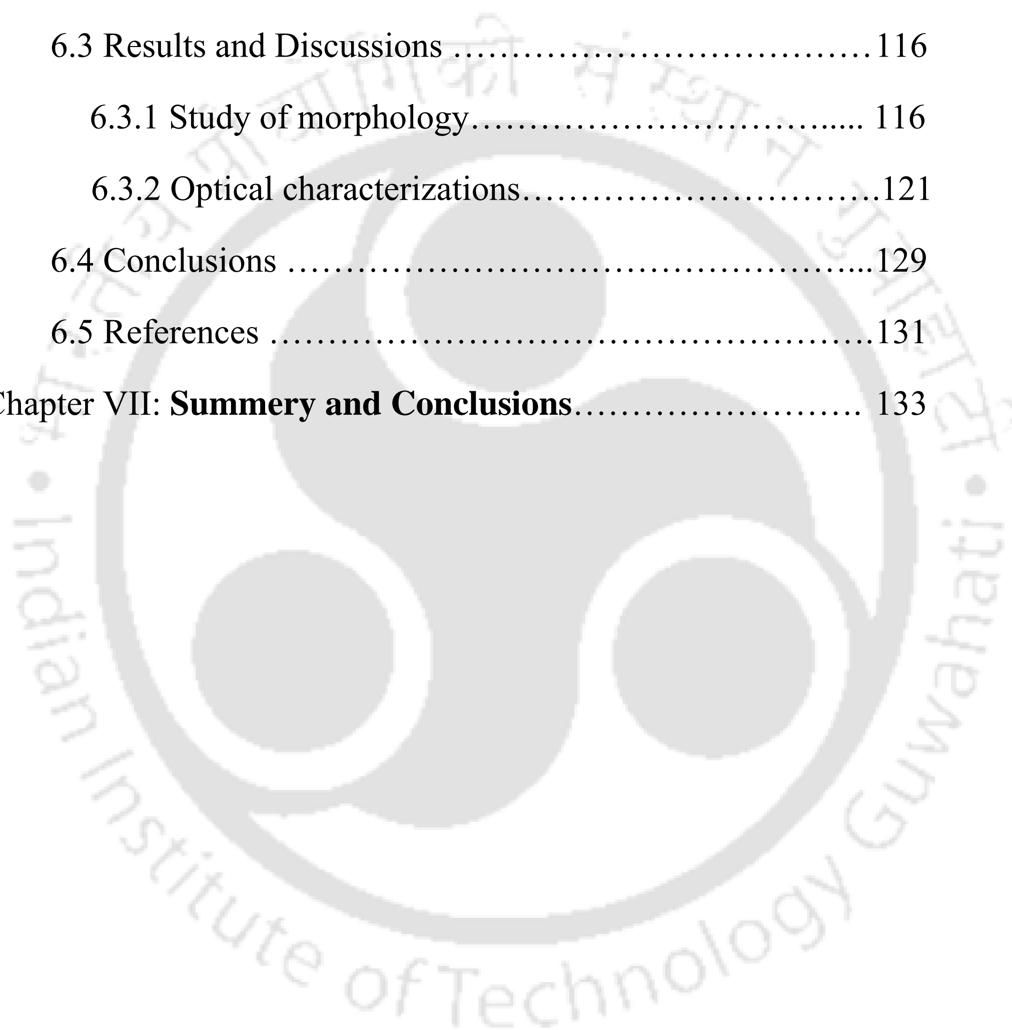

TH-1132_08612114

Synopsis

Introduction:

Self-assembled growth of thin films is an essential part of modern device fabrication. It is desirable to have an ability to control morphology of micro / nanostructures to meet functional requirements of the devices designed using such structures. Understanding of growth kinetics, therefore, is very crucial in advancing the modern technology. Nevertheless, there are lots of challenging fundamental issues related to growth of these structures, which need to be explored further and therefore, receiving significant attentions form the many researchers during last few decades.[1-4] In deposition processes, atoms or molecules impinge randomly on the substrate that supplies thermal energy to the adsorbed species. The supplied thermal energy is sufficient enough to allow adsorbed species to diffuse across the terraces on the substrate and subsequently arrange or organize themselves into different surface structures stabilized by attractive interactions. Continued deposition can produce complicated submonolayer patterns and multilayer morphologies in the form of mounds, wire, ribbons, films etc. The main atomic processes during the growth include a variety of distinct diffusion processes including diffusion on a flat terrace, attachment to an existing island, detachment from the island edges and interlayer diffusion.[2,5-7] The relative rates of occurrence of these processes primarily are controlled by the deposition rate and substrate temperature (T_{sub}). Substrate temperature activates kinetic processes by dictating the migration rate. Sometimes, diffusion processes at island edges are also inhibited because of additional barrier (Ehrlich - Schwoebel (ES) barrier).[5] Therefore, limited

TH-1132_08612114

diffusion to downward and interlayer mass transport results kinetically rough surfaces than smooth films.[8] Strain effects also often dominate the quasi-equilibrated morphology of growing films. As a result of such restricted diffusions, formation of 3D mounds (multilayer stack of 2D islands), unidirectional growth forming wires, ribbons or ribbon like long terraces are observed. This thesis work includes the studies of growth of Perylene and Naphthalene derivatives grown on SiO_2 substrates. Ag growth on Si(111)-(7×7) substrates has been considered as a system that also form flat-top mounds as observed in case of growth of perylene derivative. This is to compare the two systems which form similar surface morphology. SiO_2 layer is most commonly used gate oxide layer for microelectronics. Therefore, we have used this as our substrate of interest for this thesis work.

Perylene and Naphthalene derivatives are known to exhibit interesting electrical and optical properties. In most of these compounds, the perylene or naphthalene units act as electron-acceptors. Remarkably, the perylene unit by itself is also known as one of the earliest donors used in the preparation of highly conducting organic solids. Therefore, these molecules show promises to be competitive candidates to existing devices based on inorganic semiconductors.[9, 10] However, the growth of such molecular thin films is very complicated due to their poor van der Waal interactions between molecules and therefore, issues like epitaxy, strain, which are well defined in case of inorganic growth, are not defined properly. As a result, growth of these molecules form different kind of surface morphologies such as mounds, wires, ribbons or ribbons like growth of flat terraces. In this thesis, we have chosen two derivatives of perylenediiamide derivatives (TC-PTCDI-C_8 and PTCDI-Ph), which form flat-top mounds and ribbon like long terraces on SiO_2 substrates, respectively. 4 - (4-n, n-dimethylaminopheny lethynyl) – n - (2-propynyl) - 1, 8 napthalimide ($^{4\text{-DMAPE}}$NI) form nano-

TH-1132_08612114

ribbon like unidirectional structures. In order to understand the growth of flat-top organic mounds, we have also studied the growth of Ag on Si(111)-(7x7) surfaces which grow flat-top mounds. Though, growth mechanism and kinetics of the growth of TC-PTCDI-C_8 and Ag on Silicon surfaces are different, they form similar surface morphologies.

We have explored self-assembled growth of three different kinds of surface morphologies controlled by diffusion of the molecules. First case is the formation of 3D mounds, which are essentially multilayers stacks of 2D islands. TC-PTCDI-C_8 molecules are grown on SiO_2 substrates at 75° substrate temperature. These molecules grow 2 molecular layers as layer-by-layer and then form flat top 3D mounds. We have studied the growth from sub-monolayer to a thick film growth. Growth kinetics of forming 2D layer to 3D mound formation is explored. Height dependent step edge (ES) barrier is very common for the growth of organic semiconductor thin film growth. As a result, downward mass transport becomes restricted with coverages. This leads to form flat-top mounds of TC-PTCDI-C_8. In case of TC-PTCDI-C_8, we have observed stationary to non-stationary growth transition in the growth kinetics that corresponds to evolution form 2D wetting layer to 3D flat-top mounds formation.[11-13]

In order to understand the insight of the flat-top mound growth in inorganic system, in-spite of different growth mechanism, we have chosen to study the growth kinetics of Ag on Si(111)-(7×7) surfaces. Ag forms flat top mounds with two atomic layers preferences at the initial stages of the growth.[14] These mounds eventually grow laterally maintaining height preferences and coalesce to form percolated mounds with even (two, four … etc) atomic layers preferences.[15] This growth mechanism has been reported as electronic growth as the prefer heights essentially depends on the formation of quantum well states (QWSs) within the metal films grown on

TH-1132_08612114

semiconductors surfaces.[14,16,17] As a result, it is expected from the theoretical prediction that electronic growth can form smooth films.[17-19] However, no smooth films observed for the Ag grown on Si(111)-(7×7) surfaces at room temperature within our wide range of explored coverages. The detail growth mechanisms are studied from one monolayer to a thick film growth. Though, growth mechanisms of forming flat-top mounds are different for organic (TC-PTCDI-C_8) and inorganic (Ag/Si(111)-(7×7)) systems but they form similar kind of surface morphologies. We have found out the lateral and vertical growth rates of the mounds are comparable for both the system and follow a linear behavior with similar slope.

In the second part of thesis work, we have studied the growth of unidirectional structures like ribbons and flat long ribbon like terraces of organic materials. Two different molecules were selected for the growth based on their structure and chemical composition. PTCDI-Ph grows as ribbon like long flat terraces, however, $^{4\text{-DMAPE}}$NI forms ribbons. Both the molecules were synthesized and cleaned before thermal evaporation to grow films. N,N'-di-phenyl perylenetetracarboxylicdiimide (PTCDI-Ph) on SiO_2 substrates. Room temperature growth does not show any ordering of the films. However, unidirectional film growth forming long ribbon like terraces is observed for the films grown at elevated substrate temperatures (T_{sub} = 80°C, 90°C, 120°C, 140°C). Higher substrate temperature essentially activates the surface diffusion that increases with temperature. Therefore, mass transport to form the terraces can be controlled by controlling substrate temperature. We have calculated the surface diffusion activation energy for PTCDI-Ph molecules from the Arrhenius plot. The activation energy along the length (E_D=0.21eV) is relatively smaller than that of along the width (E_D=0.34eV). This explains the unidirectional growth of the structures. From x-ray reflectivity measurements, we have calculated the interlayer spacing of

TH-1132_08612114

the films, which clearly revealed that the molecular tilt angle with surface normal within the film.

In the last part of the thesis we studied the growth of $^{4\text{-DMAPE}}$NI molecules on SiO_2 surfaces. These molecules can be stacked with $\pi-\pi$ and CH-π interactions along one direction and therefore form organic ribbons. However, interactions on the other direction are not so strong to continue growth after a constant width. The lengths of the wires are increased at one end with the substrate temperatures keeping other end grounded at substrates. The maximum length that we observed is about 8 μm. However, the diameters of the wires were essentially constant during the growth. As a result, masses were transferred to the edges of the wires with increasing substrate temperatures. We have calculated the surface diffusion activation energy (E_D=0.21eV) for these molecules from Arrhenius plot.[20] These ribbons show huge persistent current observed over 14 hours duration. The origin of the persistent photo current is because of the formation of deep level surface states during growth.[21-23] These states capture huge number of free electrons in presence of light and slowly release the electrons.[24] Therefore, the molecules shows promise to be very good candidate for optoelectronic applications.[25-27]

In conclusion, we have extensively studied the growth of mounds and ribbon like structures formation for perelyne and naphthalene derivatives on SiO_2 surfaces with different substrate temperatures. Essentially, we found out that the growth of such structures depends on the diffusion of the molecules. The growth temperature broadly controls the diffusion and this parameter has been varied to study the growth kinetics for organic systems. Packing within the films and therefore, the growth front morphologies depend on the molecular properties as well as the growth temperature. However, for Ag, it depends on the quantum well state formation within the

TH-1132_08612114

layer as per electronic growth mode. We also have studied the structural, electrical and optical properties of some of the self-assembled structures in this thesis. Ribbon structure of $^{4\text{-DMAPE}}$NI molecules showed huge photocurrent, which persist up to 14 hours. These structures show promises to be good candidate for optoelectronic devices.

The complete thesis work has been organized into seven chapters as described below:

Chapter 1 presents the brief introduction of the development of 1D, 2D and 3D surface structures formation. In addition, fundamental issues related to the growth of mounds and ribbons like structures are discussed. Possible applications and importance of the growth of these structures are highlighted.

Chapter 2 provides brief description of facility development and the experimental techniques used in this thesis work along with their working principles. The basic in-house facilities development such as Knudsen cell for the evaporation of the organic molecules to grow films and the photoelectric property measurement system are presented.

Chapter 3 presents the results of growth of TC-PTCDI-C_8 molecules on SiO_2 substrates. Detail investigations of growth from sub-monolayer to a thick film (0.75ML, 1.5ML, 3.2ML and 8.5ML) growth are described. Here, monolayer (ML) is defined as the amount of materials to grow a complete layer. Atomic force microscopy (AFM) and X-ray reflectivity (XRR) studies revealed the detail growth kinetics of mound formation. The observed thickness of wetting layer has been found to be 2ML. Structural characterization of the mounds are determined by X-ray diffraction (XRD) and discussed.

TH-1132_08612114

Chapter 4 presents the growth of Ag on Si(111)-(7×7) reconstructed surfaces for the different coverages. In addition, statistical characterization of surface morphology for the samples is presented. Different scaling exponents for electronic growth of Ag has also been reported.

Chapter 5 presents the results of the growth of PTCDI-Ph grown on SiO_2 substrate. We reported the formation of ribbon like flat-terraces. The mechanism of such structure formation is also proposed. Results obtained form optical and electrical characterization are presented.

Chapter 6 presents the results of growth study of a $^{4\text{-DMAPE}}$NI on SiO_2 surfaces that form ribbon like structures. We have calculated activation energy of diffusion using Arrhenius plot. The results of various optical and electrical characterizations of these ribbons are reported. The optical band gap (2.53eV) of this material is calculated from the UV-absorption study which satisfy theoretical value obtained from density functional theory (DFT) calculation. The luminescence property of the material studied elaborately and reported in this chapter.

Chapter 7 presents the summary and important conclusions of these works. In addition, highlights the new findings and results related to the formation of flat top mound and ribbon like structures are reported. Open questions and the different directions of future studies are addressed.

TH-1132_08612114

References:

[1] A. C. Durr, F. Schreiber, K. A. Ritley, V. Kruppa, J. Krug, H. Dosch, and B. Struth, Phys. Rev. Lett. **90** (2003).

[2] X. N. Zhang, E. Barrena, D. K. Goswami, D. G. de Oteyza, C. Weis, and H. Dosch, Phys. Rev. Lett. **103** (2009).

[3] R. T. Weitz, et al., J. Am. Chem. Soc. **130**, 4637 (2008).

[4] Y. Wakayama, R. Hayakawa, X. N. Zhang, H. Dosch, N. Hiroshiba, and T. Chikyow, J Phys Chem C **113**, 2197 (2009).

[5] Z. Zhang and M. G. L. , Science **276**, 377 (1997).

[6] J. W. Evans, P. A. Thiel, and M. C. Bartelt, Surf. Sci. Rep **61**, 1 (2006).

[7] P. P. Gregor Hlawacek, Paul Frank, Adolf Winkler,Claudia Ambrosch-Draxl, Christian Teichert, Science (2008).

[8] D. Y. Zhong, M. Hirtz, W. C. Wang, R. F. Dou, L. F. Chi, and H. Fuchs, Phys. Rev. B **77**, 113404 (2008).

[9] D. Shukla, S. F. Nelson, D. C. Freeman, M. Rajeswaran, W. G. Ahearn, D. M. Meyer, and J. T. Carey, Chem. Mater. **20**, 7487 (2008).

[10] H. Sirringhaus, R. H. Friend, X. C. Li, S. C. Moratti, A. B. Holmes, and N. Feeder, Appl. Phys. Lett. **71**, 3871 (1997).

[11] J. H. Jeffries, J. Zuo, and M. M. Craig, Physical review letters **76**, 4931 (1996).

[12] J. Lapujoulade, Surf Sci Rep **20**, 191 (1994).

[13] M. Pelliccione and T.-M. Lu, *Evolution of thin film morphology: modeling and simulation* (Springer-Verlag, New York, 2008).

[14] L. Gavioli, K. R. Kimberlin, M. C. Tringides, J. F. Wendelken, and Z. Zhang, Phys. Rev. Lett. **82**, 129 (1999).

[15] D. K. Goswami, K. Bhattacharjee, B. Satpati, S. Roy, P. V. Satyam, and B. N. Dev, Surf. Sci. **601** 603 (2007).

TH-1132_08612114

[16] S. J. Tang, C. Y. Lee, C. C. Huang, T. R. Chang, C. M. Cheng, K. D. Tsuei, H. T. Jeng, V. Yeh, and T. C. Chiang, Phys. Rev. Lett. **107**, 066802 (2011).

[17] Z. Y. Zhang, Q. Niu, and C. K. Shih, Phys. Rev. Lett. **80**, 5381 (1998).

[18] Z. G. Suo and Z. Y. Zhang, Phys. Rev. B **58**, 5116 (1998).

[19] A. L. Wachs, T. Miller, and P. R. T.-C. Chiang, B33 (1986) 8870, Phys. Rev. B **33**, 8870 (1986).

[20] N. I. Craciun, J. Wildeman, and P. W. M. Blom, Phys. Rev. Lett. **100**, 056601 (2008).

[21] A. Thander and B. Mallik, Solid State Comm. **121**, 159 (2002).

[22] S. Karan, D. Basak, and B. Mallik, Current Appl. Phys. **10**, 1117 (2010).

[23] G. J. Hu, L. Zhang, N. Dai, L. Y. Chen, and M. C. Tamargo, Solid State Comm. **111**, 631 (1999).

[24] H. K. Yadav, K. Sreenivas, and V. Gupta, Appl. Phys. Lett. **96**, 223507 (2010).

[25] T. Thio, R. A. Linke, G. E. Devlin, J. W. Bennett, and J. D. Chadi, Appl. Phys. Lett. **65**, 1802 (1994).

[26] R. A. Linke, T. Thio, J. D. Chadi, and G. E. Devlin, Appl. Phys. Lett. **65**, 16 (1994).

[27] R. L. MacDonald, R. A. Linke, J. D. Chadi, T. Thio, G. E. Devlin, and P. Becla, Optics Lett. **19**, 2131 (1994).

TH-1132_08612114

List of Publications

In Peer-Reviewed Journals

1. D.K.Goswami and **A. Pal** , *"Dynamics of Ag growth on Si(111)-7x7 surfaces: A scaling Study",* **Int. J. Nanoscience**,10,123-127 (2011) .

2. **Arindam Pal**, J.C.Mahato, B.N.Dev & D.K.Goswami, "*Kinetic roughening in electronic growth of Ag on Si(111)-(7x7) surfaces*" **AIP Advance**(UnderReview).

3. Arindam Pal and D. K. Goswami, "*Self-assembled TC-PTCDI-C_8 flat-top mounds growth on SiO_2 surfaces*" **J. Phys. Chem. C** (Under review)

4. **Arindam Pal**, R. Kundu, B. Satpati, S. S. Bag and D. K. Goswami, "*Persistence in photoconductivity and opto-electronic property of self-assembled growth of organic nanowires by molecular beam deposition*",**J. Phys. Chem. C** (Under review).

5. **Arindam Pal**, G. Murali, V. Suresh, A.Kalita, P.K.Iyer, D.K.Goswami, "*Unidirectional growth of PTCDI-Ph on SiO_2 surfaces*" **J. Appl. Phys**. (Under review)

6. **Arindam Pal,** Samiran Pramanik and D. K. Goswami "*Growth dynamics of sub-monolayer Ag on Si(111)-(7x7) surfaces: A RHEED study*", (Phys. Rev. B, To be communicated).

Conference Presentations

1. D.K.Goswami and **A. Pal** ,*"Dynamics of Ag growth on Si(111)-7x7 surfaces: A scaling Study",* International Conference on Advanced Nanomaterials and Nanotechnology-09, December 9-11,2009 IIT Guwahati, India.

2. D.K.Goswami and **A. Pal,** *"Growth of Ag on Si(111)-7x7 Surfaces: Scaling Studyc"* 54th DAE Solid State Physics Symposia (DAE-2009), December 14-18,2009 Baroda .

TH-1132_08612114

3. **A. Pal**, R. Kundu, S. S. Bag and D.K.Goswami ,"*Self-assembled organic nanowires growth by organic molecular beam deposition*"International Conference on Fundamental & Applications of Nano science & Technology(ICFANT-2010), December 9-11, Jadavpur University

4. **Arindam Pal**, R. Kundu, S. S. Bag and D. K. Goswami ,"Self-assembled growth of organic nanowires and their characterization"International Conference on Advanced Nanomaterials and Nanotechnology-11, December 8-10, 2011, IIT Guwahati, India.

5. **Arindam Pal**, R. Kundu, S. S. Bag and D. K. Goswami, "*Large persistent photocurrent in organic nanowires*" International Conference on Advanced Nanomaterials and Nanotechnology-11, December 8-10, 2011, IIT Guwahati, India.

6. **Arindam Pal**, G. Murali, P. Anand Kumar, and D.K.Goswami,"*Kinetics of flat top organic nanostructure growth*" International Conference on Advanced Nanomaterials and Nanotechnology-11, December 8-10, 2011, IIT Guwahati, India.

7. **Arindam Pal,** J. C. Mahato, Debolina Das, B. N. Dev and D.K.Goswami, "*Dynamic scaling study of percolated Ag nanostructures*" International Conference on Nanoscience and Technology (**ICONSAT–2012**), February 20-23, 2012, Hyderabad, India

8. G.murali, **Arindam Pal** and D.K. Goswami, "*Study of growth of organic thin films by X-ray reflectivity measurements*" (**SXNS-12**) 12th International Conference on Surface X-ray and Neutron Scattering, July 25-28, 2012, Kolkata, India

9. **Arindam Pal**, R. Kundu, S. S. Bag and D. K. Goswami, " *Temperature dependent persistent photocurrent in organic nanoribbon*" 4th International Conference on Advance Materials (AMN-2012), October 17-19, 2012, Chennai, India

10. **Arindam Pal**, G. Murali, V. Suresh, P. K. Iyer and D.K.Goswami, " *Effect of temperature on the molecular arrangement of organic nanostructure*

TH-1132_08612114

growth" 4th International Conference on Advance Materials (AMN-2012), October 17-19, 2012, Chennai, India

Workshop Attended

1. " *Organic Electronic 2010"* Summer course supported by Samtel Center for Display Technologies, IIT Kanpur, July 5-10, 2010

2. "INUP Familiarization Workshop" , IIT Guwahati, September 28-29, 2012,

TH-1132_08612114

TH-1132_08612114

Chapter I

Introduction

In this thesis, we have substantially studied the growth kinetics of different kinds of surface structures formation of organic and inorganic materials. Here we focus on organic molecules with semiconducting properties and mechanisms of growth with kinetics of the growth of films are discussed. A review of basic concepts of organic semiconductors and the semiconductors investigated in this work are given. We also summarize the main processes involved in thin film growth from the vapor deposition and the influence of the growth parameters.

1.1 Organic Semiconductors

Organic semiconductors are materials based on molecules containing carbon compounds. They only become conductors of electric current when excess charge carriers are either produced by the internal photo effect or are injected by applied voltages. Their semiconducting properties are attributed to the conjugated π-electron systems in their skeletal structures which is a consequence of sp^2 hybridization of the carbon atoms: the p_x and p_y orbital are forming together with the s orbital the σ bonds and are localized between the carbon bonding atoms. The p_z orbitals of adjacent atoms, however,

TH-1132_08612114

overlap perpendicular to the plane of the sp^2 orbitals and form an additional bond, the π bond as illustrated in Fig.1.1. Due to the weak contribution of the π electrons to bonding of the molecule, the conjugated π-electron system exhibits electronic excitation energies in the range of only a few eV and is therefore responsible for the optoelectronic properties of organic semiconductors.[1] In contrast to inorganic semiconductors, where the band

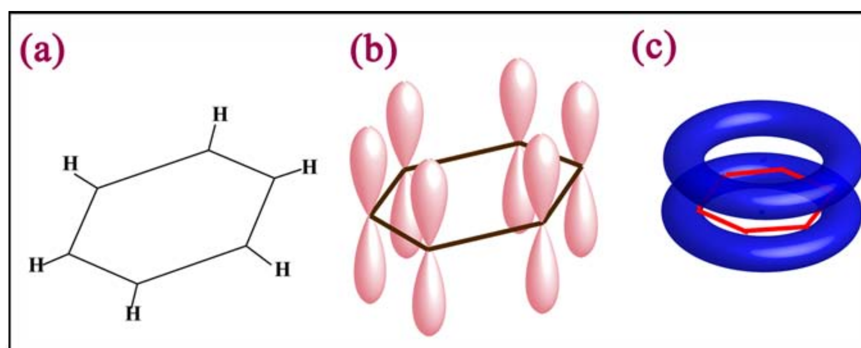

Fig. 1.1: (a)The σ bond of Benzene, (b) P_z-orbital of each carbon atom, and (c) The resulting electron cloud of ¼ electrons above and below the plane of the benzene ring.[2]

gap extends between valence and conduction band, is the gap in organic semiconductors determined by the difference between the highest occupied molecular orbital (HOMO) and the lowest unoccupied molecular orbital (LUMO). This band gap can be varied to a certain extent by synthesizing diverse molecules which differ in size, atomic arrangement and functional groups in order to tune their electronic properties.[2-10]

Basically, organic semiconducting molecules can be classified into two main groups: polymers and oligomers. Polymers are long flexible molecules which are characterized by the formation of unbounded repetitive molecular units. Oligomers or small weight organic molecules consist of a finite number of monomer units thus leading to a well defined mass (in contrast to polymers). Both, polymers and oligomers show similar electronic and optical properties with typical energy band gaps between 1.5 eV to 2.6 eV. The major difference is found in the thin film deposition techniques and

in the resulting structural properties. Polymers can be easily processed from solution which decreases the production costs dramatically. Oligomers, however, are very often insoluble and thermal evaporation are required to grow the films. Nevertheless, oligomers have the crucial advantage over polymers that they allow the preparation of very well ordered films of high purity and crystalline order, which are fundamental prerequisites to enhance charge carrier mobility.[11, 12]

1.2 Fundamental of Thin Film Growth

1.2.1 Inorganic Thin Film Growth

When a film is grown on substrate by various methods, the film may be amorphous, polycrystalline or single crystalline depending upon substrates, substrate temperature, materials of the film and method of deposition. There are three types of conventional growth modes in epitaxial growth of inorganic film depending on surface free energies of the over layer and substrate and their lattice misfit. These established growth modes are (a) Frank-van der Merwe (FM) or layer by layer growth[13](b) Volmer-Weber[14] (VW) or island growth and (c) Stranski-Krastanov[15] (SK) or layer-plus-island growth. The schematic presentation of these growth mechanism are shown in Fig 1.2 (a), (b) and (c) respectively.

TH-1132_08612114

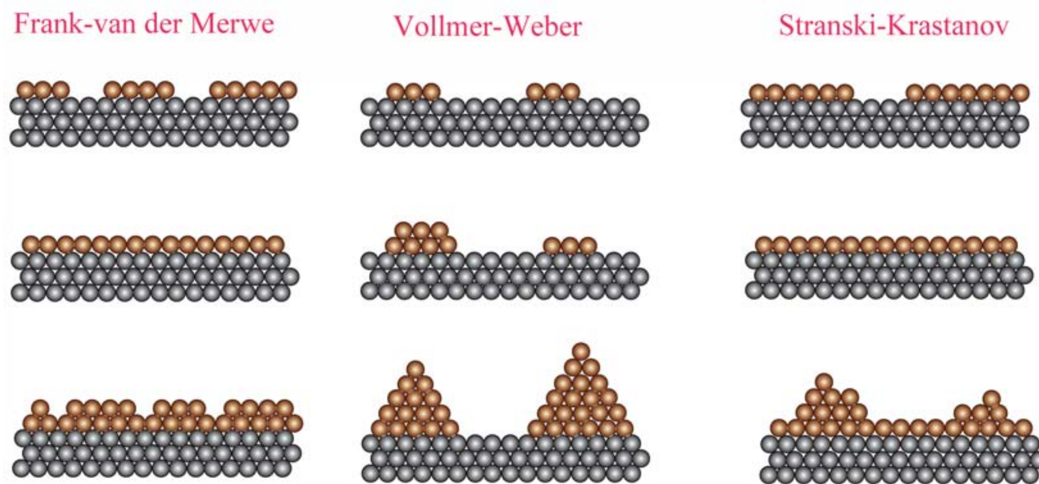

Fig 1.2: Schematic illustration of the three different growth modes: (a) layer-by-layer or Frank-van der Merwe growth, (b) island or Vollmer-Weber growth, (c) layer-plus-island or Stranski-Krastanov growth.

In the early stage of film growth, there are many of physical processes related to the growth the atoms/molecules on substrate surface. These process are (a) atom or molecule deposition, (b) deposited molecule diffuse on flat surfaces of the substrate, (c) dimer formation with deposited species, (d) attached or (e) detached of the species to an existing island, (f) diffusion from the island, (g) downward hopping from top of the island, (h) nucleation on top of the island and finally (i) desorption. All these process are illustrated in Fig. 1.3. Out of the all mentioned processes, interplay of some processes generates different type of growth. The relative rates of occurrence of these processes primarily are controlled by the deposition rate and substrate temperature (T_{sub}). Substrate temperature activates kinetic process by enabling the migration rate of diffusion. Even in the case of diffusion controlled growth, the step edge and its potential energy distribution play an important role. The step edge barrier (Ehrlich-Schwobel barrier)[16, 17] plays an very important role to determine the molecular diffusion between intermolecular steps. As a result, mounds, wire, ribbons formation is observed.

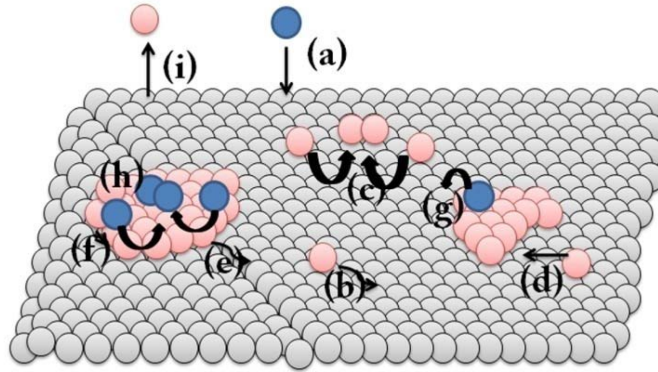

Fig. 1.3 Schematic diagram of the different process occurring during film growth

Growth of some (i.e. Ag, Pb etc.) metal films on semiconductors surfaces, however, does not follow the standard growth mode described above. The growth modes for these systems have been described as an *electronic growth* where preferential layers (N-atomic layers) dependent thickness is observed.[18, 19] Some theoretical attempts have been made to understand the N-dependent stability of metal films in terms of the energies of the quantum well (QW) states.[20, 21] The QW states are usually analyzed using a picture of standing waves within a potential well, in which energy-dependent phase shift upon reflection at the interface is included. For s-p metals the QW energy levels are often described by the quantization condition (the phase accumulation model in Fig.1.4)

$$2k_z(E_n)Nd_0 + \varphi_1\,(E_n) + \varphi_2(E_n) = 2n\pi$$

where k_z is the component of the wave vector perpendicular to the film surface, $k_z(E_n)$ is determined by the band dispersion along the normal to the film surface, d_0 is the interlayer spacing, N is the number of atomic layers in the film and n is the quantum number (an integer). $\varphi_1(E_n)$ and $\varphi_2(E_n)$ are the energy-dependent phase shifts of the electronic wave function upon refection

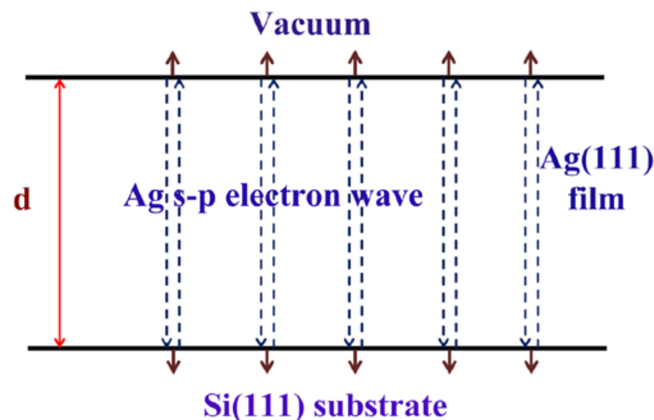

Fig. 1.4: Schematic diagram illustrating the analogy of the multiple-electron phase accumulation model with an electron interferometer for the Ag/Si(111)-(7×7) system. Multiple reflections of Ag s-p electrons at the interfaces are indicated by dashed arrows. Evanescent states outside the Ag films, due to interface reflectivities lower than 100%, are indicated by short arrows

at the two boundaries of the film.[22, 23] This model considers the QWSs of electrons trapped inside the Ag film between the barriers at the Ag/Si(111) and Ag/vacuum interfaces. Upon reflection of Ag s-p electrons at the interfaces, phase changes $\varphi_1(E_n)$ and $\varphi_2(E_n)$ are introduced, while $2k_z(E_n)Nd_0$ is the phase change accumulated upon traversing the Ag film. Total phase changes decide the standing wave formation and stabilize the thickness of the film. In this thesis, we have explored this growth mode in Ag on Si(111)-(7×7) surfaces.

1.2.2 Organic Thin Film Growth

The growth modes discussed in the previous section are essentially applied for inorganic materials, in general. However, there are intrinsic properties of organic materials which make these growth scenarios more complex.[24-26] Organic molecules are extended and anisotropic objects giving rise to internal degrees of freedom. As a result, the molecular arrangement within the films can make more complex arrangements and form different types of surfaces morphologies. Moreover, the interaction potential between

TH-1132_08612114

molecules and molecule-substrate is anisotropic. The interaction between organic molecules is dictated by van-der Waals interactions with contributions of other non-covalent interactions (H-bonding, $\pi-\pi$ and dipolar interactions) in presence of certain functional groups. As a results, often the growth can form different types of structures such as 3D mounds, wires, ribbons or unidirectional terraces.[27]

A mound is a 3D island which is multilayer stack of 2D layer. Due to the instability of the organic molecular stacking this type of structure formations is observed. The formation of mounds on a surface can be attributed to many different growth processes which can be local or non-local in nature. The formation of mounds as a result of limited diffusion due to step edge barrier(E_s) is very common for organic thin film growth.[28, 29] Fig. 1.5 shows the schematic of a typical ES barrier. This does not allow atoms/molecules to diffuse over the edge of the step on the surface, which creates an overall uphill current of the diffusive particle flux. This effect is characterized as local growth effect because it involves particles on the surface.

To investigate the film growth, the kinetic processes should be considered on the molecular scale, among of which interlayer mass transport determines the film morphology.[27, 30, 31] During the step down process, molecule has encountered ES barrier appended to the surface diffusion activation energy. In the case of efficient step down interlayer transport, nucleation of second layer take place after the full coalescence of layer underneath, resulting in layer-by-layer growth. In contrast, inefficient interlayer mass transport results in a 3D mound formation and increases the roughness of the film.

TH-1132_08612114

In order to form flat top organic mounds, step down as well as step up interlayer mass transport process are to be considered.[32] Fig. 1.5 shows the energetic diagram of molecular diffusion on the surface.

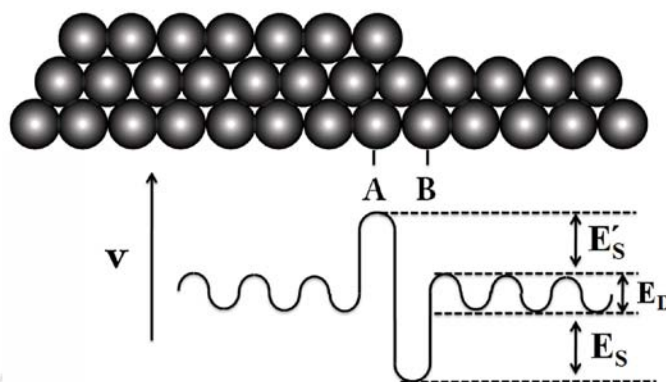

Fig. 1.5. Side view of a surface with monatomic height step and hypothetical potential map of an adatom on the surface. E_D is the surface diffusion activation energy, E_S is the ES barrier energy and E_S is the additional energy due to step.

For a molecule descending from one terrace to next terrace (step down process) encountered an energy barrier E_D+E_S', where E_D is surface diffusion activation energy and E_S' is ES barrier. On the other hand for a molecule ascending from one terrace to next terrace (step up process), the molecule encounters an energy barrier of $E_D+E_S+E_S'$, where ES is additional step edge binding energy. Fig. 1.6 shows the different kind of surface morphology formation.[32] With efficient descending process, layer-by-layer growth was observed as shown in Fig. 1.6(a). In case of inefficient descending process there is pyramid like mound formation shown in Fig. 1.6(b). Fig. 1.6(c) shows the shape of the mounds due to interlayer mass transport. However when an ascending process is enabled then flat top mound formation is observed as shown in Fig 1.6(d).[32] Therefore by controlling the diffusion and ES barrier, which are essentially the material properties, the mound type island formation is possible.[16, 33-35] The height dependent step edge (ES) barrier is very common for the growth of organic semiconductor thin film growth.

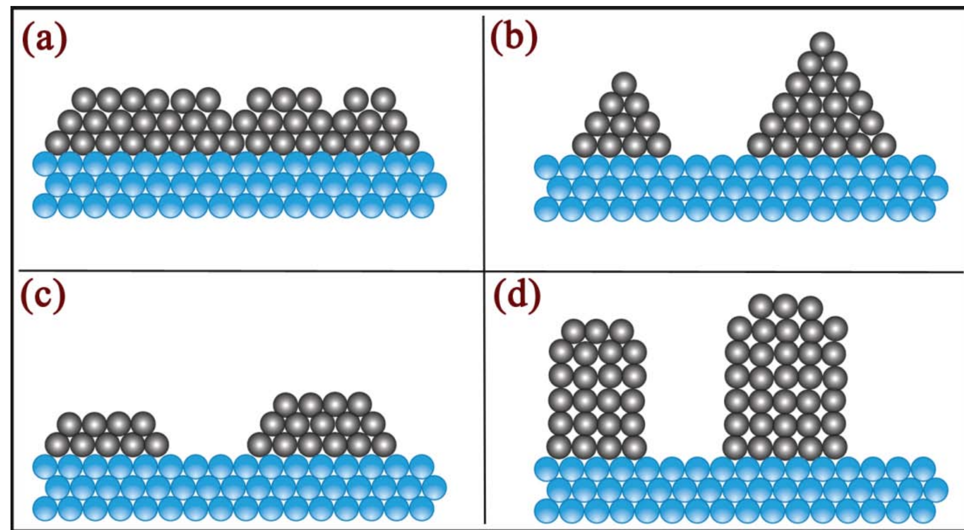

Fig. 1.6 : Different types of layer formation due to ES barrier variation.

On the other hand local surface slope (m) is an important parameter to define the surface morphology. When a molecule is deposited, then it diffuses towards the edge of a descending or ascending step. Here in the Fig 1.7 we have shown the different step edge diffusion due to different local slope. As the step barrier reflects the molecule upward, an upward current is initiated and form a mound type surface structures. This uphill current which is proportional to the height difference i.e. $j \sim \nabla h$, where j is diffusion current and ∇h is height gradient. While the molecules are diffusing upward the local surface slope of the surface structure are changing. Here diffusion length (l_D) is another important parameter that control the effective diffusion of the molecules. Thereby, it controls the surface morphology. Here l_D is defined as the average length that a molecule can diffuse. When local slope is small then the average terrace width (l) is large. In this case, molecules with diffusion length ($l_D<l$) will have less probability to diffuse up. However, if the local slope is more in that case $l_D>l$ then the step up process increases. Here l_D directly depends upon the substrate temperature (T_{Sub}). Therefore

T_{Sub} also plays an important role to define surface morphology. Combining these two process together decides the formation of mounds.[33]

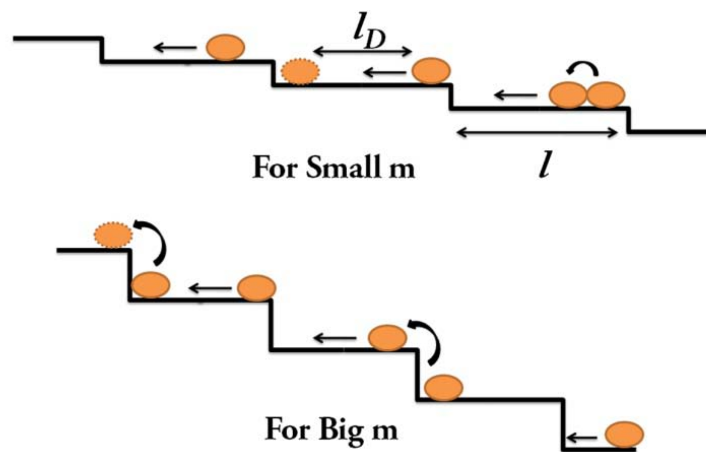

Fig. 1.7 : Schematic diagram of uphill current due to (a) small slope and (b) large slope respectively

On the other hand, formation of ribbon is another important example of diffusion control structure formation. Ribbons are one dimensional structure with diameter ranging from few nm to 200nm and length up to several microns. With respect to other structures, they present several advantages comparable to bulk counterpart,[12, 34-37] like large surface to volume ratio, a direct carrier conduction path, a large variety of potential novel properties available through control of size and structure and high compatibility with standard industrial device fabrication technology. Generally self-assembly is driven by intermolecular non-covalent interaction such as hydrogen bonding, ion-ion interaction, $\pi-\pi$ interaction with van-der Waals forces. Depending upon these interactions different types of 1D structure are formed.[6] Neverthless, favourable diffusion along a particular direction can also form 1D structures.

1.3 Organic Molecules

Here in this thesis we have chosen some of the n type organic semiconductor which has high thermal stability that makes it possible to evaporate them thermally under vacuum in a chamber. This in turn, guarantees a good control over their chemical and physical properties. We have chosen two derivatives of Perylene and one derivative from Naphthalene. The selection of the materials is because of their interesting electrical and optical properties. The Perylene core is itself a donor which is used in the preparation of organic devices for a long time.[38, 39]

1.3.1 TC-PTCDI-C_8

N,N'-bis(octayl)perylene-1,6,7,12-tetrachloro-3,4,9,10-bi (dicarboxi mide) (TC-PTCDI-C_8) belongs to the perylene group compound. The chemical structure of the molecule is shown in Fig. 1.8 which is about 30.1Å long including the chain attached with perylene core and 8.9Å in width.

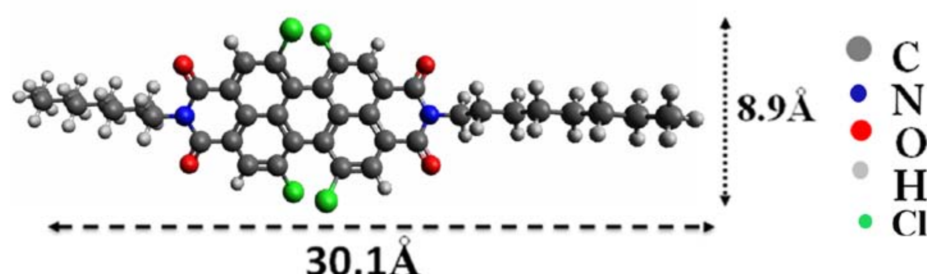

Fig. 1.8: Schematic diagram and dimension of TC-PTCDI-C_8 molecules

It forms flat top mound type surface morphology on SiO_2 substrate at elevated temperature. The derivative is showing good thermal and electrical stability.

1.3.2 PTCDI-Ph

N, N´-di-phenyl perylene tetracarboxylic diimide (PTCDI-Ph) is another perylene derivative. The chemical structure and the dimension of the molecule is shown in Fig 1.9. The length of the molecule is 19.91Å.

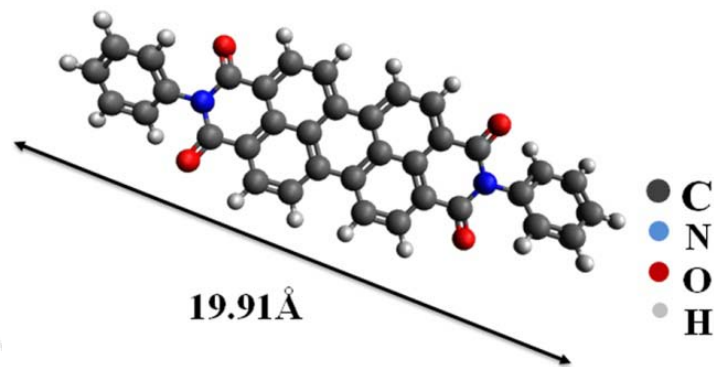

Fig. 1.9: Schematic diagram of the PTCDI-Ph molecule. The length of the molecule is mentioned.

It is a very good compound for the application of opto-electronic devices. After depositing a long flat top terrace with good crystallinity is formed.

1.3.3 ^{4DMAPE}NI

4 - (4-n, n-dimethylaminophenylethynyl) - n - (2-propynyl) - 1, 8 napthalimide ($^{4\text{-}DMAPE}$NI) is the n type organic semiconductor in the Napthalene family. The structure of the molecule and the dimensions are shown in Fig. 1.10. The length of the molecule is 16.48Å.

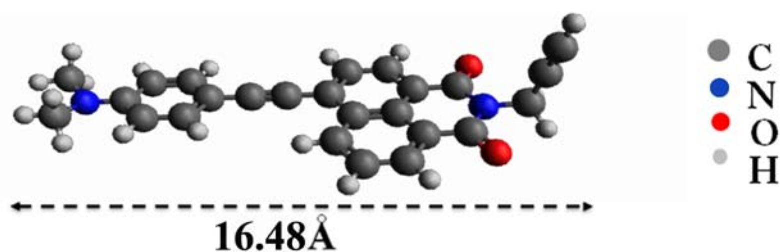

Fig. 1.10: Schematic diagram of the $^{4\text{-}DMAPE}$NI molecule. The length of the molecule is mentioned.

These molecules can be stacked with each other not only just via π–π interaction but also CH-Π interaction. As a result long ribbon type structure may form.

TH-1132_08612114

1.4 References

1. B. Mukherjee and M. Mukherjee, Org. Electron. **12**, 1980 (2011).
2. P. Y. Bruice and K. J. Rajendraprasad, *Essential Organic Chemistry* (Pearson Education, Upper Saddle River, New Jersey, 2008).
3. J. A. A. W. Elemans, R. v. Hameren, R. J. M. Nolte, and A. E. Rowan, Adv. Mater. **18**, 1251 (2006).
4. W. Brütting, *Physics of Organic Semiconductors* (Wiley-VCH, Weinheim, 2005).
5. H. Z. Chen, M. M. Ling, X. Mo, M. M. Shi, M. Wang, and Z. Bao, Chem. Mater. **19** (2007).
6. J. L. Atwood and J. W. Steed, *Organic Nanostructures* (Wiley-VCH, Weinheim, 2008).
7. J. Fraxedas, *Molecular Organic Materials: From Molecules to Crystalline Solids* (Cambridge University Press, Cambridge, 2006).
8. F. So, *ORGANIC ELECTRONICS: Materials, Processing, Devices and Applications* (CRC Press, New York, 2010).
9. V. Coropceanu, J. r. m. Cornil, D. A. d. S. Filho, Y. Olivier, R. Silbey, and J.-L. Bre´das, Chem. Rev. **107**, 926 (2007).
10. H. Klauk, *Organic Electronics: Materials, Manufacturing and Applications* (Wiley-VCH, Weinheim, 2006).
11. N. Martín and F. Giacalone, *Fullerene Polymers: Synthesis, Properties and Applications* (Wiley-VCH, Weinheim, 2009).
12. A. N. Aleshin, Adv. Mater. **18**, 17 (2006).
13. F. C. Frank and J. H. v. d. Merwe, Proc. Roy. Soc. London **A149**, 205 (1949).
14. M. Volmer and A. Weber, Phys. Chem **119**, 277 (1926).
15. I. N. Stranski and V. L. Krastanov, Akad. Wiss. Lit. Mainz Math-Natur. Ki. IIb **146**, 797 (1939).

TH-1132_08612114

16. Z. Zhang and M. G. L. , Science **276**, 377 (1997).
17. R. Ganapathy, M. R. Buckley, S. J. Gerbode, and I. Cohen, Science **327**, 445 (2010).
18. Z. Z. Q. Niu and C.-K. Shih, Phys Rev Lett **80**, 5381 (1998).
19. D. K. Goswami, K. Bhattacharjee, B. Satpati, S. Roy, P. V. Satyam, and B. N. Dev, Surf. Sci. **601** 603 (2007).
20. L. Gavioli, K. R. Kimberlin, M. C. Tringides, J. F. Wendelken, and Z. Zhang, Phys Rev Lett **82**, 129 (1999).
21. S. J. Tang, C. Y. Lee, C. C. Huang, T. R. Chang, C. M. Cheng, K. D. Tsuei, H. T. Jeng, V. Yeh, and T. C. Chiang, Phys Rev Lett **107**, 066802 (2011).
22. C. M. Wei and M. Y. Chou, Phys. Rev. B **66**, 2334081 (2002).
23. N. V. Smith, N. B. Brookes, Y. Chang, and P. D. Johnson, Phys. Rev. B **49**, 332 (1994).
24. F. Schreiber, phys. stat. sol. **201**, 1037 (2004).
25. G. Witte and C. Wöll, J. Mater. Res. **19**, 1889 (2004).
26. N. Savage, Nature **479**, 5 5 7 (2011).
27. T. Michely and J. Krug, *Islands, Mounds, and Atoms: Patterns and Processes in Crystal Growth Far from Equilibrium* (Springer-Verlag, Berlin, 2003).
28. G. Ehrlich and F. G. Hudda, J. Chem. Phys. **44**, 1039 (1966).
29. R. L. Schwoebel and E. J. Shipsey, J. Appl. Phys. **37**, 3862 (1966).
30. Z. Zhang and M. G. Lagally, Science **276**, 377 (1997).
31. J. A. Venables, G. D. T. Spiller, and M. Hanbücken, Rep. Prog.Phys. **47**, 399 (1984).
32. D. Y. Zhong, M. Hirtz, W. C. Wang, R. F. Dou, L. F. Chi, and H. Fuchs, Phys. Rev. B **77**, 113404 (2008).

TH-1132_08612114

33. A.-L. Barabási and H. E. Stanley, *Fractal Concepts in Surface Growth* (Cambridge University Press, Cambridge, 1995).
34. , edited by H. S. Nalwa (Academic Press, New York, 2000).
35. G. A. Ozin, Adv. Mater. **4**, 612 (1992).
36. A. P. Alivisatos, P. F. Barbara, A. W. Castleman, J. Chang, D. A. Dixon, M. L. Klein, G. L. McLendon, and M. E. Thompson, Adv. Mater. **10**, 1297 (1998).
37. B. H. Kim, D. H. Park, J. Joo, S. G. Yu, and S. H. Lee, Synth. Met **150**, 279 (2005).
38. H. Sirringhaus, R. H. Friend, X. C. Li, S. C. Moratti, A. B. Holmes, and N. Feeder, Appl. Phys. Lett. **71**, 3871 (1997).
39. D. Shukla, S. F. Nelson, D. C. Freeman, M. Rajeswaran, W. G. Ahearn, D. M. Meyer, and J. T. Carey, Chem. Mater. **20**, 7487 (2008).

TH-1132_08612114

Chapter II

Experimental techniques and data analysis

In this present chapter we focus on the experimental methods for preparation of organic and inorganic films as well as the techniques employed to characterized and measure film properties.

The aim is to grow organic and inorganic self assembled structures and to study the growth mechanism, structural, electrical and optical properties. The growth techniques for different materials are different. This not only depends on the sublimation temperature of the materials but also depends on the material properties. We have used high vacuum (~10^{-7} mbar) chamber for the growth of organic molecules. However, ultra high vacuum (~10^{-10} mbar) chamber was used to grow Ag films. To minimize impurities that severely affects the growth of Ag.

Most extensively used technique to study the surface morphology was scanning probe microscopy (SPM) and to access structural information we used X-ray scattering. To study the optical properties, UV-Vis spectroscopy, Photoluminescence (PL) and Time resolved spectroscopy (TRPL) were used. In this chapter, the techniques will be briefly discussed.

TH-1132_08612114

2.1 Growth Techniques of self-assembled Organic Structures

In this section, the different techniques for the deposition of Organic Semiconductor and Ag are discussed.

2.1.1 Substrate Preparation

Before we start the growth of self-assembled structures, it is important to make sure that the substrate surfaces onto which the films are to be grown, is clean. We have used two different kinds of substrates. For the growth of organic structures, we have used Si(100) with native layer of SiO_2 substrates. For the growth of Ag, we used atomically cleaned Si(111)-(7×7) surface. SiO_2 surfaces were first cleaned ultrasonically by Di-water for 20 min. After that acetone and methanol were used to clean ultrasonically separately for 10 min. Finally these were cleaned by Di-water followed by drying with dry-nitrogen gas. The cleaned SiO_2 substrates are then degassed inside the vacuum chamber at 600^oC overnight and cooled down to deposition temperature. Si(111) with SiO_2 surfaces are also cleaned with similar procedure. After degassing the substrate overnight, it was flashed to 1250oC for few seconds to remove oxide layers and prepare a atomically clean reconstructed surfaces. These surfaces were used to grow Ag film in the UHV chamber.

2.1.2 Thin Film Growth Techniques

Thermal evaporation system has been used to grow organic molecules. This system works under high vacuum (HV) condition with base pressure 3×10^{-7} mbar. A custom-made growth chamber has been designed which is shown in Fig.2.1.

TH-1132_08612114

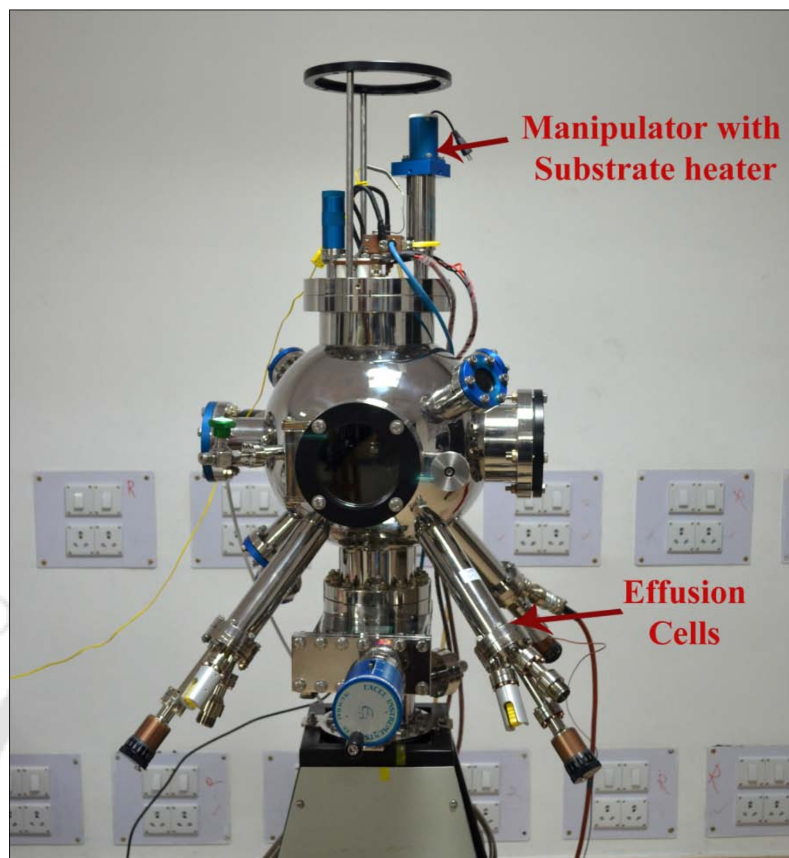

Fig. 2.1: Thermal evaporation system along with substrate heating arrangement

This chamber contains three Knudsen Cells to grow organic molecules. The Knudsen cells were designed, fabricated and installed. A sample manipulator is mounted from the top of the chamber with option of 360° azimuthally motorized rotation of the substrate. The substrate can be heated up to 800°C. The chamber also contains a quartz microbalance (QM) to monitor the thickness of the films during growth. Five Knudsen cells can be accommodated in the growth chamber.

For many applications, the incorporation of foreign atoms or molecules into a growing film is undesirable. To avoid the incorporation of residual gases into the growing film ultra-high vacuum pressures (UHV, better than 10^{-10} mbar) may be necessary. The molecular beam epitaxy (MBE)[1-5] has proven to supply epitaxially grown films of high purity. MBE is based on the thermal evaporation of the source material typically in UHV

conditions.[1, 2, 5, 6] The compound is thereby evaporated from a special oven in a more or less directed beam which guarantees a uniform thickness of the deposit. By controlling the sublimation temperature very low deposition rates can be obtained. The high purity along with the low deposition rates allow for the growth of films with good crystallinity. The uses of the MBE technique together with in-situ film diagnostic methods during and immediately after growth have provided many new insights into growth processes.

A custom-made compact MBE system along with the capability to transfer the MBE-grown samples to a UHV transfer chamber as well as to a commercial UHV STM, designed by us in collaboration with and assembled by Omicron Vacuum physik GmbH, has been installed. A UHV variable temperature scanning tunneling microscope (VTSTM from Omicron) has been coupled with the MBE system at a later date. This system is shown in Fig. 2.2.

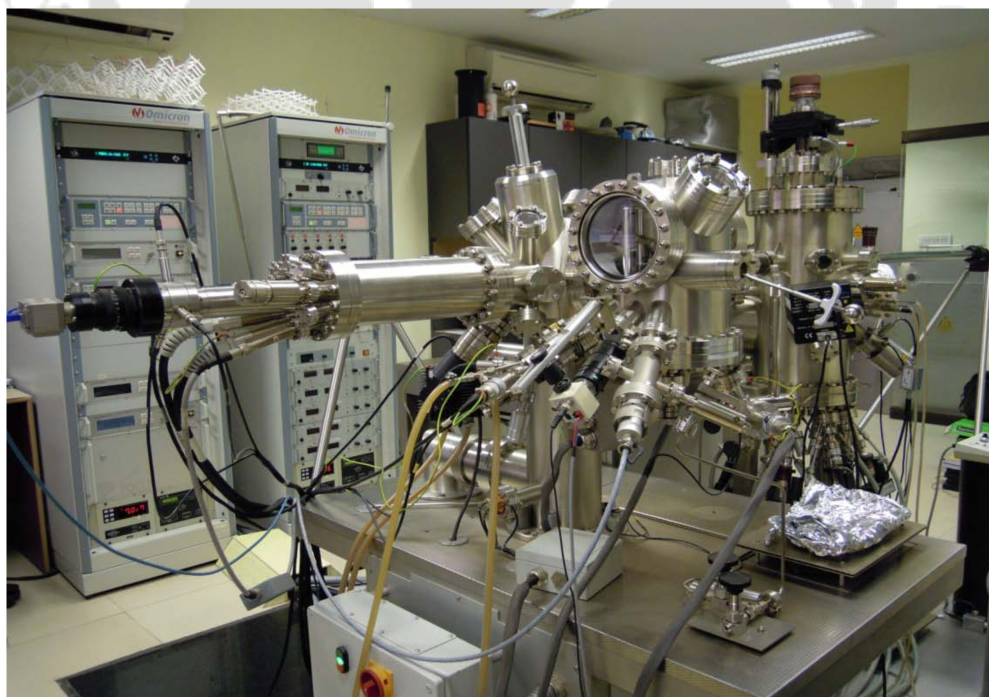

Fig. 2.2: An Omicron MBE system along with VTSTM and RHEED.

TH-1132_08612114

The MBE system has five Knudsen cells, a low power electron beam evaporator, a quartz crystal microbalance (QCM) and a residual gas analyzer (RGA). There is also a reflection high energy electron diffraction (RHEED) equipment fitted to the MBE unit for monitoring surface reconstruction and growth. For sample cleaning it has direct heating as well as Ar^+ ion sputtering facilities. The sample manipulator has a Z-translation (vertical) and the azimuthal angle can be varied over 360°. It also has a resistive heating facility so that the substrate temperature can be raised up to 900^oC. The substrate temperature and the rate of deposition control epitaxial growth of different materials. Out of the five Knudsen cells, three are capable to heat up to 1500^oC and other two are capable to heat up to 1000^oC. The temperature range achievable in the VTSTM is 50 K-500 K. The best base pressure achieved in the MBE chamber is 3×10^{-11}mbar and that in the VTSTM chamber 2×10^{-11}mbar mbar. This combined MBE-VTSTM system and its initial performance have been described in ref.[7]

In this thesis, MBE was used to grow Ag mounds on Si(111)-(7×7) surfaces. As the metals are very reactive and easily get contaminated, UHV condition is required during the growth. Nevertheless, to prepare atomically cleaned reconstructed substrate surfaces it is necessary to have UHV condition. However, organic molecules were grown on SiO_2 surfaces, which is essentially amorphous. Therefore, UHV condition is not necessarily required to grow organic molecules. Though, it is possible to incorporate organic crucible into UHV chamber. We have used separate HV chamber to grow organic molecules except two kinds of molecules.

2.1.3 Evaporation of organic molecules

The organic deposition technique we used is based on the evaporation of the source material under HV conditions. To achieve an efficient deposition of the evaporant with a uniform thickness of the deposit, special evaporation cells have been developed which deliver a somewhat directed beam.

In a so-called Knudsen cell, as is shown in Fig. 2.3(a), the organic molecules are sublimated from a ceramic crucible with a small opening. The temperature of the evaporant can be controlled to obtain the desired vapor pressure.[8, 9] We designed a simple Knudsen cell. The support materials

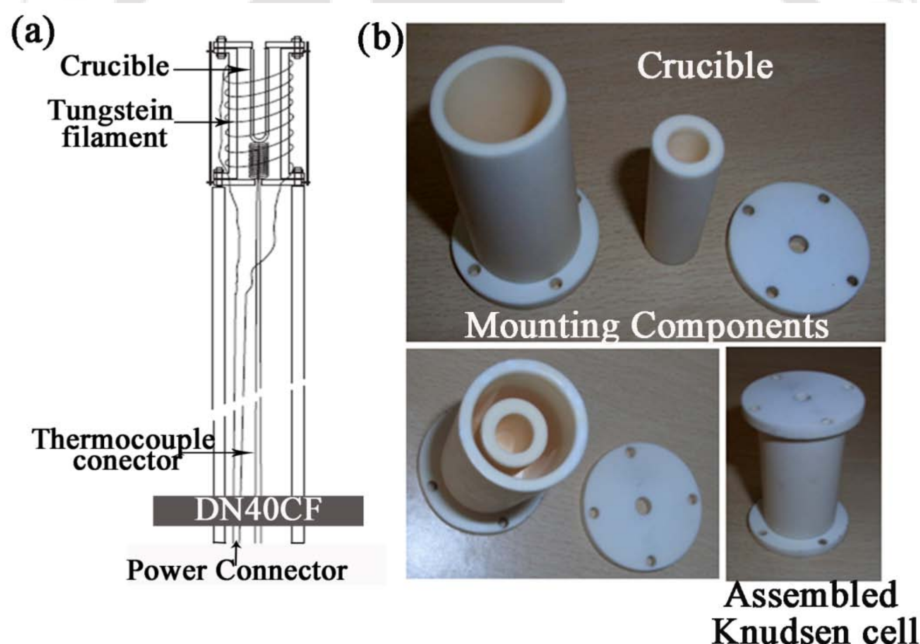

Fig. 2.3 (a) Schematic diagram of Knudsen cell along with DN40CF flange, thermocouple and electrical connection, (b) Various components of the in-house developed Knudsen cell and its total structure. Molecules come out from the small hole in the upper portion.

(ceramic, tungsten, molybdenum etc) of the evaporation cell were chosen in such a way as they had negligible vapor and dissociation pressures at the

operating temperatures (up to~500°C) to avoid contamination of the deposit. The width of the organic molecular beam emitted from this cell was sufficiently broad to guarantee a homogeneous film thickness on a substrate with a lateral length scale of 2 cm. The substrate was positioned in such a way that the surface was normal to the direction of the molecular beam. Resistance-heated tungsten wires wound around a ceramic cylinder served as a heater and the evaporation temperature (as measured by thermocouples mounted close to the crucible) was controlled by temperature controller (Eurotherm 2408) with an absolute precision of ± 5°C. Typical elements made with Al_2O_3 materials for Knudsen cell are shown in Fig. 2.3(b). These parts are mounted onto a DN 40CF flange, which is mounted with the vacuum chamber. Fig. 2.4 shows the performance of these cells. The cells take about 45 minutes to reach at the set temperature 250°C and 430°C as shown in Fig. 2.4(a) and (b) for T_{cell} = 250°C and 430°C respectively.

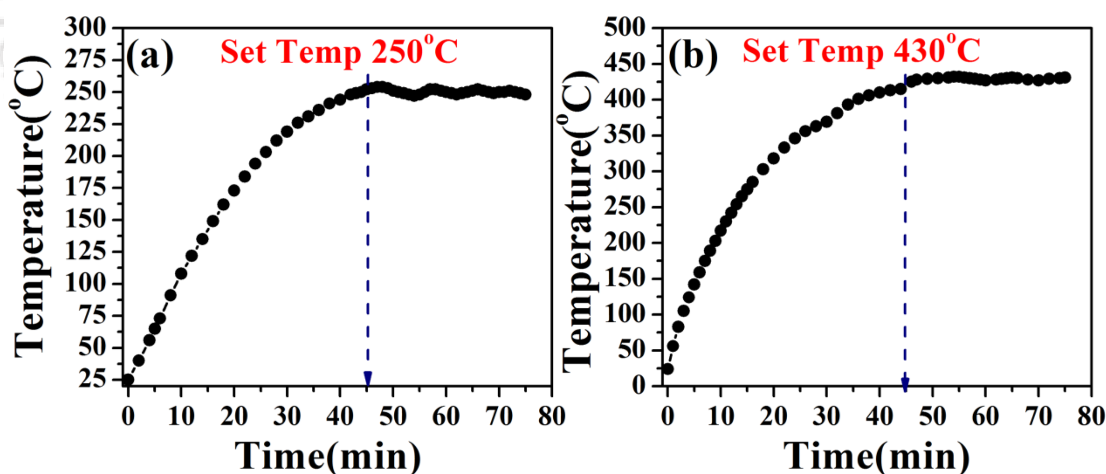

Fig. 2.4: Ramping rate (a) for 250°C and (b) 430°C of the Knudsen shell. At the desired temperature the heating rate is almost constant.

2.2 Characterization Techniques

Deposited films were characterized using several scientific tools. In this section we describe the instruments for structural, optical and electrical characterizations that are used in this thesis work. Some in-house developed instruments are also discussed.

2.2.1 Structural Characterizations

A. Scanning Tunneling Microscopy (STM)

In the early 1980's scanning tunneling microscopy (STM) was developed with the first real-space images of the surfaces of silicon. Now a day STM is used in a wide variety of disciplines, including fundamental surface science, routine surface roughness analysis and 3D surface imaging. For this invention Gerhard Binning and Heinrich Rohrer were awarded the Nobel prize in physics in 1986.

The components for the STM operation are:

Atomically sharp tip: The tips are mainly made from metal (e.g. W, Pt-Ir, Au) wires. The preparation procedures are first ex situ mechanical grinding or cleavage or electrochemical etching then insitu annealing, field emission/evaporation and even soft crash of the tip by touching a sample.

Scanner: It is a piezoelectric scanner which is used as electromechanical transducer. It can convert electric signal of 1mV to 1kV into mechanical motion in the range from an Å to few μm.

Feedback electronics: This circuit is connected with the instruments to control the sample to tip gap.

Computer: This is required to control the tip position and acquire data.

TH-1132_08612114

A coarse positioning system is required with scanner which brings the tip within the tunneling distance of the sample and to retract it back to sufficient distance (a few mm).

The basic operation[10, 11] is that when STM tip is placed in a closest distance (5-10Å) then the wave functions of the closest tip atom and surface atom overlap. If we apply V voltage within the tip and sample then current is tunneling from the sharp tip to the sample. The tunneling current is defined as

$$j = \frac{D(V)V}{d} e^{(-A\varphi_B^{1/2} d)}$$

Where d is the effective tunneling gap, D(V) is the electron density of states. A is a constant and φ_B is the effective barrier height of the junction.[5] Schematic diagram of the basic operation and the tunneling is shown in the Fig. 2.5 (a, b).

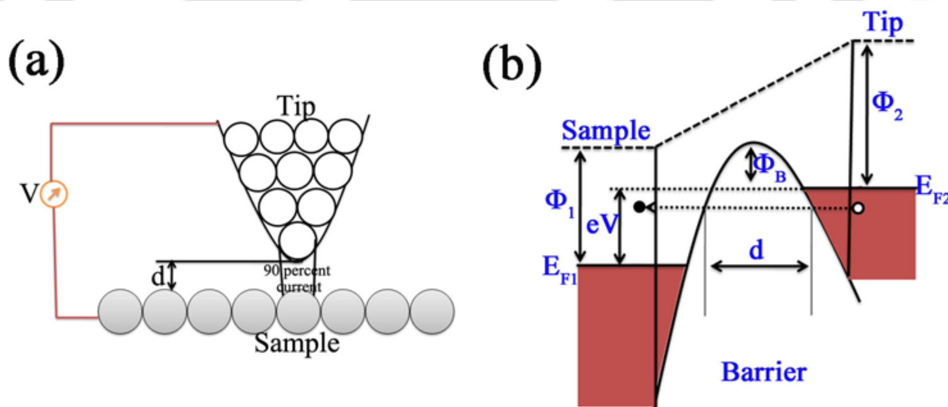

Fig. 2.5:(a) Schematic diagram of the STM operation (b) Energy diagram of the tunneling contact of the STM tip and the metallic sample. E_{F1} and E_{F2} are the Fermi levels of the surface and the tip, φ_1 and φ_2 are the work functions of the surface and the tip, φ_B is the effective barrier height, d is the effective tunneling gap and V is the bias voltage. The diagram illustrates the situation when STM probes the empty states of the surface.[5]

Depending upon the sign of bias voltage and the tip to sample spacing the resultant tunneling current varies and effectively changes the STM image. If the separation between the tip and the sample changes by 10% (on the order of 1Å) , the tunneling current changes by a order of magnitude or if the current is kept const to within 2%, the gap width remains constant to within 0.01Å. As per the lateral resolution, 90% of the tunneling current flows through the gap between the last atom of the tip and the atom of the surface. So the STM can image the surface of the sample with the sub angstrom precision vertically and atomic resolution laterally. Depending upon the bias of the tip electron or hole can tunnel from the tip to sample. At negative tip bias the empty state STM image is obtained.STM is designed to scan the sample in two modes: (i) constant height or (ii) constant current mode as shown in the Fig. 2.6.

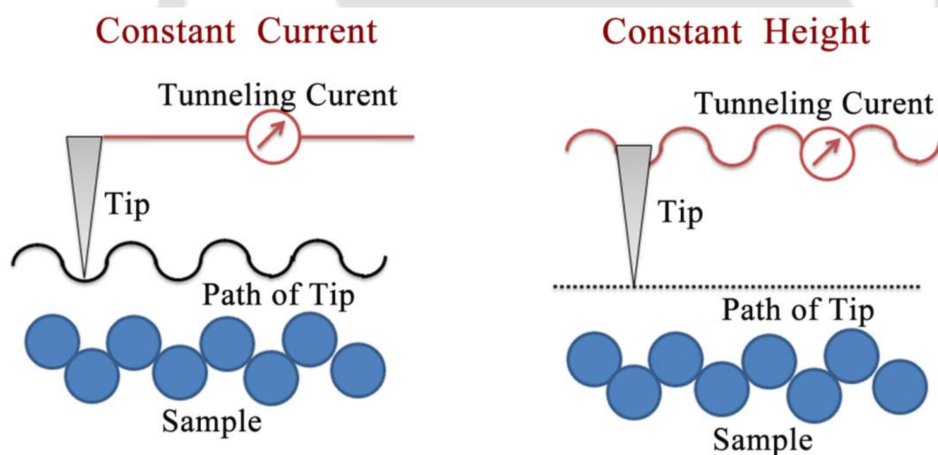

Fig. 2.6: Schematic diagram of Constant current mode and constant height mode of STM operation[12]

In *constant height mode* the tip travels in a horizontal plane above the sample and the tunneling current varies depending upon the topography and the local surface electronic properties of the sample.

In *constant current mode* STM a feedback is used to keep the tunneling current constant by adjusting the height of the scanner at each measurement point. When the system detects an increase in tunneling

TH-1132_08612114

current it adjusts the voltage applied to the piezoelectric scanner to increase the distance between the tip and the sample.

B. Atomic Force Microscopy (AFM)

The STM generally operates for conducting surface but there is no such type of restriction for AFM operation.[10, 11, 13, 14] The AFM probes the surface of a sample with a sharp tip, a couple of microns long and often less than 100Å in diameter. The tip is at the end point of the cantilever that is ~100-200 μm long. The force between the tip and the sample surface causes the cantilever bend, or deflect. A detector measure the deflection as the tip scanned over the surface. The measured deflection allows a computer to generate a map of the surface topography. The force is acting in this region is generally van der Waals type force of the magnitude ~ 10^{-9} N. Depending upon the operation and the tip to sample distance there are two types of operation: (i) *Contact* and (ii) *Non-Contact* mode.

In *contact mode* the tip is so close to the sample surface that it feels the repulsive force due to the overlap between the electron clouds of atoms of the tip and the surface. In this operation the distance between the tip and the surface is less than a few angstroms. The force distance curve is shown in the Fig. 2.7. At the right side of the curve the atoms are separated by a large distance. As the atoms are brought together they at first weakly attract each other. This attraction is increased until the atoms are so close together that their electron cloud begins to repel. This repulsion slowly decreases the attraction and inter-atomic separation continues to decrease. The force tends to zero when the distance is couple of angstroms. When the total van der Waals force becomes positive the atoms are in contact. The slope of the van der Waals curve is very steep in repulsive or contact region. This force

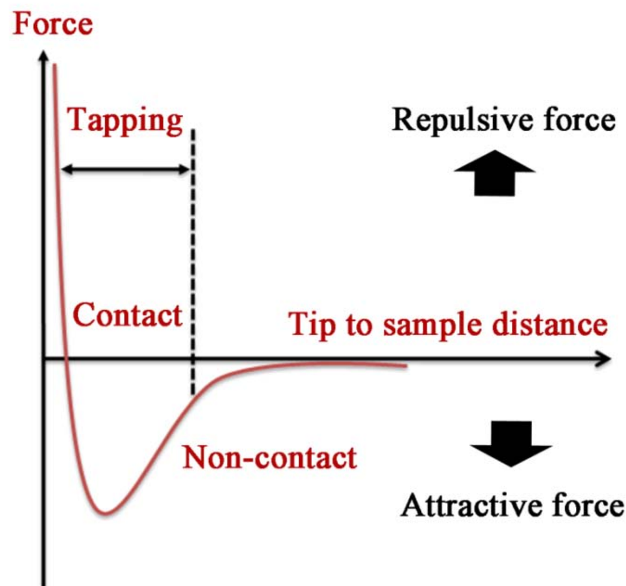

Fig. 2.7: The qualitative dependence of the van der Waals force on inter-atomic distance.[5]

can balance any force that attempts to push the atom closer together. In this operation, the height of the piezoelectric scanner is constant. When the tip is moving throughout the sample, the deflection of the cantilever is monitored using a laser focused at the top of the cantilever. The reflected light is detected by a highly sensitive quadrant photodiode. The obtained laser signal is redirected into a well constructed feedback loop to adjust the vertical scanner displacement, which keeps the cantilever deflection constant. So the surface topography can be recorded by monitoring the motion of the piezoelectric scanner. The basic operation[15] is shown in the Fig. 2.8. Depending upon the operation there are two types of modes: *constant height* and *constant force* modes.

In *constant height* mode the special variation of the cantilever is used directly to generate the topographic image because height of the scanner is fixed.

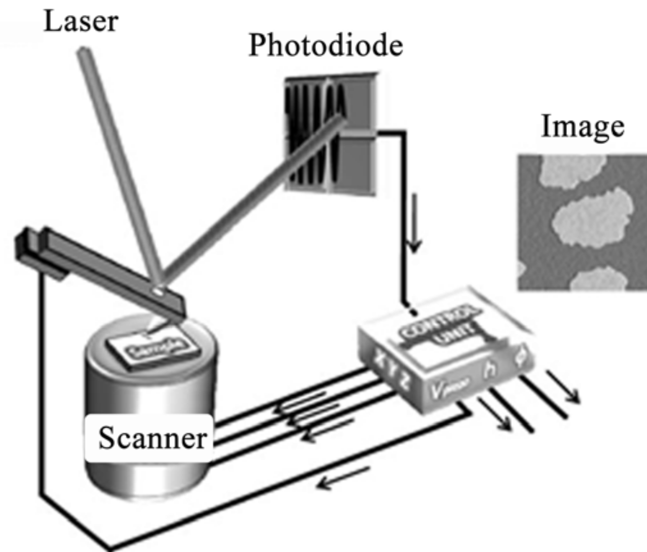

Fig. 2.8: Schematic diagram of the AFM operation.[15]

In *constant force* mode the deflection of the cantilever is used as an input to a feedback circuit that moves the scanner up and down in the vertical direction, responding to the topography by keeping the deflection constant. In this case image is generated from the scanner motion. Here total force applied to the sample is constant.

In *non contact mode* the detected signal originates from the amplitude variation of the cantilever which is vibrating near the surface of the sample. In this operation mode the tip is generally 50-150 Å above the sample. This spacing is indicated on the van der Waals curve of the Fig. 2.8. In non contact mode the cantilever is vibrating near the resonant frequency (100-400 kHz) with the amplitude of few ten to hundred angstrom, the system monitors the resonant frequency or vibrational amplitude of the cantilever and keeps it constant with the aid of a feedback system that moves the scanner up and down. Keeping the resonant frequency or amplitude constant, the average tip to sample distance is kept constant. The operation is shown in the Fig. 2.9.

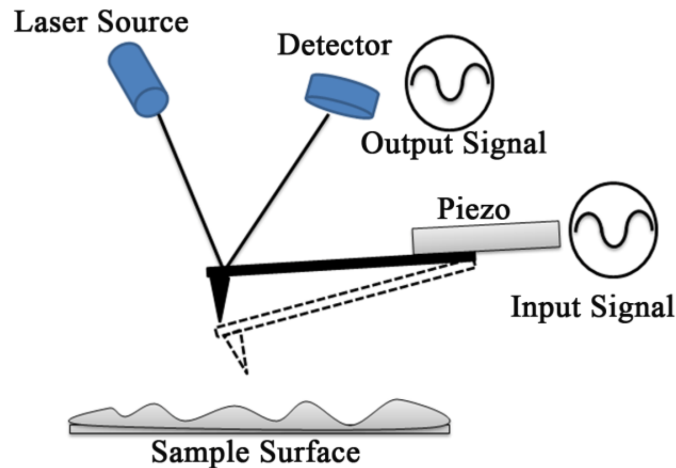

Fig. 2.9: Schematic diagram of the AFM operation in non contact mode.[14]

C. X-ray Scattering

(i) X-ray Diffraction

X- ray diffraction (XRD) is the most widely used non–destructive technique for general crystalline material characterization. The XRD patterns provide information on crystal phase, lattice parameter, strain and preferred growth direction. In XRD a collimated beam of x–rays, typically with wavelength λ=0.5–2.0Å, is incident on a specimen and is diffracted by the crystalline phases in the specimen according to 'Bragg's law',

$$2d\sin\theta = n\lambda$$

where d is the spacing between atomic planes in the crystalline phase, θ is the angle of incidence of the x–ray beam with the atomic plane, n represents the order of diffraction (we consider only the first order diffraction, n =1).[16] The intensity of the diffracted x–rays is measured as a function of the diffraction angle 2θ and the specimen's orientation. In the present study, the Seemann–Bohlin geometry is used,[17] where the incident x–rays impinge on a fixed specimen at a small angle 1–5° and the diffracted x–rays are recorded by a detector that moves along the focusing circle. This method provides good sensitivity for thin films, due to para-focusing and the large diffracting volume. Owing to the huge data bank available from JCPDS

Powder Diffraction Files covering practically every phase of every known material, crystal phase of the sample is identified from the peak positions of the diffractogram. Homogeneous or uniform elastic strain in the (*hkl*) direction can also be calculated from the shift in the diffraction peak positions, and the d_{hkl} spacing of the unstrained crystal. X–ray diffraction patters of the nanostructurs were obtained using a commercial XRD set-up (TTRAX III, RIGAKU 2500) using a Cu $K\alpha_1$ (λ=1.5406Å) radiation with nickel filter. All the data are taken at room temperature in thin film mode of the XRD at a grazing angle of 4°. Here in the Fig. 2.10 we show the commercial photocopy of the XRD instrument.

Fig. 2.10: 18kW X-Ray Diffractometer (TTRAX III, RIGAKU 2500), IIT Guwahati

(ii) X ray reflectivity

Almost a century after the discovery of X-ray scattering by materials it has been proved to be one of the most useful techniques to study crystal structure, surfaces and interfaces of thin film. In this thesis specular X-ray reflectivity (XRR) has been used to study the molecular arrangement with the film as well as structural information.[18-21] It is very useful in the case of (i) the determination of film thickness with precision of 0.1 nm, (ii) electron density profile throughout the film and (iii) determination of the roughness

TH-1132_08612114

of the surface and interface with precision of 0.1 nm. When a electromagnetic wave falls on the interface of two different media then some amount of radiation may be reflected, some amount may be refracted or some amount may be both reflected and refracted depending upon the incident angle and refractive coefficient of the media. X-ray reflectivity is limited to small angle of incidence where it is possible to consider electron density as continuous. The elastic scattering of X-rays with matter can be well described by an index of refraction which characterized the change of direction of the X-ray beam when traversing from the interface of the two materials with different electron densities.

For X-rays the refractive index n is given by

$$n = 1 - \delta + i\beta$$

Where
$$\delta = \frac{\lambda^2}{2\pi} r_0 \rho_e$$

$$\beta = \frac{\lambda}{4\pi} \mu_l$$

Here r_0 is the classical electron radius (2.818×10^{-15}Å), ρ_e is the electron density of the medium, μ_l is the linear absorption coefficient for the incident photons in the medium.[21, 22]

For total external reflection to occur, the incident angle, θ_{in} must be smaller than the so called critical angle θ_c, such that $\theta_{in} \leq \theta_c = \sqrt{2\delta}$. This is a very useful phenomenon since under this condition only an evanescent wave propagates below the surface and hence surface sensitivity is considerably enhanced.

The reflection and transmission of X-ray can then be treated as a classical problem of reflection of an electromagnetic wave at an interface. The Fresnel relationship for a flat surface yields,

TH-1132_08612114

$$R_F(q_z) = \left| \frac{q_z - \sqrt{q_z^2 - q_c^2 - \frac{32i\pi^2\beta}{\lambda^2}}}{q_z + \sqrt{q_z^2 - q_c^2 - \frac{32i\pi^2\beta}{\lambda^2}}} \right|^2,$$

with the wave vector transfer $q = (0,0,q_z = 4\pi Sin\theta/\lambda)$.

For a medium consisting of slabs of different electron densities and thickness which is shown in Fig. 2.11(a), the reflected intensity can be calculated by applying the boundary condition of the electric and magnetic fields at each interface. This leads to the dynamical theory which takes multiple reflections into account. The dynamical theory is described in detail in the monographs. A recursive formalism was presented the first time by Parratt[23, 24] and reflected intensity is given by[22]

$$X_j = \frac{|r_j|^2}{|t_j|^2} = e^{-2ik_{z,j}Z_j} \frac{r_{j,j+1} + X_{j+1}e^{2ik_{z,j+1}z_j}}{1 + r_{j,j+1}X_{j+1}e^{2ik_{z,j+1}z_j}}$$

With Fresnel coefficients $$r_{j,j+1} = \frac{k_{z,j} - k_{z,j+1}}{k_{z,j} + k_{z,j+1}}$$

However, real surfaces and interfaces have a certain roughness which can be accounted for by the modified Fresnel coefficient given by

$$r_{real} = r_{ideal} \,.\, e^{-2k_{iz}k_{fz}\sigma^2},$$

where σ is the roughness of the interface.

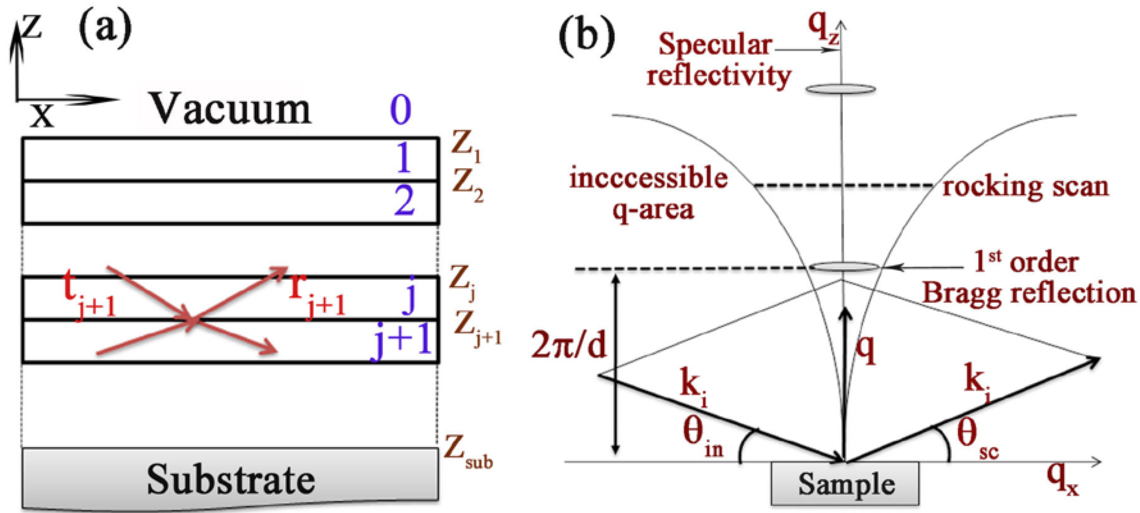

Fig. 2.11: Schematic representation of (a) the recursive formalism by Parrat and (b) the accessible q-area with specular and rocking scan.

The reflectivity in above equation does present periodic oscillations in reciprocal space with $\Delta q_{z,j} = 2\pi/D_j$. The oscillations are the result of constructive interferences between the reflected waves at the interfaces and their period gives the thickness D_j, of the respective layer.

If a film has a periodic structure in the out-of-plane direction the path difference between the reflected waves from two neighboring scattering planes give rise to Bragg reflections according to Bragg condition, $n\lambda = 2d_{film} \sin\theta_{Bragg}$.

A schematic representation of the specular reflectivity geometry is shown in Fig. 2.12. The incident and reflected beams are in one plane and its normal is perpendicular to the normal of substrate surface.

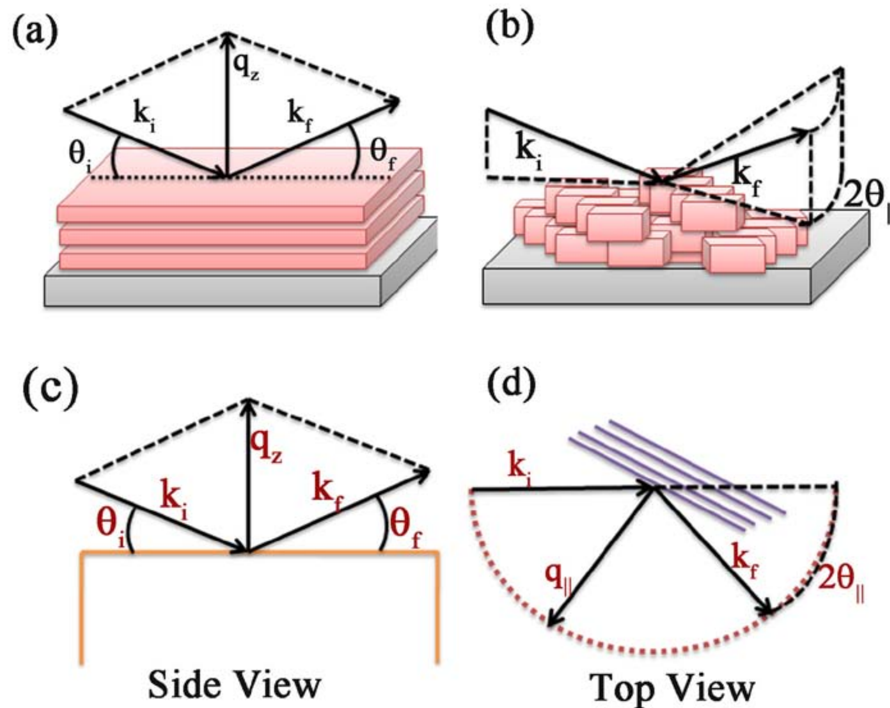

Fig. 2.12: Schematic diagram of (a) specular and (b-d) grazing incidence XRD geometry.(a) For specular geometry $\theta_i=\theta_f$ and the normal of the plane spanned by k_i and k_f. (b) Below the critical angle θc the incoming-ray beam form an evanescent wave which is exponentially damped along the surface normal and which has a component along the interface which give rise to scattering in-plane. (c) and (d) represent a side view and top view of GIDX geometry.

(iii) Grazing incidence X-ray diffraction

As mentioned already above, for $\theta_{in} < \theta_c$ the X-ray reflection is accompanied by an evanescent wave field which propagates along the interface between the two media. The amplitude of this evanescent wave is exponentially damped along the inward surfaces normal with a decay length Λ (typically in the range of few nm)

$$E_t \sim e^{ik_{\|}r_{\|}} e^{(z/\Lambda)}$$

Therefore, GIDX is a surface sensitive diffraction method and by varying the angle of incidence the probed depth of the material can be adjusted. A

schematic representation of grazing incidence geometry is shown in Fig. 2.12(b), Fig. (c) and (d) show a side and top view of GIDX geometry respectively. Since the evanescent wave is propagating laterally, scattering planes in the surface plane can give rise to Bragg reflections.[25]

D. Field-Emission Scanning Electron Microscopy

The field emission scanning electron microscopy(FESEM) is one of the most widely used instruments for material research to observe small structure (~1nm).[26, 27] Principle of electron microscope is the same as optical microscope but instead of using visible light, it uses energetic electrons. However, resolution of optical microscope is limited by its wavelength compared to accelerated electrons which have very short wavelength.[28] The electron can have very small wavelength λ_e which can be changed according to applied voltage. The wavelength λ_e can be written as:

$$\lambda_e = \frac{h}{mV} = \frac{h}{\sqrt{2qmV}} = \frac{1.22}{\sqrt{V}} nm$$

Fig. 2.13: Field Emission Scanning Electron Microscopy (Sigma, Zeiss, Germany)

Here in the Fig. 2.13, we show the photograph of FESEM (Sigma, Zeiss, Germany) which is used in the present work. In FESEM the electron is emitted from a sharp tungsten needle (diameter 10-100nm) by a strong electric field. The acceleration voltage between cathode and anode is ~ 0.5-

TH-1132_08612114

30 kV. As the instrument is operating in high vacuum (less than 10^{-7} mbar) so there is no scattering along the column which helps preventing discharge inside the instrument. Electron emitters from field emission gun were used for FESEM. These types of electron emitters can produce up to 1000 times than the emission of a tungsten filament. After the electrons exit the electron gun, they are collimated by electromagnetic condenser lenses, focused by objective lenses. These electrons strike the sample surface and produce secondary electrons. A secondary electron detector is placed near the sample and it will give morphological image of the sample. FESEM is also equipped with a special objective lens that projects the magnetic field under the lens. A very high resolution is obtained by changing the specimen to sample distance. A secondary electron detector is connected above the objective in-lens (in-lens detector), which differentiates the image with conventional image. A very high resolution image is obtained using in-lens detector.

E. Transmission Electron Microscopy

The transmission electron microscopy (TEM) is based on the diffraction of electrons when they pass through a very thin sample. The principle of the transmission electron microscope is almost the same as an optical microscope, using magnetic lenses instead of glass lenses and electrons instead of photons.[26, 29] An electron beam from an electron gun is focused by a condenser lens onto a small spot (~ 2–3μm) on the sample and after passing through the sample is focused by the objective lens to project the magnified image into the screen. A very essential element is the aperture located at the back focal plane of the objective lens which determines the image contrast and resolution limit of the microscope.[30, 31]

In the simplest view, electron diffraction from a crystalline lattice can be described as a kinematical scattering process that meets the wave

interference conditions given in the Bragg equation. As in the case of x-ray diffraction, the electron diffraction patterns are spot patterns form single crystal films, ring patterns from fine-grain randomly oriented crystallites, and superimposed ring and spot-patterns from larger grain polycrystalline films containing some preferred orientation (textured films).

Our equipment is a 200 keV (FEI Tecnai G^2-F20) high resolution transmission electron microscope (HRTEM) with point-to-point resolution of 0.19 nm and lattice resolution of 0.14 nm. A camera consisting of a yttrium-aluminium-garnet (YAG) scintillator that is fiber-optically coupled to an image intensifier, connected to a high-resolution television tube camera, provides a total magnification of 30 million (microscope magnification~1.5×10^6 and the camera magnification: 20). This magnifying system outputs a video stream that is acquired in a computer with a frame-grabber. An option of using the films is also available.

Due to a limited penetration depth of electrons in solids, the sample should be very thin: the acceptable thickness is about 100-1000Å. To facilitate sample preparation, an ultrasonic disc-cutter, a dimpler, a precision ion-polishing system (all from GATAN, USA), a grinder/polisher unit and wire saw are available. With high-resolution TEM atomic structure can be obtained directly. We have used plan view TEM and high resolution TEM (HRTEM) and selective area electron diffraction (SAED) pattern for the work presented in this thesis.

2.2.2 Spectroscopic Measurements

In this section we will discuss briefly the instruments used for the spectroscopic measurement of the sample.

TH-1132_08612114

A. UV-Vis Spectroscopy

UV-Vis absorption is the measurement of the attenuation of a beam of light after it passes through a sample or after reflection from a sample surface. As the electronic band structure of any material is determined by the optical property of the material. Therefore this technique is very useful to study the absorption or transmission of light by the samples. The UV-Vis spectroscopy is very useful to explore the electronic properties of any material.[26] In this case, the substrate should be transparent as this equipment works at transmission geometry. When we excite the sample with light with different wavelengths, the materials absorb the light corresponding to the energy of band gap or any state intermediate to the band gap. It will show peak at the point of absorption. Fig. 2.14 shows the photograph of the UV-Vis instrument. For my analysis I have deposited the material on corning glass substrate.

Fig. 2.14: Photograph of the Ultraviolet-visible spectroscopy.

B. Photoluminescence Spectroscopy(PL)

Luminescence refers to the emission of light by a material through any process other than black body radiation. The term photoluminescence (PL) means any emission of light that results from optical stimulation.[32]

Photoluminescence is a nondestructive process for the determination of the luminescence property of a material, i.e. following the excitation when the excited states relax. It also can be applied for the determination of the trap level if the trap centers are radiative.[33] The spectral distribution of the sample depends on the electronic transition probability within the different energy level. When we excite any material with energy comparable to band gap or more than that then electrons are transferred to higher energy state. When these electrons return to their equilibrium state, the excess energy is released. The electrons and holes can either recombine non-radiatively by emitting phonons (or transferring energy to other particle) or radiatively emitting photons. The energy of the emitted photon is equal to the difference between two electronic states involved in this transition. This spectroscopy measure the photon counts. An excellent review on PL of crystalline semiconductor is described by G. D. Gilliand.[34]

Fig. 2.15: Photograph of steady state photoluminescence spectrometer. (Thermo Spectronic, AMINCO, Bowman, Series 2)

There is a Xenon lamp inside the instrument. The light is mono-chromated by a mono-chromator. The mono-chromated light is focused by a lens system to the substrate point. The geometry of the measurement is reflection geometry. Output light is collected by a detector. Using the software interface we can change the slit width of incident light as well as the detector slit. In my work, in some cases I have used the Xenon lamp

source, in some cases 480nm Laser source for exciting the sample. For analyzing, the peaks are fitted by Gaussian line shape function using Peak Fit software.

C. Time-Resolved Photoluminescence Spectroscopy

This spectroscopy technique is used to study the exciton dynamics in semiconductor. The basic principle is to use photon from a short pulse laser source to excite the electrons and holes in one instance, which forms excitons. As the excited electrons and holes recombine, this spectroscopy allows one to measure the lifetime of the excitons, i.e. time since it created and time when it annihilated. Knowledge of lifetime of the emitted photons is essential to understand the origin of PL from different samples. Basically it measures the number of photons of fixed wavelength with time. These emitted photons are analyzed by spectrometer and detected by a micro-channel-plate photomultiplier tube (MCP-PMT) detector. Multi Channel Analyzer (MCA) boards in a computer analyze the output pulse voltages into various channels which correspond to different time. By this process, instrument analyzes the received photon at different time. The number of output pulse is directly proportional to incident photon. Fig. 2.16 shows the photograph of TRPL spectroscopy (Life Spec II, Edinburg Inst., UK) used in my study. Here we use nanosecond pulsed pump laser (EPL series, Edinburg Inst., UK) of wavelength 480 nm to measure the PL decay. This instrument has a time resolution of ~ 50ps. The TRPL spectra represent the decay behavior of number of channel available in the sample. The decay equation is expressed as

$$I(t) = I_1 \exp\left(-\frac{t}{\tau_i}\right) + I_2 \exp\left(-\frac{t}{\tau_2}\right) + I_3 \exp\left(-\frac{t}{\tau_3}\right) + \cdots \dots \dots \dots \dots + I_0$$

TH-1132_08612114

Where $I(t)$ is the PL count, $I_1, I_2, \ldots$ are decay channel amplitude, $\tau_1, \tau_2, \ldots$ are the decay time constant and I_0 accounts for the background noise.

Fig. 2.16: Photograph of time resolve spectroscopy (Life Spec II, Edinburg Inst., UK)

2.3 Designing and development of photocurrent and photoresponse measurement setup

To study the electrical, photo electrical and photo-detection property of organic sample we designed photocurrent and photoresponse setup. The photograph of the setup is shown in the Fig. 2.16 and the schematic diagram of the operation is shown in the diagram 2.17.

Fig. 2.16: Photograph of the photocurrent and photoresponse measurement setup.

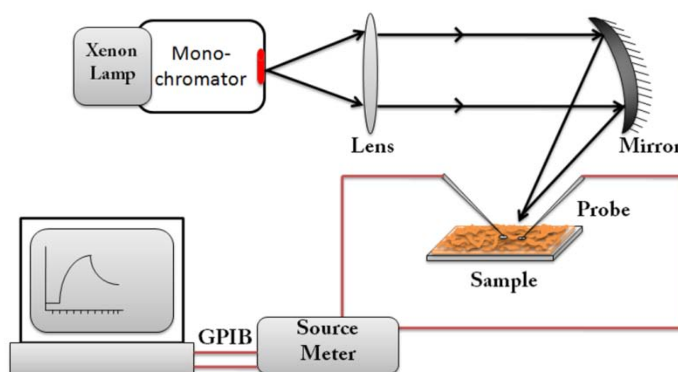

Fig. 2.17: Schematic diagram of in-house developed Photocurrent measurement setup

The setup consists of a light source, electrical contact, two probe probe-station, Keithley sourcemeter with computer interface. Monochromated UV-Vis light from 150W Xenon lamp is used for exciting the sample. The monochromated light is tightly focused to the small area of the sample using a combination of convex lens and a concave mirror. Sample is placed on probe station (EPS 500, Ecopia, South Korea) vertically. The electrical connection was made by silver contact along with two tungsten microprobes of diameter 1.5μm. The monochromated light is tightly focused in between the Ag contacts. For wavelength dependent photocurrent measurement we fixed the bias voltage and by changing the wavelength just note down the current value. The photo current is measured using picoammeter (Keithley 6487, USA) and the instrument supplies the necessary bias voltage. All the measurements were done at room temperature.

2.4 Statistical analysis of rough surfaces

When atoms or molecules are deposited on the substrate surfaces, they make the surface rough as it is always a random deposition. In order to understand the evolution of the surface during growth it is essential to understand the characteristics of rough surface profile. Mathematically a

rough surface is described by the surface height profile *h(x,t)*, where h denotes the surface height with respect to the substrate at a portion *x* on the surface at time *t*.

In this section, we describe the various statistics used to characterize rough surface. We will also describe how the heights are correlated which enables one to calculate different scaling exponents.

(i) Average height

The average surface height is the arithmetic average of surface heights. Analytically it can be expressed as

$$\overline{h(t)} \equiv \langle h(x,t) \rangle$$

Where *h(x,t)* is the height of a point *x* and time *t*, ⟨⟩ signifies the average over large no of points. In order to nullify any artificial effect in calculation the average surface height it is better to make $\overline{h(t)} = 0$ by choosing suitable reference height. If the deposition rate is constant, then the average height increases linearly with time i.e. $\overline{h(t)} \approx t$.

(ii) Interface Width

Interface width is the most important parameter to specify the roughness of any surface. It is defined as the standard deviation *w* of the surface height. In other way it is defined as root mean square roughness of any surface. The mathematical form is

$$w(t) \equiv \sqrt{\langle [h(r,t)]^2 \rangle}$$

Where *h(r,t)* is the height at particular position at particular time t. Larger the value of *w* signifies larger roughness. In other way it is defined as

$$w(t) \sim t^{\beta}$$

TH-1132_08612114

This is the power law dependence of interface width and β is defined as growth exponent according to the dynamic scaling theory. This is an important parameter which is essential to specify the thin film growth.

(iii) Autocorrelation function

The above mentioned two parameters specify the vertical property of a surface. So in order to know the correlation in longitudinal direction an important parameter is defined as

$$R(r,t) \equiv w^{-2}\langle[h(x,t)h(x+r,t)]\rangle$$

Where each h signifies the heights in two consecutive points separated by a distance r.

(iv) Lateral correlation length

The lateral correlation length ξ is defined as the value of r, where $R(r,t)$ decrease to $1/e$ of its original value.

$$R(\xi,t) \equiv e^{-1}$$

If the distance between two surface points is within ξ, the heights at these two points can be considered as correlated. If the distance is more than these, two surface points are independent of each other. The time dependent behavior of the lateral correlation length is obeying power law as

$$\xi(t) \sim t^{1/z}$$

Where $1/z$ is defined as dynamic exponent. In other way the lateral correlation function (ξ) is defined as the length beyond which surface heights are not significantly correlated. For mound type surface it is essentially the size of the mound. The physical significance of these parameters is shown by the schematic surface profile in Fig. 3.1.

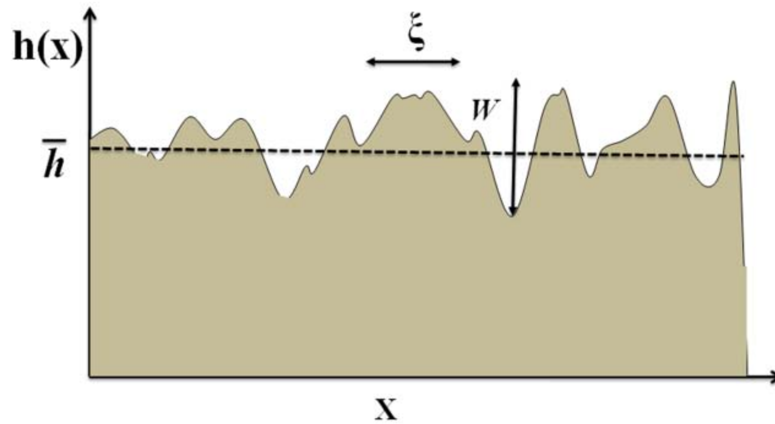

Fig. 3.1: Schematic diagram of a rough surface. The significance of average height, lateral correlation length (ξ) and interface width (w) is shown here.

(v) Height-height correlation function

The simplest way to calculate the height-height correlation function for an isotropic surface as the mean square of height difference between two surface positions separated by a distance r for coverage of the molecule (θ) is

$$G(r,\theta)=\langle [h_i(r,\theta)-h_j(0,\theta)]^2\rangle$$

Where each h signifies the heights of two consecutive points separated by a distance r and averaged over pairs of points i and j.[35] For small r, height-height correlation function is defined as $\boldsymbol{G(r) \sim [m(\theta)r]^{2\alpha}}$ with $r \ll \xi$, where ξ is defined as lateral correlation length, α is the roughness exponent and m is the local slope of the surface profile. The growth of the molecules with local slope $m(\theta)$ independent of the coverage is said to be stationary.[36, 37] On the other hand, for non-stationary growth $m(\theta)$ increases with time and an up-shift of $G(r)$ is observed.

2.4.1 Calculation of correlation functions from AFM images

In order to calculate $G(r, \theta)$ we use AFM images. The AFM images are essentially a three dimensional matrix containing x, y and z. In our

TH-1132_08612114

calculation it consists of 512×512 data points, each point containing consecutive height value. Here in the Fig. 3.2(a) we show a typical AFM image of Ag film. The line scan profile of the surface is shown in Fig. 3.2(b). By extracting the matrix from the image and using MATLAB programming we calculate height-height correlation function. The height-height correlation function is defined along the fast scan direction (assumed to be x direction) as[38]

$$G(r) = \frac{1}{N_y(N_x - p)} \sum_{i=1}^{N_y} \sum_{n=1}^{N_x - p} [h(p+n,l) - h(n,l)]^2$$

Where, N_x & N_y = No of data points in X &Y direction respectively

p= Distance within which surface scan is obtained.

h = Height at particular points.

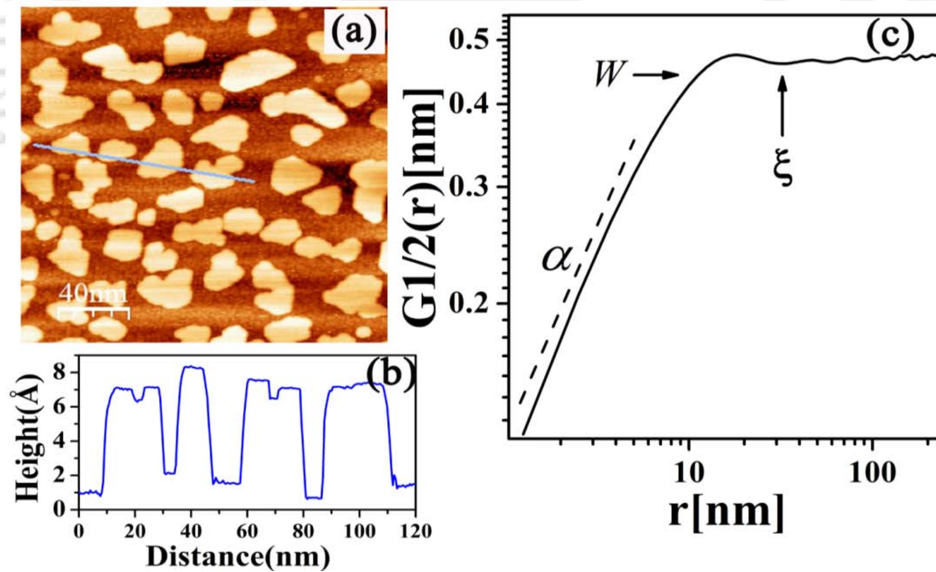

Fig. 3.2: (a)Typical AFM image of Ag film grown on Si substrate (b) line scan profile of the AFM image (c) square root of height-height correlation function plot of the AFM images. The different scaling exponents are shown here.

Here in the Fig. 3.2(c) we show a typical plot of square root of height-height correlation function. Form the slope of the linear portion we got roughness exponent. We calculate the lateral correlation length (ξ) from first deep position after the linear portion and interface width (w) by the value of y where $G^{1/2}(\xi/2)$.[39-41]

TH-1132_08612114

2.5 References

1. D. K. W. Kolasinski, *Surface Science: Foundations of Catalysis and Nanoscience* (John Wiley & Sons, Chichester, 2008).
2. D. h. c. H. Lüth, *Solid Surfaces, Interfaces and Thin Films* (Springer, New York, 2010).
3. K. Seshan ed., *Handbook of Thin-Film Deposition Processes and Techniques Principles, Methods, Equipment and Applications* (Noyes Publications, New York, 2002).
4. M. A. Herman and H. Sitter, *Molecular Beam Epitaxy: Fundamentals and Current Status* (Springer, New York, 1996).
5. K. Oura, V. G. Lifshits, A. A. Saranin, A. V. Zotov, and M. Katayama, *Surface science* (Springer-Verlag, New York, 2003).
6. H. Ibach, *Physics of Surfaces and Interfaces* (Springer, New York, 2006).
7. D. K. Goswami, B. Satpati, P. V. Satyam, and B. N. Dev, Current. Sci. **84**, 903 (2003).
8. J. M. Lafferty, *Foundations of Vacuum Science and Technology* (John Wiley & Sons, Toronto, 1998).
9. A. Chambers, R. K. Fitch, and B. S. Halliday, *Basic Vacuum Technology* (IOP Publishing Bristol 1998).
10. S. Amelinckx, D. v. Dyck, J. v. Landuyt, and G. v. Tendeloo, *Handbook of Microscopy* (VCH, Germany, 1997).
11. M. D. Ventra, S. Evoy, and J. R. H. Jr. eds., *Introduction to Nanoscale Science and Technology* (Kluwer Academic Publishers, Boston, 2004).

12. R. Wiesendanger, *Scanning Probe Microscopy and Spectroscopy: Methods and applications* (Cambridge University Press, New York, 1994).
13. D. Sarid, *Scanning Force Microscopy With Applications to Electric, Magnetic and Atomic Forces* (Oxford University Press, New York, 1994).
14. P. Eaton and P. West, *Atomic Force Microscopy* (Oxford University Press, New York, 2010).
15. R. García, *Amplitude Modulation Atomic Force Microscopy* (Wiley-VCH, Weinheim, Germany, 2010).
16. B. E. Warren, *X-Ray Diffraction* (Devour, New York, 1990).
17. B. D. Cullity and S. R. Stock, *Elements of x–ray diffraction* (Prentice Hall, New Jersey, USA, 2001).
18. U. Pietsch, V. Holý, and T. Baumbach, *High-resolution X-ray Scattering from Thin Films to Lateral Nanostructures* (Springer, New York, 2004).
19. J. Daillant and A. Gibaud, *X-Ray and Neutron Reflectivity: Principles and Applications* (Springer-Verlag, Berlin, 2009).
20. J. K. Basu and M. K. Sanyal, Phys. Rep. **363**, 4675 (1999).
21. J. Als-Nielsen and D. McMorrow, *Element of modern X-ray physics* (Wiley, Chichester, 2001).
22. M. Tolan, *X-Ray Scattering from Soft-Matter Thin Films: Materials Science and Basic Research* (Springer, Berlin, 1999).
23. L. G. Parratt, Phys. Rev. **95**, 359 (1954).
24. L. G. Parratt and C. F. Hempstead, Phys. Rev. **94**, 1593 (1954).
25. M. Birkholz, *Thin Film Analysis by X-Ray Scattering* (WILEY-VCH, Weinheim, 2006).
26. T. Pradeep, *NANO: The Essential* (McGraw-Hill Education, Chennai, 2007).

TH-1132_08612114

27. L. Reimer, *Scanning Electron Microscopy Physics of Image Formation and Microanalysis* (Springer, New York, 1998).
28. W. Zhou and Z. L. Wang, *Scanning Microscopy for Nanotechnology Techniques and Applications* (Springer, New York,USA, 2006).
29. J. Ayache, L. Beaunier, J. Boumendil, G. Ehret, and D. Laub, *Sample Preparation Handbook for Transmission Electron Microscopy Techniques* (Springer, New York, 2010).
30. D. B. Williams and C. B. Carter, *Transmission Electron Microscopy: A Textbook for Materials Science* (Springer, 2009).
31. B. Fultz and J. Howe, *Transmission Electron Microscopy and Diffractometry of Materials* (Springer, Berlin Heidelberg, New York, 2007).
32. L. Ozawa, *Cathodoluminescence and Photoluminescence, Theories and Practcal Applications* (CRC Press, New York, 2007).
33. D. K. Schorder, *Semiconductor Material and Device Characterization* (Wiley-Interscience, New Jersey, USA, 2006).
34. G. D. Gilliland, Mat. Sci. Egg. R **18**, 99 (1997).
35. J. Lapujoulade, Surf. Sci. Rep. **20**, 191 (1994).
36. M. Pelliccione and T.-M. Lu, *Evolution of thin film morphology: modeling and simulation,* (Springer-Verlag, New York, 2008).
37. J. H. Jeffries, J.-K. Zuo, and M. M. Craig, Phys Rev Lett **76**, 4931 (1996).
38. Y. Zhao, G.-C. Wang, and T.-M. Lu, *Characteriztion of Amorphus and Crystalline Rough Surface: Principles and Application* (Academic Press, London, 2001).
39. T. K. Chini, D. P. Datta, and S. R. Bhattacharyya, J. Phys.: Condens. Matter **21**, 224004 (2009).

TH-1132_08612114

40. I. J. Lee, M. Yun, S.-M. Lee, and J.-Y. Kim, Phys. Rev. B **78**, 115427 (2008).
41. D. P. Datta and T. K. Chini, Phys. Rev. B **69**, 235313 (2004).

TH-1132_08612114

Chapter III

Growth of TC-PTCDI-C_8 films on SiO_2 surface

3.1 Introduction

There has been increased emphasis in electronic devices based on organic semiconductor molecules. The performance of organic devices depends not only on molecule itself but also on the arrangement of molecules in the films. There are many open questions and challenges related to the understanding of the growth mechanisms and physical principles of molecular ordering in the organic films. Therefore, the study of growth of organic molecules on different substrate surfaces has attracted lot of attention of many investigators in last few years.[1-6] In contrast to inorganic systems, whose growth mechanisms have been solidly established and successfully exploited to control the growth, organic thin film growth is definitely more complex due to the anisotropy and their weaker van der Waals interaction potentials. In such systems, fundamental concepts typically employed for inorganic materials such as strain or epitaxy are not defined well. Several models have been proposed to understand the growth mechanism, however, it remains poorly understood and requires detail investigations from molecular level to a thick film growth.

TH-1132_08612114

The evolution of surface morphology during the growth has been subject of extensive theoretical as well as experimental studies during last few decades.[7-13] These studies relate the thin film growth mechanism to a set of scaling exponents describing the dependence of the surface roughness on film thickness and their lateral length scale.[14-16] While there has been a lot of research on the process of kinetic roughening leading to different surface morphology,[17] there has been much recent experiments and theoretical interests in a different mode of surface growth for organic materials thin films involving the formation of 'mounds' which are pyramid like or flat top structures.[4] The precise experimental conditions that determine whether the growth morphology would be kinetically rough or dominated by mounds are presently not understood properly. Recently some experimental studies have contributed to enhance the molecular-scale understanding of organic growth. A usually rapid growth of vertical roughness and lateral correlations has been observed for DIP (diindenoperylene) thin films grown on SiO_2.[7] Zhang et al. show evidences for a thickness dependence of the interlayer mass transport caused by molecular reorientations during the first stages of the growth as the origin for the morphological evolution with thickness.[18] Hlawacek et al. have concluded a gradual increase of Ehrlich-Schwöbel (ES) barrier with thickness as the origin of a strong trend toward mound formation, which was ultimately attributed to changes in the molecular tilt.[19] Formation of 3D steep-edged island on top of initial wetting layer of thickness of one or few monolayers has also been observed on organic thin film growth and explained by different effective step edge binding energy of strained layer and unstrained layer.[4]

In this chapter we discuss the growth kinetics of 2D layer-by-layer to 3D flat top mound formation of *N,N'*-bis(octayl) perylene-1,6,7,12-tetrachloro-3,4:9,10-bis-(dicarboximide) (TC-PTCDI-C_8) on SiO_2 substrates.

TH-1132_08612114

These mounds are essentially 2D multilayer structures. We have observed that the initial stage of the growth is layer-by-layer up to two molecular layers and then 3D flat top mounds start forming. The morphology evolution during this transition has been represented with the roughness scaling exponents (α), which was calculated from the height-height correlation function of the surface profiles. The value of α was calculated for this two stages of the growth and found to be 0.68±0.02 corresponding to layer-by-layer growth and 0.85±0.05 for the flat top mound growth. This suggests a transition of growth kinetics, which is essentially due to the dynamic behavior of local surface slopes (m) associated with layer dependent ES barrier.

3.2 Experimental

We have deposited TC-PTCDI-C_8 on Si(100) surfaces with native oxide layer by physical vapor deposition in ultra-high-vacuum (base pressure ~ 10^{-10} mbar). The chemical structure of this molecule is shown in Fig. 1.8. The molecule is about 30.1 Å long including the chains connected with the perylene core, where as it is about 8.9 Å along the width of the molecule. The substrates were cleaned ultrasonically with acetone, ethanol and water and then dried with nitrogen gas. Subsequently, the samples were annealed under vacuum above 500°C for 12 hours and slowly cooled to the growth temperature. As-received molecules were purified by gradient sublimation before use. The film coverage and the growth rate were controlled by means of a calibrated quartz crystal monitor (QCM). A monolayer (ML) is defined as the thickness of the layer when a complete one layer is formed. We have used two different substrate temperatures during the growth: room temperature (T_{sub}= RT) and an elevated temperature (T_{sub} = 75°C). The deposition rate was about 2.5Å/min. The surface morphology was measured

TH-1132_08612114

using contact mode AFM (atomic force microscopy) (Digital Instruments NanoScope III SPM) *ex-situ*. Repeated scans with a small force set point were carried out in order to avoid damage of the molecular film by tip sample interaction. X-ray reflectivity (XRR) and grazing incidence x-ray diffraction (GIXD) measurements were performed *ex-situ* at the synchrotron source Angströmquelle Karlsruhe (ANKA) of the Karlsruhe Institute of Technology (KIT) with a wavelength of λ = 1.24 Å.

3.3 Results and Discussions

3.3.1 RT Growth of TC-PTCDI-C_8 on SiO_2 substrate

A. AFM Results

Fig.3.1 shows the AFM image of TC-PTCDI-C_8 films grown on SiO_2 substrates while substrate was kept at RT. .

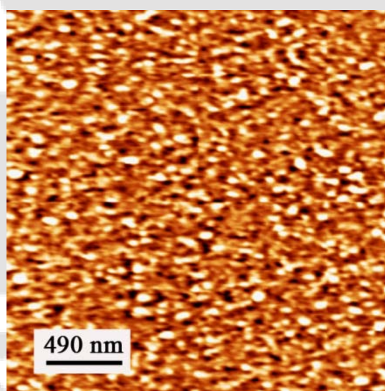

Fig. 3.1: Contact mode AFM image of TC-PTCDI-C_8 film grown at room temperature (Scan area 2μm×2μm).

A rough film with small grain boundaries is observed. This essentially means a poor molecular order within the film and therefore, no molecular terraces are observed.

B. X-ray reflectivity Results

From the morphology of TC-PTCDI-C_8 films as observed in AFM images, it is difficult to understand the molecular arrangement within the

films. In that regards, x-ray reflectivity measurement is a very sensitive technique to understand the molecular arrangements as well as total thickness of the films. Therefore, we have carried out XRR measurements on the film using synchrotron x-radiation of wavelength λ=1.24Å. Fig. 3.2 (a) shows the normalized XRR intensity with vertical component of scattering vector (q_z). No Bragg peaks was observed in the XRR data. The data were

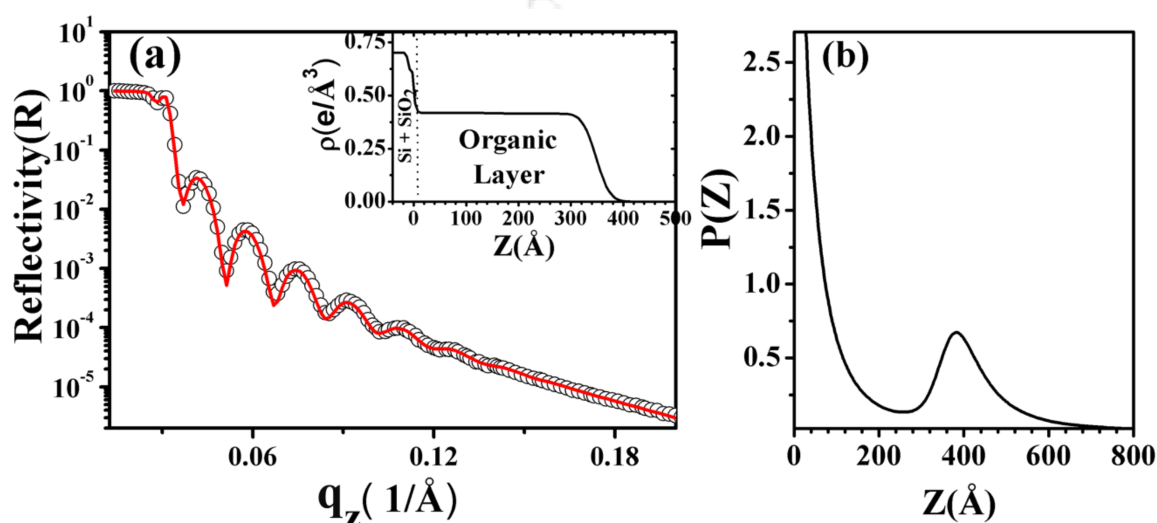

Fig. 3.2: (a) X-ray specular reflectivity spectra of TC-PTCDI-C_8 film grown at RT on SiO_2 substrate. The red curve corresponds to the fitted intensity using Parratt formalism. The electron density profile is shown in the inset of the graph. The average thickness of the film calculated from the electron density profile is 360Å. (b) The Patterson function plot of the RT sample calculated from the XRR data. The average thickness of the film calculated is 360Å.

collected covering higher q_z, Fig. 3.2(a) only shows the data at the lower Q_z. Keissig fringes are observed as seen from the figure. These fringes arise due the total thickness of the films. We have used Parratt formalism to fit XRR data. The solid line in Fig. 3.2(a) is the fitted result. The electron density profile used to fit XRR data is shown in the inset of Fig. 3.2(a). The average thickness of the films estimated from the fitting is 360 Å. In order to verify our result measured from the Parratt formalism, we have calculated the Patterson function which is shown in Fig. 3.2(b). It is defined as the Fourier transform of the reflectivity normalized by Fresnel reflectivity. The Fresnel

TH-1132_08612114

Reflectivity is defined as the total reflectivity from substrate. The broad peak observed in the Patterson function plot represents the average thickness of the film. The average thickness of the film calculated from the peak position of the Patterson function plot is ~ 360Å, which confirms the thickness obtained from XRR fitting.

3.3.2 Growth of TC-PTCDI-C_8 on SiO_2 substrate at 75°C substrate temperature

A. AFM Results

Atomic force microscopy (AFM) measurements were carried out on different stages of growth to study the morphology evolution. Fig. 3.3 shows some representative contact mode AFM images of TC-PTCDI-C_8 thin films evaporated on SiO_2 substrate while the substrate temperature was maintained at 75°C. Growth of first monolayer is shown in Fig. 3.3(a) for coverage 0.75 ML. Formation of percolated molecular terraces are observed and some uncovered parts of the substrate are still visible. The roughness of the surface morphology calculated from the whole image is about 11.5 ± 0.3 Å. This represents the average height of surface fluctuations. A typical line scan is shown below the AFM image. This is representing the height fluctuation along the line drawn over the image. The roughness observed here is considerably smaller than the size of the molecule and this discloses that the molecules are tilted with respect to surface normal. The tilted arrangement of perylene cores has been considered in the analogy with the structures of PTCDI-C_8 films.[20, 21] For the case of 1.5 ML films, growth of the first molecular layer is completed which was incomplete in the case of 0.75 ML sample. Some terraces are started forming on top of the first layer as shown in Fig. 3.3(b).

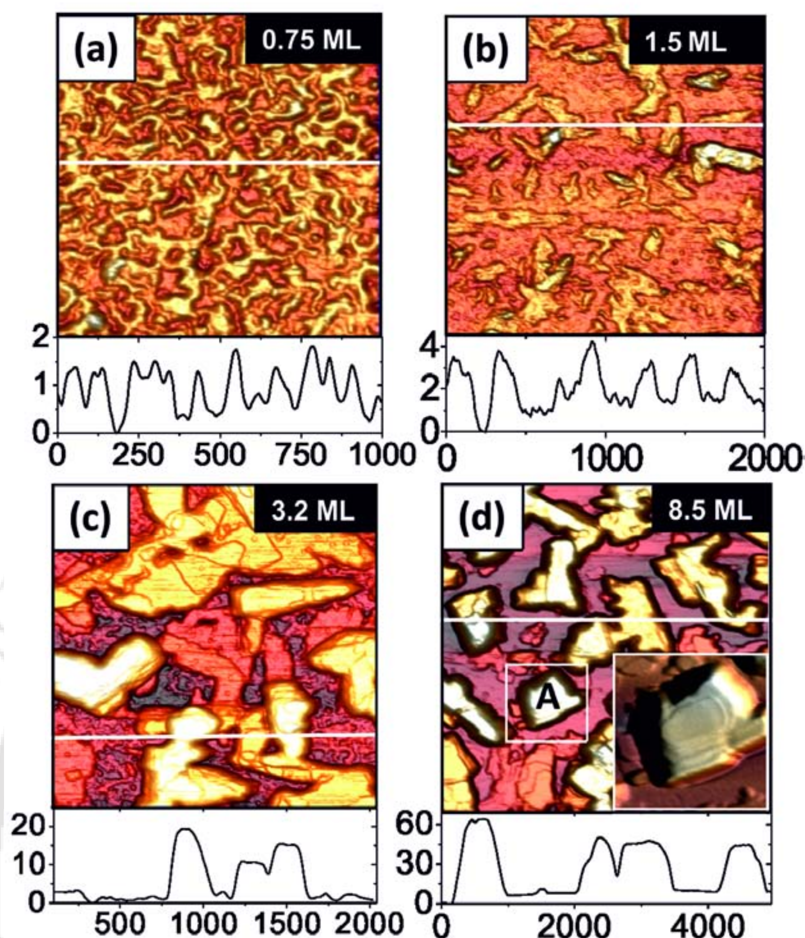

Fig. 3.3: Contact mode AFM image of TC-PTCDI-C_8 film grown at 75°C on SiO_2 substrate with four different coverages (a) 0.75 ML, (b) 1.5 ML, (c) 3.2 ML and (d) 8.5 ML. The line scan profile of each of the sample is shown in down of each image. The scan area are for (a) 1×1μm, (b, c) 2×2μm and (d) 5×5μm. The mound formation is shown in the inset of (d) which is the zoom region marked as A. Here all the scales in line scan profile are in nm.

With further growth, these terraces increase in size and height developing into mounds with a flat top as shown in Fig. 3.3(c) and (d) for 3.2 ML and 8.5 ML coverage, respectively. It can be seen that these mounds have a layered structure. Molecular steps are visible in a closer view for the mound marked as “A” in the inset of Fig. 3.3(d). Height scans along the line drawn on for every AFM images are shown below the corresponding AFM images to understand the height variation of the mounds. One can readily observe that mounds coalesce and course with coverage and form bigger mounds in size.

B. X-ray reflectivity Results

(i) Out of plane Structure

X-ray specular reflectivity (XRR) measurements were performed in order to determine the average height of the interlayer spacing for thick mounds and thickness of underlying layer. XRR measurements were performed ex-situ for all four samples. Fig. 3.4 shows the x-ray reflectivity data taken from 0.75 ML and 1.5 ML samples. Electron density profile has

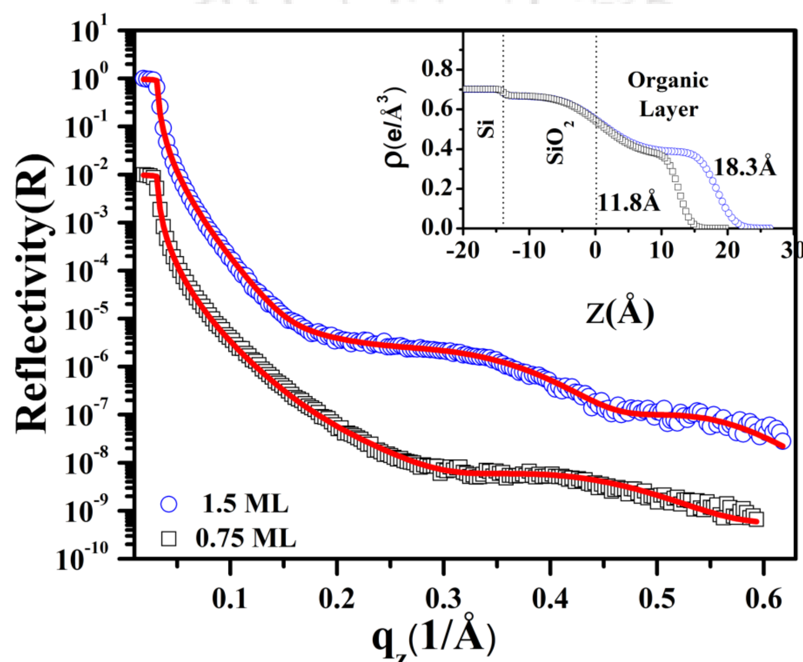

Fig. 3.4: X ray reflectivity spectra of TC-PTCDI-Ph film grown on SiO_2 at 75°C temperature with two different coverage 0.75 ML and 1.5 ML. The red line corresponds to the fitted curve of the XRR spectra using Parratt formalism. The electron density profile is shown in the inset of the graph.

been obtained from a fit of the XRR intensity by Parratt formalism, which is shown in the inset. From the electron density profile it can be estimated that the average thickness of the organic film for 0.75 ML sample is 11.8 Å. This is consistent with the result obtained from the AFM measurement. However, a closer look at the line scan of this sample showed in Fig. 3.3(a) revealed that height of individual terraces is larger than 11.8 Å. The height observed by the XRR analysis is essentially the roughness of the sample. The

growth of this layer is completed at coverage of 1.5 ML. Fig. 3.3(b) shows the representative image of 1.5 ML sample. The thickness of this complete layer is 18.3 Å, which is obtained from XRR fitting. Molecular terraces grown on top of this layer, as shown in the Fig. 3.3(b), do not contribute significantly to specular XRR data and are being considered as roughness of the sample.

Specular XRR data taken from the 3.2 ML and 8.5 ML samples are shown in Fig. 3.5. Up to fourth order Bragg peaks are observed for both the samples. The second order Bragg peak for 3.2 ML sample is not observed.

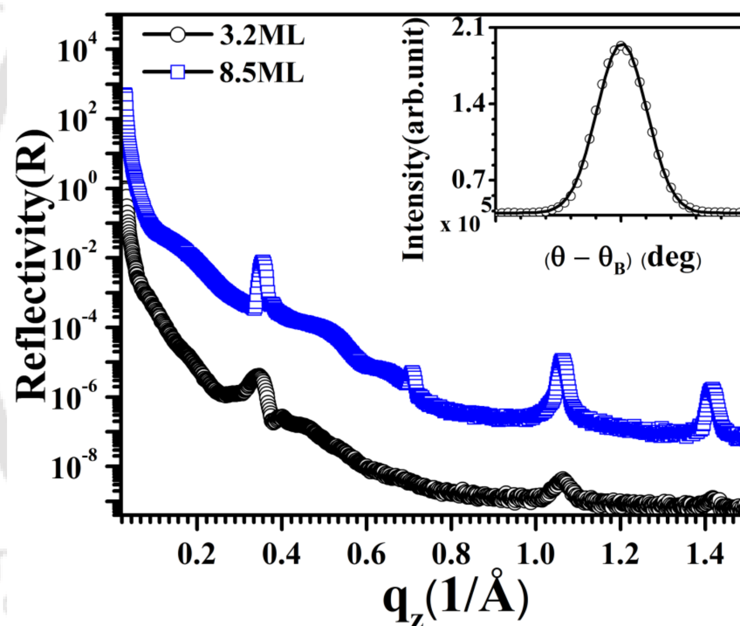

Fig. 3.5: X ray reflectivity spectra of TC-PTCDI-C_8 sample grown at 75°C with two different coverage 3.2ML and 8.5 ML. Intense forth order Bragg peak is observed. The Rocking scan profile of the first order Bragg peak for 8.4ML coverage shown in the inset of the graph.

This peak is less intense peak and is suffering of poor statistics in reflectivity data. Rocking curve obtained from the 8.5 ML samples at the first order Bragg peak position (inset of Fig. 3.5) showed an average mosaicity of 0.009° that revealed the excellent molecular alignment along the

surface normal direction. Bragg peaks appearing on the reflectivity data stem from the layered structure of the mounds and are associated with a spacing of d = 18.8 Å between the adjacent molecular layers i.e. average layer height. XRR data at lower q_z (below first order Bragg peak) is fitted using Parratt formalism for 8.5 ML sample. Fig. 3.6 shows the XRR fitting and the electron density profile obtained from XRR fitting. This is shown in the inset. The thickness obtained from this fitting is 36.7 Å. This is essentially

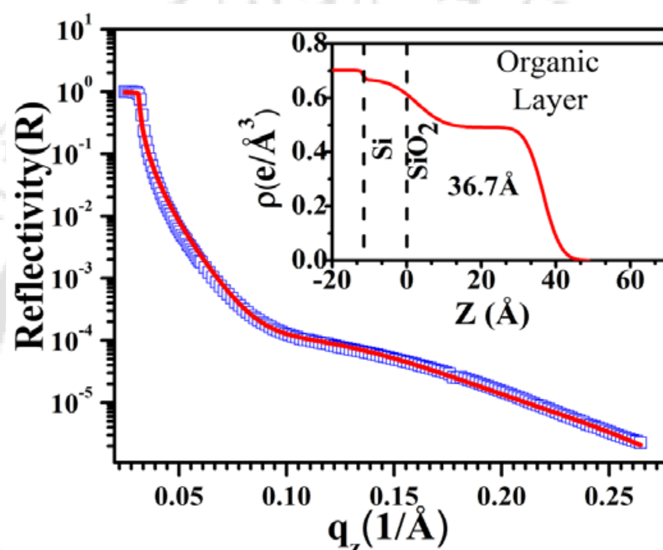

Fig. 3.6: X-ray reflectivity spectra up to 1st order Bragg peak of 8.5 ML coverage sample. The red curve signifies the fitting line using Parratt formalism. The electron density profile due to fitting is shown in the inset of the graph.

the thickness of the layer. The contributions of mounds to the specular reflectivity are not significant at lower q_z. However, they contribute at higher q_z and therefore we observed Bragg peaks. Moreover, mounds cannot be considered as roughness because contribution from the rough surface to the reflectivity is meaningful for small variation of layer thickness with root-mean-square (rms) thickness deviation (σ) < $\lambda/2\pi \sin(\theta)$, where λ is the X ray wavelength and θ is the grazing angle.[22, 23] If we consider the critical angle (θ) of the film, which is 0.36 degrees, the calculated σ would be around 3 nm. However, the average sizes of the mounds are about 10 times higher

TH-1132_08612114

than this value. Thus we can assume that the only layer contributes to reflectivity at lower q_z. The thickness of this layer obtained from the XRR fitting is 36.7 Å. This layer essentially contains two molecular layers as thickness of the first layer obtained from 1.5 ML sample is 18.3 Å. It is difficult to obtain a model to fit XRR intensity at lower q_z for the sample 3.2 ML. This is partially because some flat mounds with lower thickness contribute to XRR and modulate the intensity.

In order to calculate the thickness of the layer for this sample, we calculated Patterson functions $P(z)$ form both the sample for entire range of measured q_z's which are shown in Fig. 3.7. The peaks observed with a period 18.8Å matches the position of the first order Bragg peak.

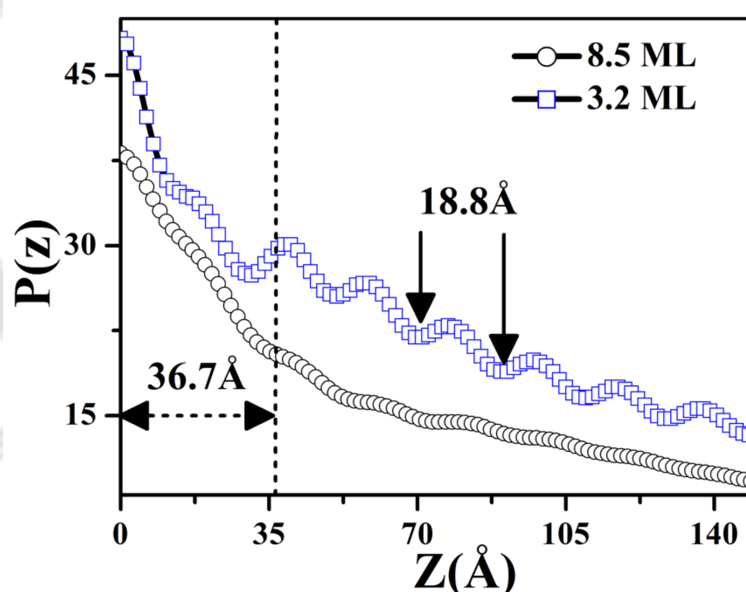

Fig. 3.7: The Patterson function plot of XRR spectra of the sample 3.2 ML and 8.5 ML. The width of the oscillation is 18.8Å which comes from the Bragg peak and under-laying layer thickness is 36.7Å

These peaks are evident along the entire film profile, indicating that the periodicity exists throughout q_z direction. Patterson function also shows the second weak peak around 36.7Å position. This peak corresponds to the layer

thickness, which well agrees with the thickness observed from the reflectivity fitting for 8.5 ML sample. As the Kiessig fringes observed in the reflectivity data obtained from the 3.2 ML sample are not very strong, the calculated Patterson function does not show strong layer peak. However, we can see a shallow modulation around 36.7 Å which corresponds to the thickness of the layer. From combined analysis of reflectivity fitting together with Patterson function calculation one can conclude that TC-PTCDI-C_8 molecules initially grow layer-by-layer on the SiO_2 surface of two molecular layers and then start forming flat top mounds on further growth.

(ii) In-Plane structure

In order to understand in-plane molecular arrangements, high-resolution AFM images were obtained on top of the mounds. Fig. 3.8(a) shows an AFM

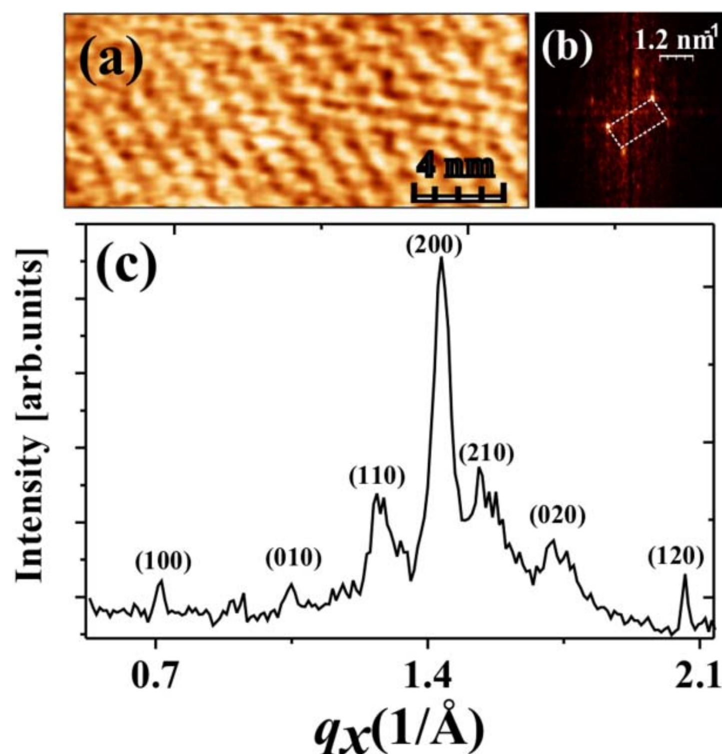

Fig. 3.8: (a) High resolution AFM spectra on the top of a mound of TC-PTCDI-C_8 sample. The molecular arrangement is shown here. (b) The FFT image of the high resolution AFM image from where the unit cell dimension determined. (c) In plane XRD spectra of the TC-PTCDI-C_8 film grown on SiO_2 substrate. The different planes of the spectra are specified here.

image showing molecular arrangement on surface of 8.5 ML sample. This clearly revealed molecular periodicity at the top of the mounds. Fast Fourier Transform (FFT) image of this AFM image is shown in Fig. 3.8(b). The bright spots reflect in-plane molecular periodicity. Based on the symmetry of the bright spots, rectangular unit cell is marked in the FFT image by solid lines. The lattice constants obtained from the FFT image are a = 11.2±0.2 Å and b = 6.5±0.3 Å in real space.

In order to determine with accuracy the in-plane molecular ordering, x-ray diffraction measurements were carried out at grazing incidence geometry, which is shown in Fig. 3.8(c). Error bars were calculated considering statistical errors by including multiple images. Considering a and b are the in-plane lattice constants, we have identified the in-plane x-ray diffraction peaks. The results are shown in Fig.5(c) with lattice constant a = 10.9 ±0.2 Å and b = 6.2 ±0.3 Å which are consistent with AFM results within the error bar.

C. Statistical Analysis of surface morphology

In order to gain insight into the dynamic behavior of the detailed growth processes, we determine the roughness scaling exponents and local surface slope. These quantities are determined from height-height correlation function, $G(r, \theta)$ which is defined as mean square of height difference between two surface positions separated by a distance r for the coverage (θ) of the molecule as $G(r, \theta)= \langle[h_i(r, \theta)-h_j(0, \theta)]^2\rangle$ where $h_i(r, \theta)$ and $h_j(r, \theta)$ are the heights of the surface at the locations separated by a distance r and the brackets signify an average over pairs of points i and j.[24-26] For the small r, height-height correlation function $G(r,\theta)\sim[m(\theta)r]^{2\alpha}$ with $r \ll \xi$, where, ξ is the lateral correlation length scale, α is the roughness scaling exponent and $m(\theta)$ is the local slope of the surface profile for small length scale.[24]

TH-1132_08612114

Lateral correlation length (*ξ)* is the measure of the length beyond which surface heights are not significantly correlated. For the mounded surfaces, this is essentially the size of the mounds.[24] Growth of the molecule with local slope *m(θ)* independent of the coverage is said to be stationary. In such cases, height-height correlation function coincides for $r << \xi$. This signifies the layer-by-layer growth. On the other hand, if the local slope *m(θ)* increases with time, an up-shift of $G(r)$ is observed as film thickness increases.[24, 27] This signifies non-stationary growth by mound formation. Examples of $G(r)$ calculated from the AFM images for different coverage are plotted in Fig. 3.9. In order to avoid sampling induced effect in the $G(r)$, care has been taken to include many AFM images in the averaging of $G(r)$ data. In our analysis we have checked that 6 to 10 AFM images from each sample were enough to give statistically reliable data to obtain $G(r)$ plot. Fig. 3.9 show $G^{1/2}(r)$ Vs. r plots for all the coverage. Following the method discussed before and mentioned in ref[28-30] , we define the surface roughness amplitude W (shown by arrow marked in Fig. 3.9) as the value of $G^{1/2}(r)$ at the first local maximum, $w = G^{1/2}(\xi/2)$ where ξ marked by an upward arrow is the position of r at the first local minimum of $G^{1/2}(r)$. This definition of roughness amplitude is preferred over the large r limit of $G(r)$ because artifacts at large length scales can affect AFM data. The roughness exponent α was determined from a fit to the linear part of the log-log plot of $G^{1/2}(r)$ vs r. We have observed that the value of α for the first two samples (0.75 ML and 1.50 ML) is 0.68±0.05 and 0.85±0.02 for the samples with coverage 3.2 ML and 8.5 ML. In addition, we also noted that $G^{1/2}(r)$ coincides for $r << \xi$ with constant local slope for first two samples whereas the samples with higher coverage show an up-shift in $G^{1/2}(r)$ for $r << \xi$. In this case the local slope also increases with increasing coverage maintaining the roughness exponent constant. This clearly indicates stationary growth for the

first two samples and non-stationary growth for higher coverage. The calculated α (0.68±0.05) for stationary growth is consistent with the commonly reported values for organic growth.[7, 10]

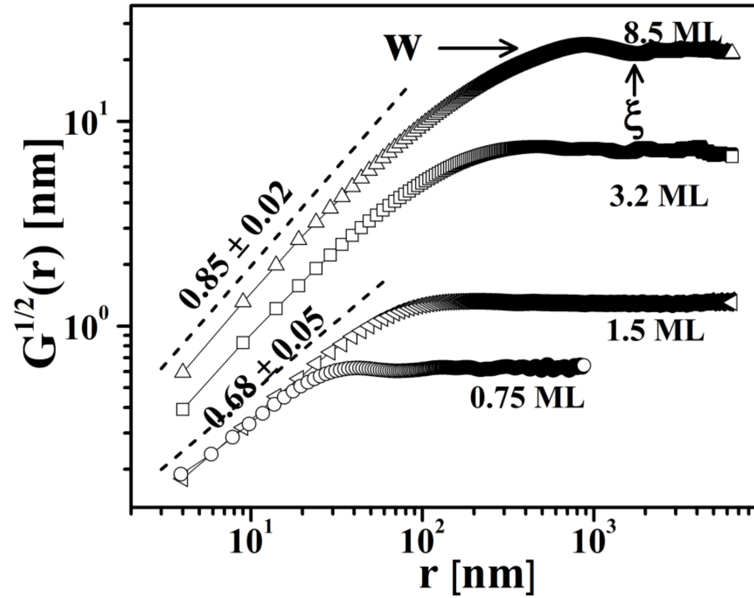

Fig. 3.9: Square root of height-height correlation function calculated from AFM images of different coverage of TC-PTCDI-C_8 film grown at 75°C on SiO_2 substrate. Roughness exponent is calculated from the slope of the linear portion.

This value also agrees well with kinetic roughening in the observed Kardar-Parisi-Zhang (KPZ) universality class for which $\alpha \approx 2/3$.[9] The changes in local surface slope indicate a transition from stationary to non-stationary growth. The value of α for mounds should be unity, asymptotically. However, observed values are always less than unity. In our case, we have observed a value of 0.85. This value agrees with the reported values observed in the case of inorganic mounds formation.[27, 31]

The variations of roughness amplitude (w) and in-plane length scale (ξ) as function of coverage (θ) were studied to understand the details dynamics of the growth. The interface width and lateral correlation length is calculated using the previously described method from $G^{1/2}(r)$ for different samples and plot as a function of coverage shown in Fig. 3.10 (a, b).

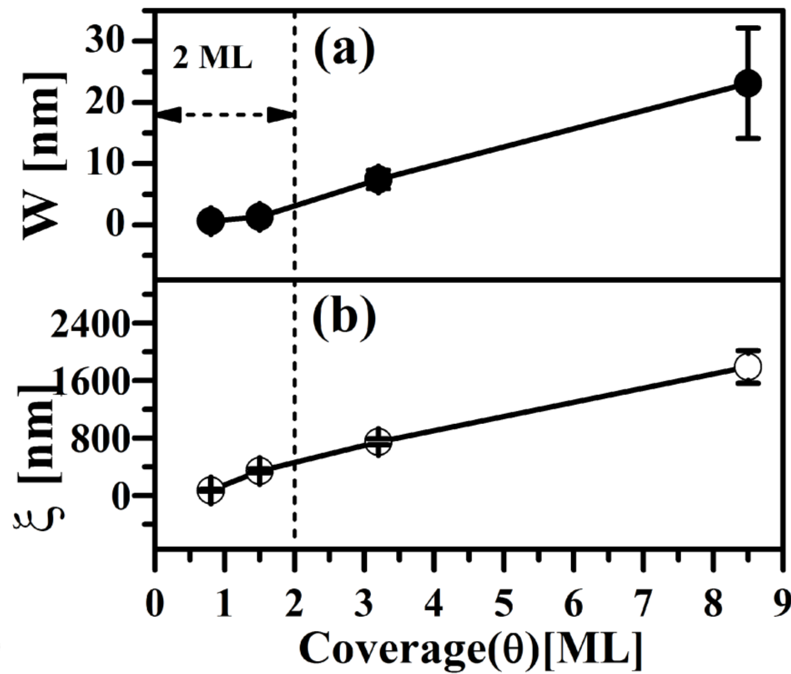

Fig. 3.10: Log-log variation of (a) interface width and (b) lateral correlation function (ξ) with coverage. As there are two different type of growth they are separated by dash line.

However, they do not show any power law behavior within the coverage range that we explore in this work. This could be because of the two different growth kinetics observed within the explored range of the coverage. Therefore, it is difficult to correlate this growth mechanism with the reported growth mechanism based on the dynamic scaling theory without the values of growth and dynamic exponent. The observed two α's signifies a transition in growth kinetics. This could be due to instability in the films due to coalesce of mounds. The variation of W with ξ, interestingly, shows linear behavior in the regime of mound growth as shown in Fig. 3.11. The slope of linear variation is 0.02, which essentially revealed the higher lateral growth rate than the vertical growth of the mounds.

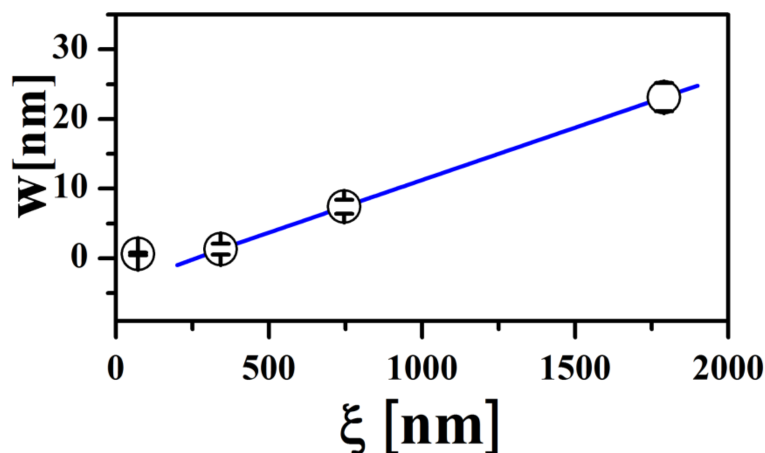

Fig. 3.11: Variation of interface width (w) with lateral correlation function (ξ). By fitting the points we get slope of this curve 0.02.

3.4 Conclusions

Detail understanding of the growth of TC-PTCDI-C_8 has been possible combining AFM and XRR results. We have observed a structural transition consisting in a strong variation of local surface slope from layer to the 3D mound formation. Thickness of the layer is calculated from XRR measurement. This layer consists of two molecular layers with layer spacing 18.3 Å, which is close to the layer spacing for the thick multilayer mounds (18.8Å). The error bar for calculating thickness from XRR is typically less than 1 Å. Growth transition from layer-by-layer to mounds formation is reflected in a transition from stationary to non-stationary growth confirmed by the variation of local surface slope and roughness exponents. The thickness calculated from XRR of the incomplete first layer observed in 0.75 ML sample is much less than the thickness of the complete layer observed in the 1.5 ML sample. This is essentially due to the fact that in case of incomplete layer an average height was assumed in XRR fitting where height fluctuations were considered as roughness. Therefore, thickness observed from the XRR fitting is not the actual thickness of the terraces that started forming but the roughness of the surface. Morphological changes

TH-1132_08612114

during the first stages of the growth implying molecular re-orientation which has recently been observed for other molecules on SiO_2 as well, for instance, for F_{16}CuPc, quaterrylene and parasexiphenyl. This is probably more common scenario to what is generally assumed and most likely due to the maximization energy per unit area in the organic-substrate interface. The formation of flat top mounds, as observed here, has been explained in terms of layer dependent Ehrlich-Schwöbel barrier that restrict the downward molecular diffusion current at the step edge and form a stack of 2D layers. In such cases, the instability is due to coalesce of mounds.

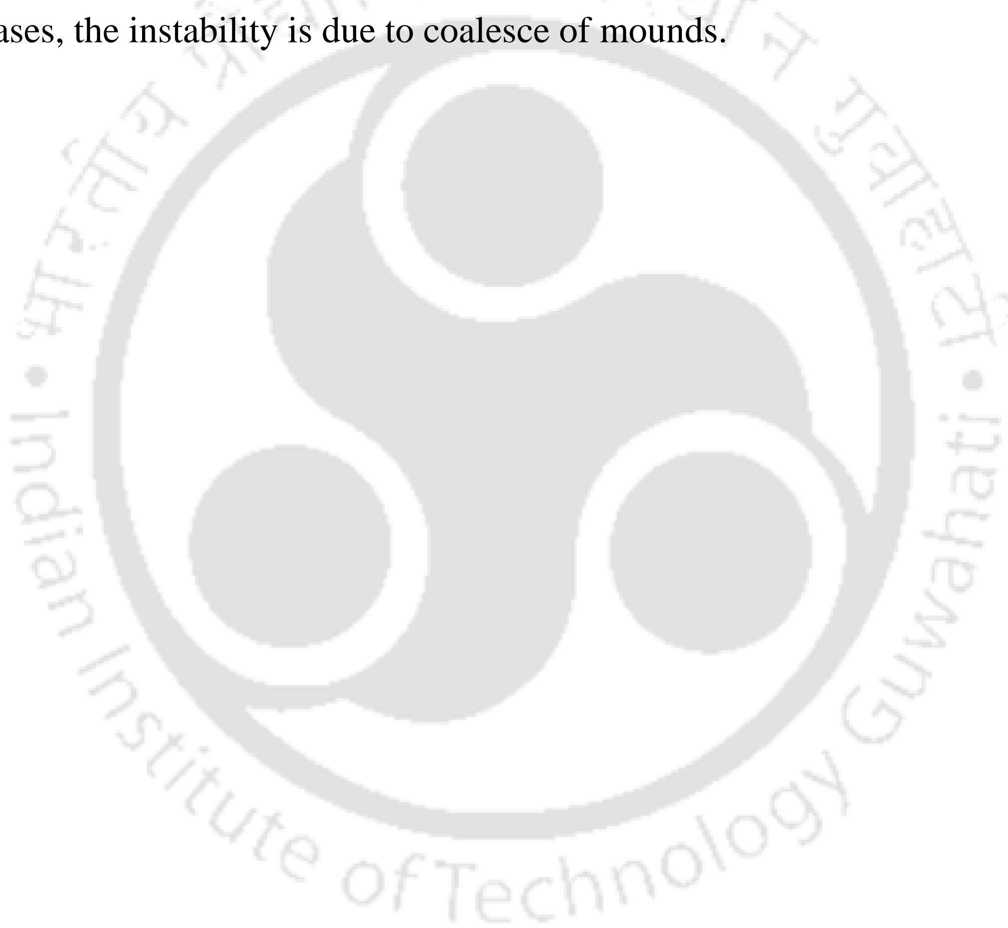

TH-1132_08612114

3.5 References

1. X. N. Zhang, E. Barrena, D. G. d. Oteyza, and H. Dosch, Surf. Sci. **601**, 2420 (2007).
2. S. C. B. Mannsfeld, K. Leo, and T. Fritz, Phys Rev Lett **94**, 056104 (2005).
3. B. Krause, A. C. Durr, F. Schreiber, H. Dosch, and O. H. Seeck, Surf. Sci. **572**, 385 (2004).
4. D. Y. Zhong, M. Hirtz, W. C. Wang, R. F. Dou, L. F. Chi, and H. Fuchs, Phys. Rev. B **77**, 113404 (2008).
5. K. Vasseur, C. d. Rolin, S. Vandezande, K. Temst, L. Froyen, and P. Heremans, J Phys Chem C **114**, 2730 (2010).
6. Y. Chen, L. Chen, G. Qi, H. Wu, Y. Zhang, L. Xue, P. Zhu, P. Ma, and X. Li, Langmuir **26**, 12473 (2010).
7. A. C. Durr, F. Schreiber, K. A. Ritley, V. Kruppa, J. Krug, H. Dosch, and B. Struth, Phys Rev Lett **90**, 016104/1 (2003).
8. Y.-P. Zhao, J. B. Fortin, G. Bonvallet, G. C. Wang, and T. M. Lu, Phys Rev Lett **85**, 3229 (2000).
9. J. Krug, Adv. Phys. **46**, 139 (1997).
10. J. Krim and G. Palasantzas, Int. J. Mod. Phys B **9**, 599 (1995).
11. F. Biscarini, P. Samor, O. Greco, and R. Zamboni, Phys Rev Lett **78**, 2389 (1997).
12. Z. Xun, G. Tang, K. Han, H. Xia, D. Hao, Y. Chen, and R. Wen, Physica A **389**, 5635 (2010).
13. P. K. Dhillon, S. Sarkara, A. Franquet, A. Moussa, and W. Vandervorst, Appl. Surf. Sci **258**, 9579 (2012).
14. S. Yim, K.-i. Kim, and T. S. Jones, J Phys Chem C **111**, 10993 (2007).

TH-1132_08612114

15. D. Hong, Y. R. Do, H. T. Kwak, and S. Yim, J. App. Phys. **109**, 063507 (2011).
16. A. Brillante, I. Bilotti, R. G. D. Valle, and E. Venuti, Phys. Rev. B **85**, 195308 (2012).
17. J. J. Yang, J. Tang, N. Liu, F. Ma, W. Tang, and K. W. Xu, J. App. Phys. **111**, 104303 (2012).
18. X. N. Zhang, E. Barrena, D. K. Goswami, D. G. de Oteyza, C. Weis, and H. Dosch, Phys Rev Lett **103**, 136101 (2009).
19. Y. Wakayama, R. Hayakawa, X. N. Zhang, H. Dosch, N. Hiroshiba, and T. Chikyow, J Phys Chem C **113**, 2197 (2009).
20. T. N. Krauss, E. Barrena, D. G. d. Oteyza, X. N. Zhang, J. n. Major, V. Dehm, F. Wu¨rthner, and H. Dosch, J Phys Chem C **113**, 4502 (2009).
21. T. N. Krauss, E. Barrena, X. N. Zhang, D. G. d. Oteyza, J. n. Major, V. Dehm, F. Wu¨rthner, L. P. Cavalcanti, and H. Dosch, Langmuir **24**, 12742 (2008).
22. A. K. Das, S. K. Ghose, B. N. Dev, G. Kuri, and T. R. Yang, Appl. Surf. Sci **165**, 260 (2000).
23. D. K. G. d. Boer, Phys. Rev. B **44**, 498 (1991).
24. M. Pelliccione and T.-M. Lu, *Evolution of thin film morphology: modeling and simulation,* (Springer-Verlag, New York, 2008).
25. Y. Zhao, G.-C. Wang, and T.-M. Lu, *Characteriztion of Amorphus and Crystalline Rough Surface: Principles and Application* (Academic Press, London, 2001).
26. J. Lapujoulade, Surf. Sci. Rep. **20**, 191 (1994).
27. J. H. Jeffries, J.-K. Zuo, and M. M. Craig, Phys Rev Lett **76**, 4931 (1996).
28. I. J. Lee, M. Yun, S.-M. Lee, and J.-Y. Kim, Phys. Rev. B **78**, 115427 (2008).
29. D. P. Datta and T. K. Chini, Phys. Rev. B **69**, 235313 (2004).

30. T. K. Chini, D. P. Datta, and S. R. Bhattacharyya, J. Phys.: Condens. Matter **21**, 224004 (2009).
31. G. Lengel, R. J. Phaneuf, E. D. Williams, S. D. Sarma, W. Beard, and F. G. Johnson, Phys. Rev. B **60**, 8469 (1999).

TH-1132_08612114

Growth of flat top Ag mounds on Si(111)-(7×7) reconstructed surfaces

4.1 Introduction

In order to understand the deep insight of flat-top mound formation, we have chosen to study the growth of Ag on Si(111)-(7×7) surfaces. This is a model example of flat top mound formation for inorganic materials whose growth mechanism does not follow any of the classic growth modes for mound formation that depends on the restricted diffusion driven by the diffusion activation energy and step edge barriers of the systems. On the other hand, TC-PTCDI-C_8 form flat-top mounds on SiO_2 substrates as described in the last chapter. However, this growth is driven by the diffusion of the molecules. These two systems with different growth mechanism form similar type of surface structures and therefore, we studied this system in order to find out any similarity in this structures formation. In this chapter, we discussed the growth of Ag mounds on Si(111)-(7×7) surfaces and was correlating with the results obtained in case of TC-PTCDI-C_8 mounds growth.

Study of growth of Ag films on Si surfaces has been of great interest for the decades in view of their technological applications.[1] As a result, the Ag/Si(111) system is one of the most extensively studied because

TH-1132_08612114

it is a non-reactive metal-semiconductor system.[1-3] The growth morphology of Ag film depends upon the deposition rate and growth temperature.[4-6] On the other hand, the studies of low dimensional structures have attracted considerable interest because spatial confinement of electrons in thin films results in discrete quantum well states (QWS's).[7, 8] In the semiconductor layer systems, these effects are well known and have already been used in electronic devices. However, the observation of quantization effects in metal layers has been restricted to only a few systems. In this respect Ag films have attracted a great interest due to nearly free electron characteristics of s-p bands over a large region of Brillouin Zone (BZ). The room temperature growth of Ag films and the low temperature growth followed by room temperature annealing produce 3D flat top mounds with strongly preferred height of two atomic layers on a wetting layer.[7, 9] With further growth, these mounds increase the number density with no change in height of the mounds and at the same time grow laterally. Eventually they coalesce to form percolated mound structures. Nevertheless, the percolated structures also follow the even atomic layer preference such as 2, 4, 6 … etc.[9] This growth mechanism definitely does not belong to the growth modes normally observed and termed a “electronic growth” of metal over layer on semiconducting substrates.[10] Essentially, Ag free electrons are confined within the two interfaces of the films. As a result of this confinement, the electrons produce quantum well states by forming electron standing wave within the interfaces and stabilize the thickness of the films by constructive interference.[7, 8, 11] As an example, a critical thickness of the films Is proposed beyond which atomically flat films can be grown on GaAs(111) surfaces.[11] However, no thickness windows for the growth of Ag on Si(111)-(7×7) surfaces is observed for this system.[12-14] In this chapter, we discuss the detailed statistical analysis of the surface morphology of Ag films and its evolution with coverages to understand the growth mechanism and correlate

TH-1132_08612114

the lateral and vertical growth of the mounds with the results we obtained in case of TC-PTCDI-C_8 mound growth. Though the Ag films form percolated network like flat-top mounds, whereas, TC-PTCDI-C_8 form individual mounds without any percolation, line profile at any instant of growth for both the system reveals similar type of mounds. In our analysis of rough surfaces, we have analyzed essentially the line profiles at three dimensions on the surface. In the process of analysis, we have predicted different scaling exponents of the electronic growth. A linear diffusion process has been identified which works in parallel with the electronic growth. We have explored a wide range of coverage of Ag of 1 ML to 80 ML.

4.2 Experimental

4.2.1 Clean surfaces of silicon

It is extremely important to prepare an atomically clean surface of the silicon substrate on which an epilayer is to be grown. Common impurities like O and C on the surface should be brought down below the detection limit. This is usually checked by Auger electron spectroscopy (AES). However, we have used reflection high energy electron diffraction (RHEED) to detect characteristic diffraction patterns of clean surfaces followed by in-situ STM measurements and ensure that the substrate surface is clean before the deposition begins. The sample is degassed at 600°C for about 12 hours in the MBE chamber. Following this it is flashed at ~1200°C for about 2-3 minutes by direct heating. In this process the native oxide on the Si surface desorbs and a clean silicon surface is produced. During this heating, the pressure in the chamber should not increase above 1×10^{-9} mbar. Clean silicon surfaces are reconstructed. Surface reconstruction is the rearrangement of the surface atoms due to the termination of the bulk structure at the solid-vacuum interface.

TH-1132_08612114

4.2.2 Si(111) surface reconstruction

During the preparation of atomically clean surface in ultra high vacuum condition, the oxide layer on top of the Si substrate was removed. Due to the absence of neighbouring atom on one side, the force acting on the surface of Si atom is modified. As a result due to minimum energy configuration surface is changed with respect to bulk structure. Here in the Fig. 4.1 we show the Si(111)-(7×7) reconstructed surface according to dimer-adatom-stacking-fault (DAS) model. This model was proposed by Takayanagi et al. in 1985.[15] (7×7) is the more stable configuration among all (2n+1) × (2n+1) where n=1,2,3… reconstructions are observed in Si(111) surface.

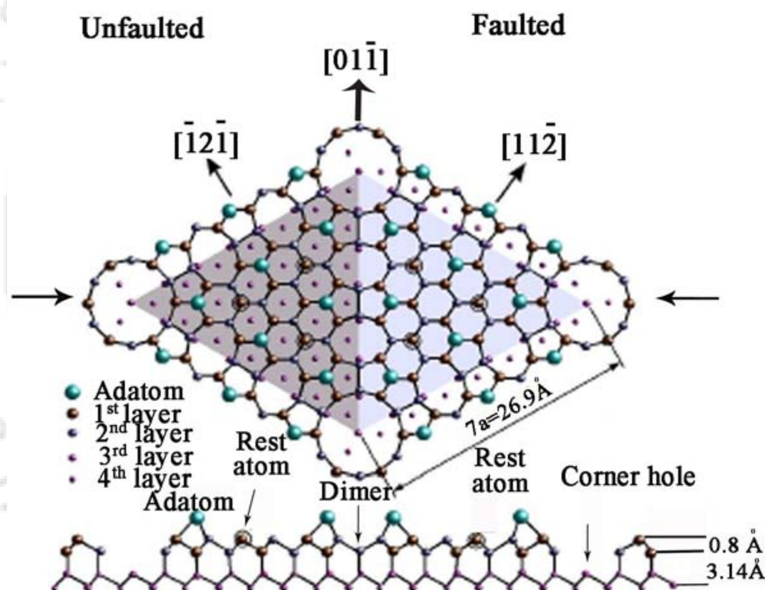

Fig. 4.1: Schematic diagram of Si(111)-(7×7) reconstructed surface according to DAS model

In this figure we show the top view of the reconstructed surface unit cell where different layer atoms are defined by different sizes and different color ball. In the lower part we show the side view of the surface. This model consists of 12 adatoms on the top surface which are divided by two triangular shape sub unit cell. One of which is called faulted and another is called un-faulted half within which one has stacking fault. There are nine

dimers per unit cell and one deep corner hole. Each adatom saturates three dangling bond of underlying atom. In the above picture the adatoms in the half unit cell with stacking fault are shown brighter than the adatoms in the other half without stacking fault.[16] In Fig. 4.2 two STM images of reconstructed surface are shown in positive and negative bias voltage. In positive bias electron tunnel into the unoccupied states of the sample and in this case both of the half are similar. We can distinguish two parts of the unit cell in negative bias condition when electron tunnel from the filled state of the sample into the tip. In the Fig. 4.2 (a) STM image is in positive sample bias condition and (b) in negative bias condition. In the second case we can see clearly the two half unit cell which are marked in the image.

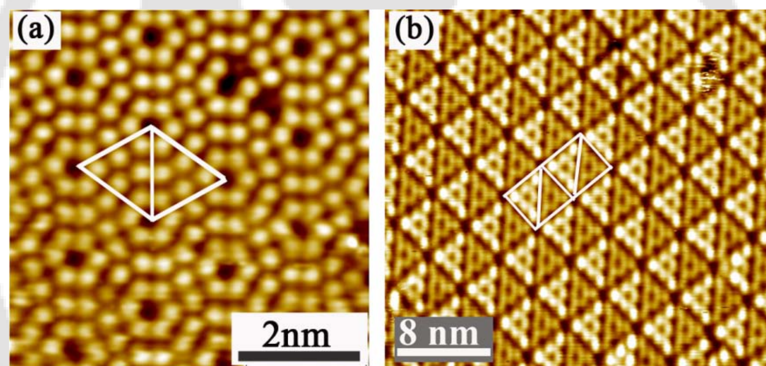

Fig. 4.2: STM image of Si(111)(7×7) reconstructed surface obtained at different bias voltage.(a) Sample bias: 1.7 Volt, Tunneling current: 0.5nA, (b) Sample bias -1.9 volt; tunneling current 0.2nA. One unit cell is marked in (a) and two unit cell are marked in (b). Two parts of the unit cell are different, one is called Faulted half and another half is un-faulted half which is very clear in the –ve bias image.

4.2.3 Growth of Ag on Si

In spite of large lattice mismatch (25%) Ag can grow epitaxially on silicon substrate.[17-19] This is possible by coincident site lattice matching. Because there is 0.42% lattice mismatch between $3a_{Si}$ and $4a_{Ag}$ (a_{Si}=5.43Å, a_{Ag}=4.09Å).[17, 20, 21] Coincident site lattice matching alone does not give rise to epitaxial growth. A favorable bonding configuration of substrates and

TH-1132_08612114

over-layer atoms are required which exist in case Ag on Si(111)-(7×7) surfaces.

The Ag growth and scanning tunneling microscopy (STM) measurements were performed in a custom made molecular beam epitaxy (MBE) chamber coupled with an ultra high vacuum (UHV) variable temperature scanning tunneling microscopy (VTSTM, Omicron). The base pressure in the growth chamber was 1×10^{-10} mbar. A n-type Si(111) wafer (orientation ± 0.5^{o}) with resistivity of 10-20 Ω cm was used as a substrate material. Atomically clean reconstructed Si(111)-(7×7) surface were prepared by the method described earlier. Ag atom were then evaporated from Knudsen cell made of pyrolytic boron nitride (PBN) and deposited on Si(111)-(7×7) reconstructed surface at RT at deposition rate 2 monolayer/min. We have deposited 1, 1.4, 1.6, 1.8, 2, 4, 5,10, 30, 40, 80 ML Ag on Si(111)-(7×7) reconstructed surface. Here we define 1 monolayer (ML) of Ag is equivalent to the nominal surface atomic density of Ag(111), 1.5×10^{15} atoms/cm^2. The chamber pressure increases to 5×10^{-10} mbar at the time of deposition. Following deposition the samples were transferred to VTSTM chamber for morphology characterization.

4.3 Results and Discussions

4.3.1 Morphological Analysis

In order to understand the morphology evolution of Ag on Si(111)-(7×7) surfaces, we have used scanning tunneling microscopy (STM). The basic operation procedure of STM is discussed in the chapter II. Here in the Fig. 4.3 we have shown the STM images of Ag films for different Ag coverages.

TH-1132_08612114

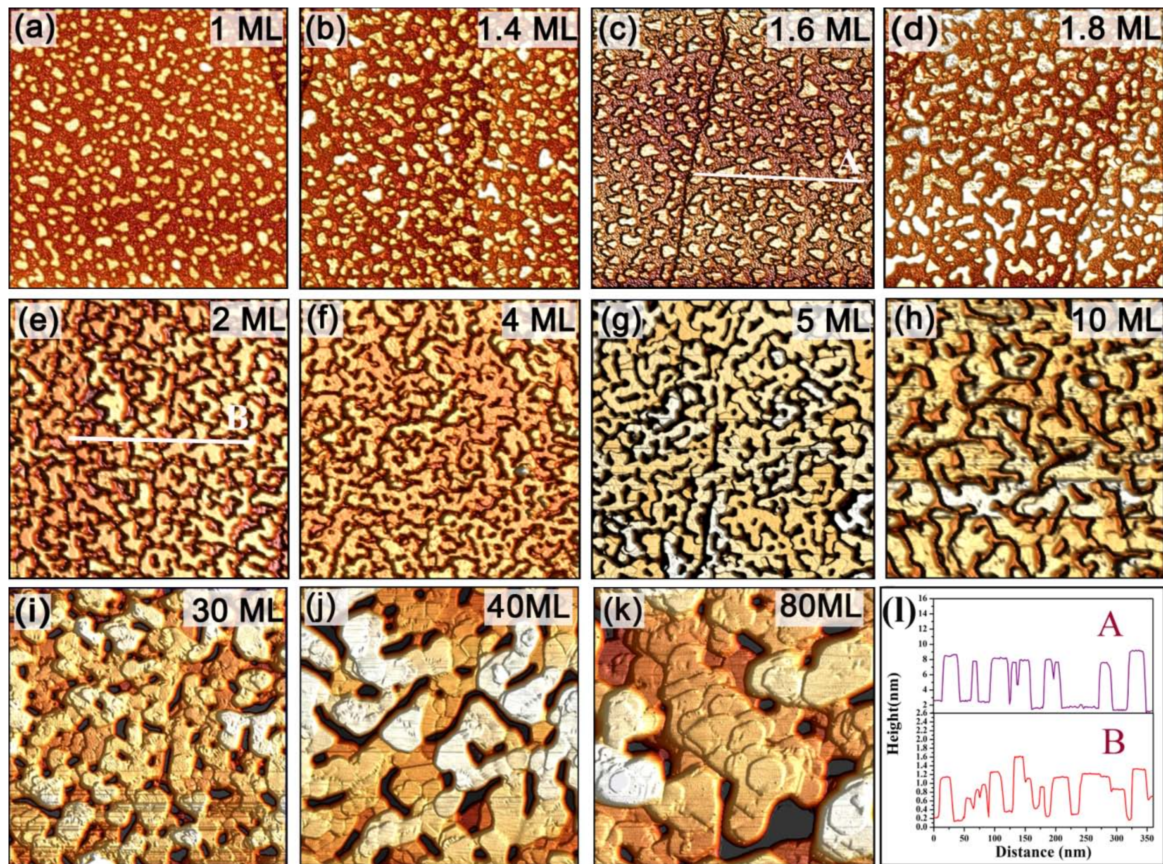

Fig. 4.3: STM images of (a-k) Ag/Si(111)-(7x7) surfaces, showing the surface morphology for 1, 1.4, 1.6, 1.8, 2, 4, 5, 10, 30, 40, 80 ML coverage of Ag. All the images are in 500×500 nm^2 area. (l) shows a typical line profile taken from the line drawn in (c and e) showing flat top mound formation.

Plateau like Ag mound formation on the top of wetting layer is observed for the samples with Ag coverage of 1ML to 1.8 ML (Fig (a-d)). These mounds are growing laterally with coverage keeping height of the structures constant. We have grown samples with several other coverages (2-80ML) which are shown in Fig. 4.3(e-k). It is observed that small islands increase their number density and lateral extension with coverage with no change in height, eventually forming a percolated network of same preferred height. After that these islands grow laterally as well as vertically in both directions. This type of growth is called percolated network type growth. A strong preferred height of two atomic layer is observed for the sample up to 1.8ML (below percolation). For thicker samples, percolated structures showed a

tendency to grow with preference of N-layer height where N is even number (N=2, 4, 6… etc).This preferential height growth mode is called "electronic growth" mode where electronic confinement within the metal semiconductor interface and vacuum interface played an important role by producing electron standing waves. Due to the formation of standing wave with constructive interference, it stabilizes the film thickness.[7, 9] The formation of percolated network type mounds are observed for the samples with coverages 2-30 ML which are shown in Fig.4.3 (e-i). The strong height preference with even atomic layer is observed in this range of coverages. However, monatomic layered hexagonally shaped islands formation is observed on top of the percolated mounds are observed for the samples with coverage beyond 30 ML. As a result, preferential height growth was no longer observed after wards. The typical STM images in this range are shown in Fig. 4.3(j-k). From the STM images presented in the Fig. 4.3(a-i), it is observed the formation of the flat-top mounds. Two typical line scans showing height profiles are shown in Fig. 4.3(l) taken along the lines drawn in Fig.4.3 (c) and (e). They clearly represent the formation of flat-top mounds which is comparable with the line scan taken from the sample TC-PTCDI-C_8 presented in the Chapter - III.

4.3.2 Statistical analysis of surface morphology

In order to understand the dynamic behavior of the growth of Ag on Si(111)-(7×7) surfaces, we have analyzed the surface fluctuation and determined different scaling exponents which represent the characteristics of the surface morphologies. The technical detail of the analysis method is described in the Chapter II. These quantities are determined from height-height correlation function, $G(r,\theta)$ which is defined as mean square of height difference between two surface positions separated by a distance r for coverage of the atom (θ) as $G(r,\theta)=\langle[h(r,\theta)-h(0,\theta)]^2\rangle$ where $h(r,\theta)$ and

$h(0,\theta)$ are the heights of the surface at the locations separated by a distance r and the brackets signify an average over pairs of points.[22-25] As the growth rate of Ag is kept constant throughout the experiments, we have considered the dynamic behavior of the growth in terms of θ instead of time t. For the small r, height-height correlation function $G(r,\theta)=[m(\theta)r]^{2\alpha}$ with $r<<\xi(\theta)$ where $\xi(\theta)$ is the characteristic in-plane length scale, α is the roughness scaling exponent and $m(\theta)$ is the local slope of the surface profile for small length scale.[23, 26] $m(\theta)$ is calculated from the fitting of linear portion of log-log plot of $G(r,\theta)$ vs r using above equation. The separation between the mounds is another essential parameter to characterize the mounded surfaces. This is called wavelength (λ). Lateral correlation length, $\xi(\theta)$, is the measure of the length beyond which surface heights are not significantly correlated. For the mounded surfaces, this is essentially the size of the mounds.[27] The wavelength λ and lateral correlation length ξ are not necessarily equal. They only must satisfy the relation $\xi \le \lambda$ because mounds are separated by at least their size. Only if the mounds grow next to each other would imply that $\xi = \lambda$.[28]

Here we calculate $G(r,\theta)$ from STM images of different coverage. In order to avoid sampling induced effect in $G(r,\theta)$, care has been taken to include many AFM images in the averaging $G(r,\theta)$. In our case we check 8-10 images for a particular coverage, which is good for statistical reliable data. Here we plot $G^{1/2}(r)$ Vs r which is shown in Fig. 4.4. Looking at the morphologies of the STM images shown in Fig.4.3, we can divide the growth into three different regions: (a) individual mound growth with two atomic layer height (1-1.8 ML coverages), (b) percolated mound growth (2 – 30 ML) and (c) percolated mounds with hexagonal island at top (40-80 ML). To monitor the evolution of surfaces with coverages, we calculated interfaces width (w). To monitor the roughening process qualitatively, we

measure the interface width (w) as a function of coverage(θ). Following the method described in ref[29, 30] , we define the surface roughness amplitude $w(\theta)$ [shown by the arrow mark in Fig. 4.4(b)] as the value of $G^{1/2}(r,\theta)$ at first local maxima, $w(\theta)=G^{1/2}(\xi/2)$ where ξ marked by an upward arrow is the position of r at the first local minima of $G^{1/2}(r)$. This definition of roughness amplitude is preferred over the large r limit of $G(r)$ because artifacts at larger length scale can affect STM data. The roughness exponent is calculated by fitting the linear portion of the log-log plot of $G^{1/2}(r)$ Vs r. We have observed three value of roughness exponent (α). Below percolation α is 0.67 ± 0.04, in the percolated region it is 0.77 ± 0.07 and in hexagonal island region is 0.83 ± 0.03 as shown in Fig. 4.4 (a, b, c).

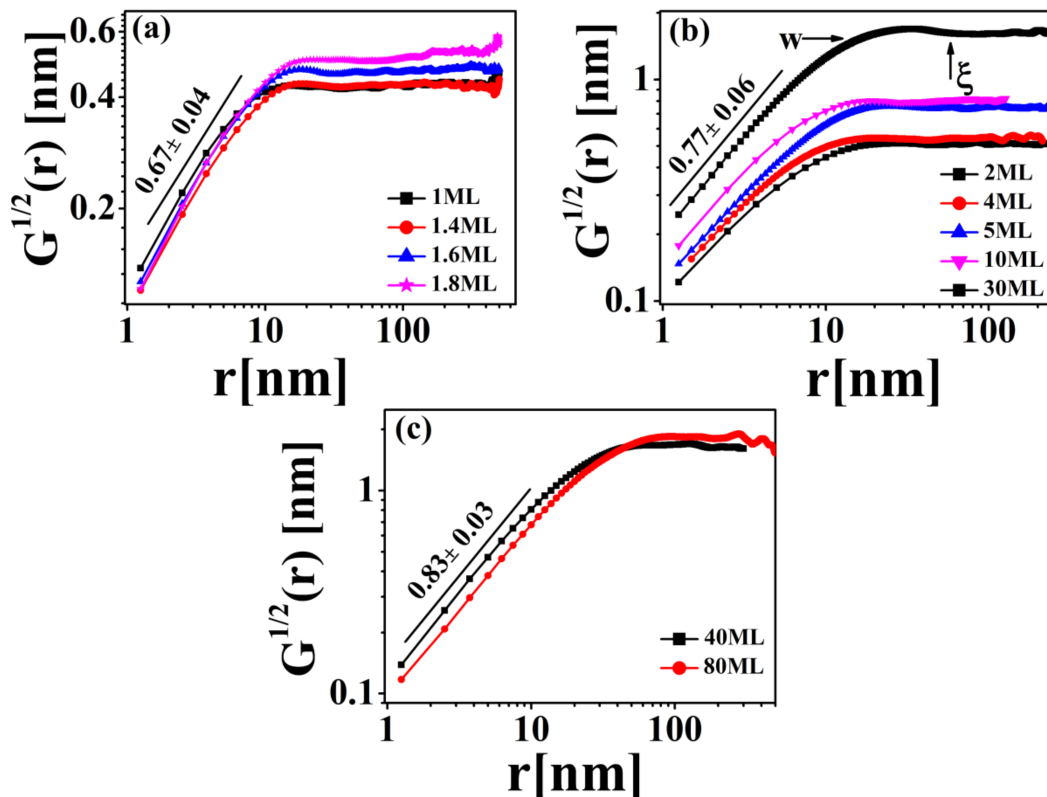

Fig. 4.4: Square root of height-height correlation function calculated from STM images of (a) 1 to 1.8 ML Ag coverages, (b) 2 to 30 ML Ag coverages, (c) 40 and 80 ML Ag coverages. Roughness exponent (α) is calculated from the power fitting of the linear portion.

The interface width (w) increases as power law of θ, as $w(\theta)\sim\theta^{\beta}$. As the rate of flux of the deposition is kept constant along the growth, we used $w(\theta)\sim\theta^{\beta}$ instead of $w(t)\sim t^{\beta}$, where t is the time. The exponent β characterizes the dynamics of the growth and it is called growth exponents. On the other hand lateral correlation length $\xi(\theta)$, increases with θ as a power law as $\xi(\theta)\sim\theta^{1/z}$, where $1/z$ is called the dynamic exponent. The log-log variation of w calculated from square root of height-height correlation function is shown in Fig. 4.5(a). The value of growth exponent calculated from the slope is 0.33 ± 0.03. The dynamic exponent ($1/z$) was calculated from the slope of the log-log plot of lateral correlation length which is shown in Fig. 4.5(b). The value of $1/z$ is 0.27 ± 0.05.

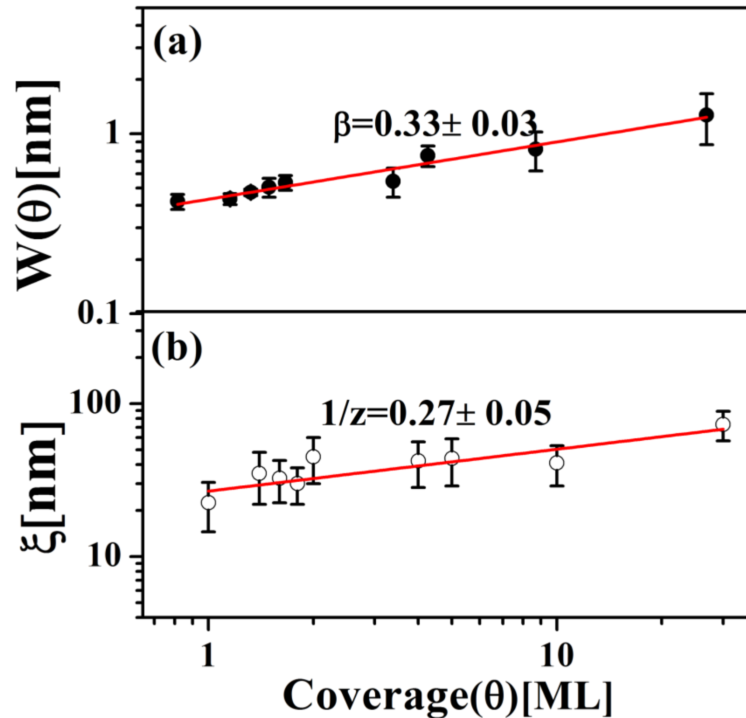

Fig. 4.5: Log-log variation of (a) interface width (w) and (b) lateral correlation length (ξ) with coverages (θ). Growth exponent (β) and dynamic exponent ($1/z$) are calculated from the slope of the a and b curve, respectively.

In order to find out the relation of growth rates along vertical and lateral direction of mounds we have plotted *w* Vs ξ which is shown in Fig. 4.6.

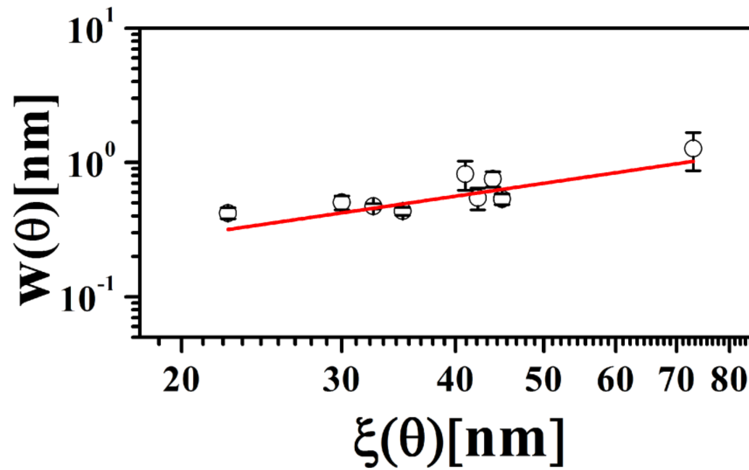

Fig. 4.6: Log-log variation of interface width (*w*) with lateral correlation length (ξ). Solid curve represents the least-square fit to the data points with power equation.

From the equations of *w* versus θ and ξ versus θ, as described above, one can derive that $w = C\xi^{\beta/(1/z)}$. From the fitting we have calculated the ratio of the exponent β /(1/z) = 0.99 ± 0.11 and *C*=0.014± 0.008 which is a constant. Here the value of exponent is ~ 1. This essentially means the linear relationship between *w* and ξ with slope ($dw/d\xi$) as 0.02. In our case, the ratio of β = 0.33 ± 0.03 and *1/z* = 0.27 ± 0.05, is 1.22 ± 0.10 which is comparable with the fitted value within the error bar. Therefore, one can consider almost the linear behavior with slope = 0.02. This slope indicates the competition between smoothing due to the lateral growth and roughening due to vertical growth. Smaller value of the slope indicates faster lateral growth than vertical growth, which essentially enables the wetting layer film growth. Therefore, one can expect to have smooth film growth with faster lateral growth. As predicted in the electronic growth mode, the formation of discrete quantum well states can lead to novel effects including preferred heights and critical thickness of metal films beyond which the film will be

atomically flat.[8, 9, 31-33] In case of Ag grown on Si(111)-(7×7) surfaces, we have not observed any such critical thickness. Faster lateral growth, as observed, can support the formation of smooth films. However, there is an instability in the growth that does not allow forming smooth films and a roughening in the growth mechanism is observed. A two-step growth mechanism has been popular in which films are grown at low temperature followed by room temperature annealing.[33, 34] At low temperature, a non-equilibrium structure is formed and this drives the system into a metastable state with height preference. However, it will not be accessible fully if unwanted kinetic processes are enabled. Though, room temperature growth of Ag films shows height preference as a consequence of "electronic growth" in which quantum well states can determine the film morphology but kinetic processes cannot be suppressed completely. As a result, we observed roughening in the growth in terms of flat top mounds at the lower coverages and percolated mounds at higher coverages with magic heights. This morphology is, essentially, due to the competition between quantum well state formation and kinetic growth processes.

From the theoretical treatments of non-equilibrium film growth, following the nonlinear growth equation the predicated scaling exponents are α=2/3 and β=1/5.[35] However for linear growth equation predicted value of the scaling exponents are α= 1 and β=1/4.[36] On the other hand in presence of Schwoebel barrier self affine scaling will break down because it prevents particle to diffuse downward.[37, 38] In such case also we can see the mound type surface with stationary slope. The predicted scaling exponents for Schwoebel barrier is α=1 and β=1/4.[37] None of these theoretical models support the exponents that we observed for electronic growth mode. In order to identify this roughening mechanism, we calculated local slope $m(\theta)$. If $m(\theta)$ is independent of the coverage [i.e., $m(t)$ is independent of time], then it

is said to be stationary. In such cases, height-height correlation function coincides for $r << \xi$. On the other hand, for non-stationary growth the local slope $m(\theta)$ increases with time and an up-shift of $G(r,\theta)$ is observed as film thickness increases.[23, 26] This represents mound growth. Fig. 4.7 shows the plot $m(\theta)$ versus coverage (θ). We have observed $m(\theta) = \sqrt{Kln(\theta/\theta_c)}$ dependency with anomalous scaling behavior up to the coverage of 30 ML. Here, K is constant and θ_c is transition coverage to the scaling regime.

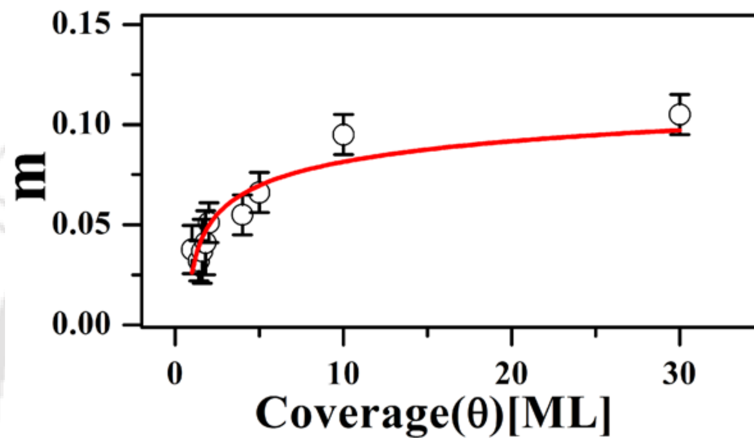

Fig. 4.7: Plot of local slope *m(θ)* as a function of coverage(*θ*). The solid curve is least square fit to the data points with $m(\theta) = \sqrt{Kln(\theta/\theta_c)}$

This dependency was observed for the preferential height growth region only. The value of θ_c obtained from the fit is 0.76 ML. This indicates that our smallest coverage sample (1ML) is already into the scaling regime. This dependency says that there is local surface diffusion, which causes the instability in the electronic growth and makes the growth non-stationary with increasing local surface slope with coverage.[23, 26, 39] In our case, all the samples were grown while substrates were kept at room temperature. Therefore, the growth kinetics at room temperature introduces instability in the electronic growth. This could be the reason for roughening of the films. However, only diffusion model simply cannot explain the growth exponents that we observed. Electronic growth mechanism is also very significant to describe the growth front morphology. Therefore, the roughening behavior

TH-1132_08612114

belongs to a different universality class involving quantum well states formation along with local surface diffusion.

4.4 Conclusions

In this chapter we have discussed the growth of flat-top Ag mounds on Si(111)-(7×7) surfaces as an example of flat-top mound growth with electronic growth mechanism. In the last chapter we have discussed the growth of TC-PTCDI-C_8 mounds where growth mechanism was essentially decided by the limited diffusion of the molecules by activation energy as well as by step edge barrier (ES barrier). In order to compare mound formation dictated by different growth mechanism, we have calculated and compared the growth rate of the mounds along the lateral and vertical directions. Interestingly, we have found the change of roughness width with lateral correlation length is same (0.02) for both the cases. This essentially indicates that the higher lateral growth rate than vertical growth. As a result, both the materials has high tendency to form smooth films. However, a roughening mechanism that can be suppressed completely in the kinetic growth region, make the film rough and therefore, formation of flat-top mounds are observed in both the cases.

In the process of analyzing Ag films, we have calculated the different scaling exponents for the electronic growth mode for the first time. The observed roughness scaling exponents for three different regions are 0.67 ± 0.04, 0.77 ± 0.06 and 0.83 ± 0.03. The values of growth and dynamic exponents are 0.33 ± 0.03 and 0.27 ± 0.05 respectively. Though, there are three different growth regions were assumed for the calculation of roughness exponents, however, we have observed single growth and dynamic exponents for the complete range of coverages. Average roughness

TH-1132_08612114

exponents observed for TC-PTCDI-C_8 mound growth are 0.68 ± 0.05 and 0.85 ± 0.02 which are comparable with the exponents obtained in case of Ag mounds. This would be very interesting to understand the similarity of mound formation for these two systems. This may require detail model calculations for flat top mound formations, which need to be explored and left it for future study. A simple model calculation for flat top mound formation is reported in ref[40]. However, they have not calculated the detailed growth parameters.

TH-1132_08612114

4.5 References

1. W. G. Schmidt, F. Bechstedt, and G. P. Srivastava, Surf Sci Rep **25**, 141 (1996).
2. S. Hasegawa, X. Tong, S. Takeda, N. Sato, and T. Nagao, Prog. Surf. Sci. **60**, 89±257 (1999).
3. E. J. Vanloenen, M. Iwami, R. M. Tromp, and J. F. Vanderveen, Surf. Sci. **137**, 1 (1984).
4. Z. H. Zhang, S. Hasegawa, and S. Ino, Phys. Rev. B **55**, 9983 (1997).
5. K. R. Roos and M. C. Tringides, Surf. Sci. **302**, 37 (1994).
6. G. Meyer and K. H. Rieder, Appl. Phys. Lett. **64**, 3560 (1994).
7. L. Gavioli, K. R. Kimberlin, M. C. Tringides, J. F. Wendelken, and Z. Zhang, Phys Rev Lett **82**, 129 (1999).
8. S. J. Tang, C. Y. Lee, C. C. Huang, T. R. Chang, C. M. Cheng, K. D. Tsuei, H. T. Jeng, V. Yeh, and T. C. Chiang, Phys Rev Lett **107**, 066802 (2011).
9. D. K. Goswami, K. Bhattacharjee, B. Satpati, S. Roy, P. V. Satyam, and B. N. Dev, Surf. Sci. **601** 603 (2007).
10. Z. Z. Q. Niu and C.-K. Shih, Phys Rev Lett **80**, 5381 (1998).
11. H. B. Yu, C. S. Jiang, P. Ebert, X. D. Wang, J. M. White, Q. Niu, Z. Y. Zhang, and C. K. Shih, Phys Rev Lett **88** (2002).
12. Z. Y. Zhang, Q. Niu, and C. K. Shih, Phys Rev Lett **80**, 5381 (1998).
13. Z. G. Suo and Z. Y. Zhang, Phys. Rev. B **58**, 5116 (1998).
14. A. L. Wachs, T. Miller, and P. R. T.-C. Chiang, B33 (1986) 8870, Phys. Rev. B **33**, 8870 (1986).
15. K. Takayanagi, Y. Tanishiro, M. Takahashi, and S. Takahashi, J. Vac. Sci. Technol. A **3**, 1502 (1985).
16. R. J. Hamers, R. M. Tromp, and J. E. Demuth, Phys Rev Lett **56**, 1972 (1986).

TH-1132_08612114

17. G. A. Smith, K. H. Park, G. C. Wang, T. M. Lu, and W. M. Gibson, Surf. Sci. **233**, 115 (1990).
18. D. C. McKenna, G. C. Wang, and K. Rajan, J. Elec.Matt. **20**, 753 (1991).
19. K. Takahiro, S. Nagata, and S. Yamaguchi, Appl. Phys. Lett. **69**, 2828 (1996).
20. T. C. Nason, L. You, G. R. Yang, and T. M. Lu, J. App. Phys. **72**, 466 (1992).
21. T. J. Konno and R. Sinclair, Phil. Mag **71**, 163 (1995).
22. J. Lapujoulade, Surf. Sci. Rep. **20**, 191 (1994).
23. M. Pelliccione and T.-M. Lu, *Evolution of thin film morphology: modeling and simulation,* (Springer-Verlag, New York, 2008).
24. Y. Zhao, G.-C. Wang, and T.-M. Lu, *Characteriztion of Amorphus and Crystalline Rough Surface: Principles and Application* (Academic Press, London, 2001).
25. A.-L. Barabási and H. E. Stanley, *Fractal Concepts in Surface Growth* (Cambridge University Press, Cambridge, 1995).
26. J. H. Jeffries, J.-K. Zuo, and M. M. Craig, Phys Rev Lett **76**, 4931 (1996).
27. M. Pelliccione, T. Karabacak, C. Gaire, G.-C. Wang, and T.-M. Lu, Phys. Rev. B. **74**, 125420 (2006).
28. J.-K. Zuo and J. F. Wendelken, Phys Rev Lett **78**, 2791 (1997).
29. I. J. Lee, M. Yun, S.-M. Lee, and J.-Y. Kim, Phys. Rev. B **78**, 115427 (2008).
30. D. P. Datta and T. K. Chini, Phys. Rev. B **69**, 235313 (2004).
31. H. Liu, Y. F. Zhang, D. Y. Wang, M. H. Pan, J. F. Jia, and Q. K. Xue, Surf. Sci. **571**, 5 (2004).
32. L. Huang, S. J. Chey, and J. H. Weaver, Surface Science **416**, L1101 (1998).

TH-1132_08612114

33. A. R. Smith, K. J. Chao, Q. Niu, and C. K. Shih, Science **273**, 226 (1996).
34. G. Neuhold, L. Bartels, J. J. Paggel, and K. Horn, Surf. Sci. **376**, 1 (1997).
35. Z. Lai and S. Das Sarma, Phys Rev Lett **66**, 2348 (1991).
36. D. E. Wolf and J. Villain, Europhys Lett **13**, 389 (1990).
37. M. Siegert and M. Plischke, Phys Rev Lett **73**, 1517 (1994).
38. j. A. Stroscio, D. T. Pierce, M. Stiles, A. Zangwill, and L. M. Sander, Phys Rev Lett **75**, 4246 (1995).
39. H. Yang, G. Wang, and T. Lu, Physical review letters **73**, 2348 (1994).
40. D. Y. Zhong, M. Hirtz, W. C. Wang, R. F. Dou, L. F. Chi, and H. Fuchs, Phys. Rev. B **77**, 113404 (2008).

TH-1132_08612114

TH-1132_08612114

Chapter V

PTCDI-Ph on SiO_2 Surfaces: growth of long molecular terraces

5.1 Introduction

π-conjugate organic molecules play an important role in modern science due to their unique electrical and opto-electrical property. Moreover these molecules are the building block of low-cost, high performance organic devices[1-4] such as field effect transistor[5], solar-cells[6-9], light harvesting arrays[10, 11] and light emitting diodes[12-14]. Out of all π-conjugated organic semiconductors, Perylene tetracarboxylic diimides (PTCDI) and their derivatives have attracted more attention in the recent years for their extraordinary thermal and photochemical stabilities[15, 16] It also has been used as optical switch[17], photoreceptors, chemical sensors,[18] etc. Due to weak π–π interaction between molecules, the packing of molecules within the active channel of the devices has been very important in order to enhance the charge carrier mobility. Therefore the precise control on the morphology and other properties are the main challenging issues in the film growth and the

TH-1132_08612114

self-assembled growth of these molecules are widely being used to control the growth.[19, 20]

Perylene and its derivatives, are found to be good n-type organic semiconductor for optoelectronic device applications [20]. One can also tune their HOMO-LUMO gap by attaching different functional groups with the core.[21] On the other hand, diffusion of the molecules play very important role in self-assembly. Substrate temperature dictates the diffusion. As a result, substrate temperature has been a key parameter in self-assembled growth.

In this chapter, we have discussed the self-assembled growth of perylene-diimide derivative, N, N´-di-phenyl perylene tetracarboxylic diimide (PTCDI-Ph) long terraces on SiO_2 substrate. The growth kinetics of the terraces are also discussed. Structural, electrical and optical properties of the films grown at different substrate temperatures are studied.

5.2 Experimental

PTCDI-Ph molecules were synthesized and cleaned before using them for deposition. The chemical structure and the dimension of the molecule are shown in the Fig. 1.9. PTCDI-Ph films were grown using thermal evaporation technique under high vacuum condition (10^{-6} mbar). The basic operation and the description of the instrument used for growth is discussed in chapter II in the section 2.1.2. PTCDI-Ph molecules were grown on SiO_2 surface with different substrate temperature such as RT, 80°C, 90°C, 120°C. The substrates were cleaned using methanol, acetone and di-ionized water following the standard procedure of cleaning semiconducting substrates which is already described in Chapter II section 2.1.1. Sublimation temperature for this molecule is 430°C. Molecular flux was kept constant

TH-1132_08612114

during deposition for all samples and deposition time was 10 min and the thickness of the film is about 500Å.

5.3 Results and Discussions

5.3.1 Studies of surface morphology

To study the morphology evolution of PTCDI-Ph films with substrate temperature, we have used ex-situ AFM measurements. Fig. 5.1(a) shows AFM micrographs for the sample grown at room temperature (RT). Small random grains formation is indicating very poor molecular alignment within the films. However, flat top long molecular terrace type structure formation is observed in case of samples grown at elevated substrate temperature. The AFM images shown in Fig. 5.1 (b-e) are showing the evolution of surface morphology of PTCDI-Ph films with substrate temperature. These structures

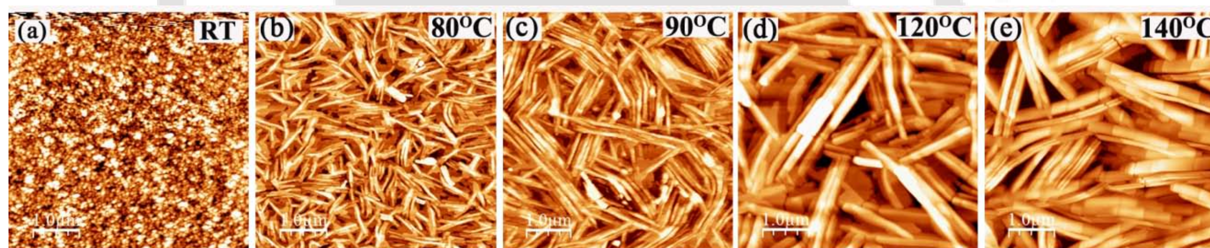

Fig. 5.1: AFM topography image of PTCDI-Ph film grown on SiO_2 substrate at (a) RT, (b) 80°C, (c) 90°C, (d) 120°C and (e) 140°C. Size of all the images are 5×5μm^2.

grow randomly onto the substrate. The size of these terraces increases with the substrate temperature. This can be easily seen from the AFM images. Fig. 5.2(a) is showing an AFM image of closer view of an individual terrace. Single molecular steps are clearly visible. A line scan along the terraces shown in Fig. 5.2(b) is showing the average molecular steps of about 17.4Å high. This is also confirmed from the histogram plot of a section of AFM image shown in Fig. 5.2(d). Other derivatives of PTCDI also found to form molecular steps.[1, 22] It is noticeable from Fig. 5.1 (b-e) that the molecular

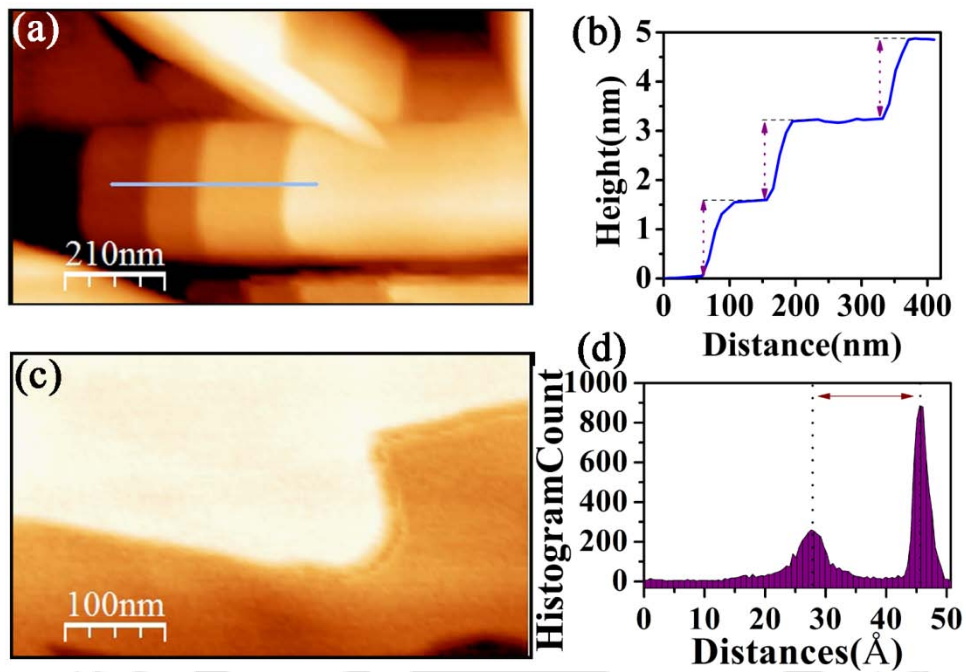

Fig. 5.2: (a) AFM image of the terrace (b) Line scan profile of the different layers of flat top ribbon. It is clear that each layer is grown by monomolecular layer.(c) AFM image of the underneath layer (d) Histogram profile of the underneath surface of the ribbon type terrace. It signifies the monomolecular step layer is in the underneath surface

terraces are growing along the length as well as along the width of the terraces as substrate temperature increases. As the coverages for all the samples were kept constant, therefore, it is likely that there is mass transport to grow the terraces. There could be two different components of the mass transport. First component could be due to the diffusion of the deposited molecules. As the number density of the terraces decreases with substrate temperature, it is obvious that small terraces contribute to grow larger terraces. This is only possible if small terraces break into parts and diffuse to attach to the larger terraces. Therefore, second components of diffusion can come from the diffusion of these terraces. The Arrhenius plot of variation of length and width with substrate temperature is shown in Fig. 5.3 (a) and (b) respectively. We have calculated the activation energy of the

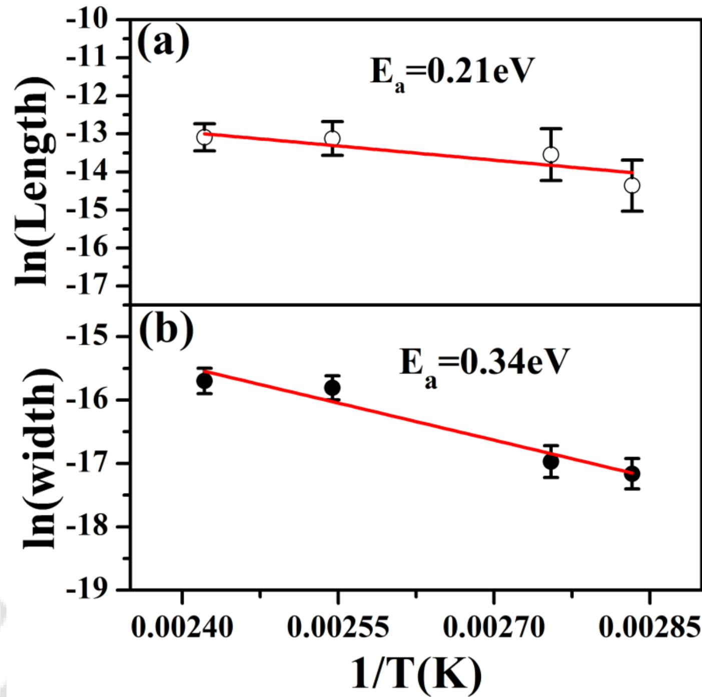

Fig. 5.3: (a) Schematic diagram of the formation of layers in PTCDI-Ph film, (b) Arrheneous plot of the nanostructure with respect to length and (c) with respect to width. The obtained value of the surface diffusion activation energy is along length is 0.21eV and along width is 0.34eV.

growth of these terraces from the linear fit of Arrhenius plot. The activation energy calculated for the growth of length (E_l) and width (E_d) of the terraces are found to be 0.21 eV and 0.34 eV, respectively. The calculated activation energy includes the contribution coming from the diffusion of the molecules on the films during the growth as well as the diffusion of the small terraces which break into parts and diffuse. Higher activation energy along the width represents the less favorable growth. For the measurement of length and width of the terraces, we have used ImageJ software.[23] We have considered only the clearly visible terraces without any overlap with other terraces. A large number such terraces were considered from several AFM images to confirm statistically significant data. The growth of such long terraces are observed earlier.[24] However, they have not studied details of the growth.

In order to study the vertical growth of the terraces with substrate temperature, we have calculated roughness width (w) form the sample grown in different substrate temperature. W's were calculated from the height-height correlation function (G(r,θ)). The details of the methodology for calculating G(r, θ) is given in the Chapter II in the section 2.4.1. A large number of (8-10 in this case) AFM images were considered in the calculation of G (r, θ) to have statistically reliable data. Fig. 5.4 shows the

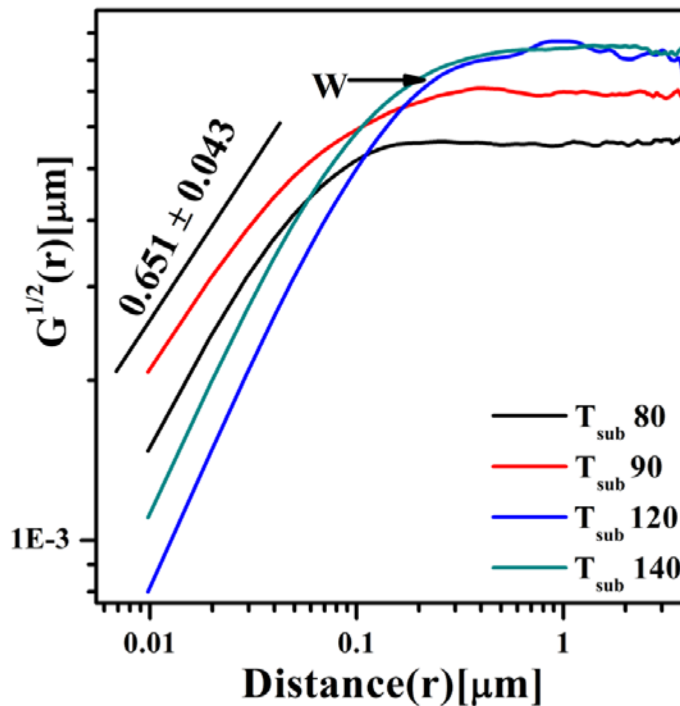

Fig. 5.4 : Square root of height-height correlation function plot of PTCDI-Ph film grown at different substrate temperature. The value of roughness exponents is calculated from the slope of the linear portion

plot of $G^{1/2}(r)$ vs r. The roughness exponent (α) is calculated from the slope of the linear portion of G(r). The average value of α is 0.65 ± 0.04. The variation of roughness width (w) with substrate temperature is shown in Fig. 5.5. Interestingly, we have found a power law behavior as $w \sim T^{\gamma}$. The value of the exponent is $\gamma = 0.64 \pm 0.11$.

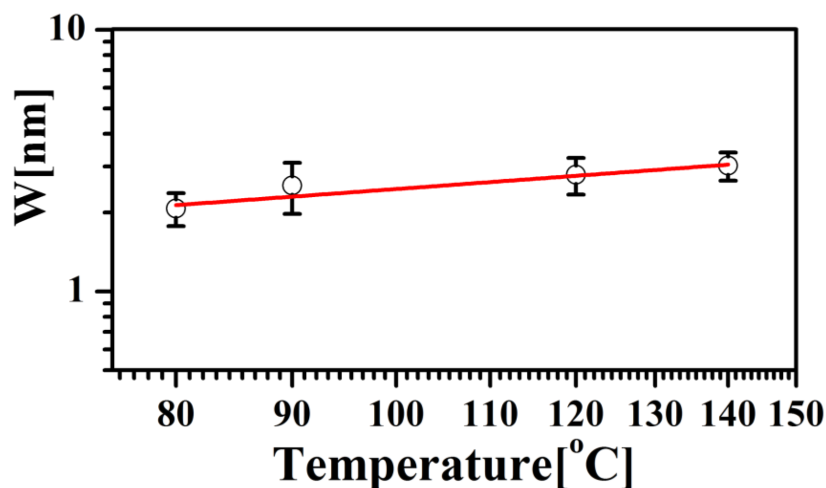

Fig. 5.5: Log-log plot of interface width as a function of growth temperature. It shows the power law behavior as $W \sim T^{0.64}$

5.3.2 Structural Characterizations

In order to gain insight into the film structures at different substrate temperatures and elucidate the molecular arrangement within the film, we have carried out x-ray reflectivity (XRR) measurements. We have used Cu-Kα X-ray radiation with wavelength 1.54Å. Fig. 5.6 shows representative XRR data taken from the three samples grown at 80°C, 90°C and 120°C substrate temperature. We have observed up to third order Bragg peaks, indicating layered structure with the well order vertical arrangement of the molecules within the films. However, XRR taken form sample grown at RT does not show any Bragg peaks (data not shown). This essentially means no vertical arrangement of the molecules within the films. From the position of the Bragg peaks, we have calculated the average lattice spacing d ~ 17.3Å. This result confirms the layer spacing calculated from the AFM results in the previous section.

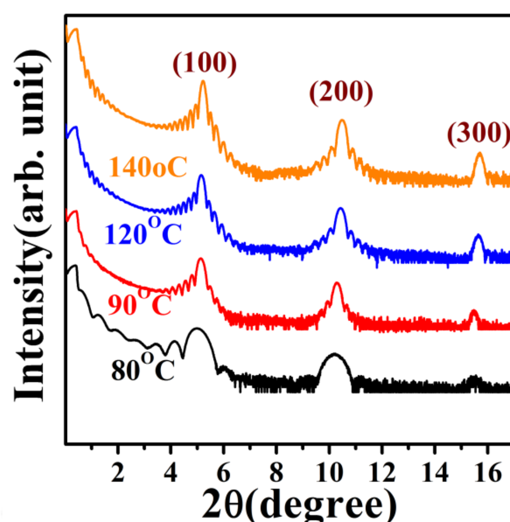

Fig. 5.6: X-Ray reflectivity spectra of PTCDI-Ph film grown on SiO_2 surface corresponding to substrate temperature 80°C, 90°C, 120°C and 140°C. The Bragg peak position is shifting in right direction with increment of substrate temperature.

Combining the XRR results with AFM results, a possible growth models is proposed. To achieve the layer spacing of 17.3Å with the molecule of 19.9Å length, it is possible that the molecules are tilted with respect to the vertical direction of the substrate. The calculated angle is about 30°. Here we consider that Ph group connected with the PTCDI core does not change the physical structure of the molecules while forming films by maintaining the actual angle of the group with the core. Along the length of the terraces, molecular cores are stacked by π-π interaction. However, molecules are connected side-wise along the width of the terraces which is essentially weaker. As a result, molecular interaction along the length of the terraces is stronger than that of along the width. Therefore, long terraces are formed. Higher substrate temperature increases the diffusion of the molecules and possibly the diffusion of small terraces, which coalesce with the bigger terraces. In Fig. 5.7(a, b) we have shown schematically how the molecules are packed within the terrace.

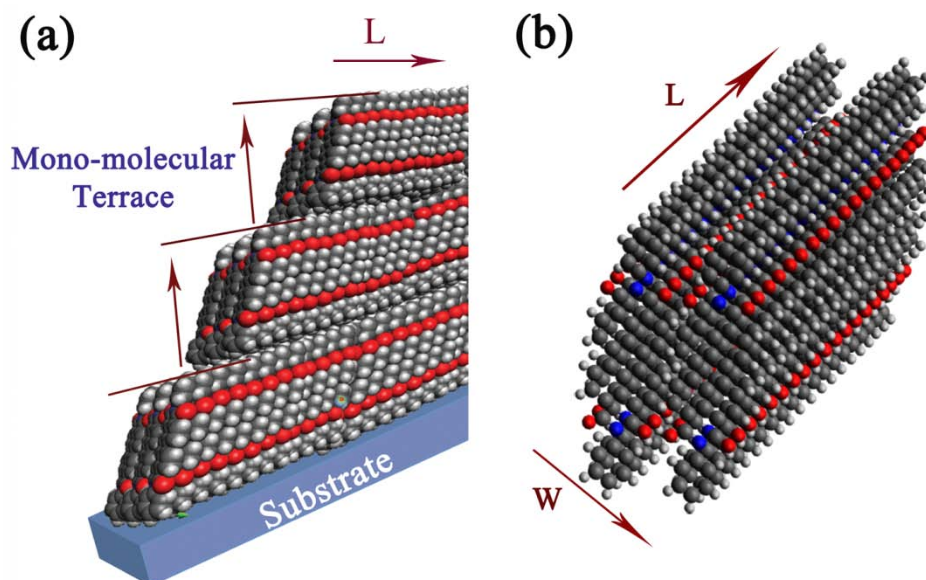

Fig. 5.7: Schematic diagram of (a) showing possible molecular packing within the terrace and (b) growth direction along the length (l) and width (w)is shown as per the molecular packing.

5.3.3 Optical Characterizations

In this section, we discuss the optical properties of PTCDI-Ph molecular structure grown on SiO_2 substrate. Essentially we have studied absorption and luminescence properties.

A. Absorption property

In order to understand the absorption property, we have measured the absorption spectra of the film.[25] A commercial spectrometer (Shimadzu 3010 PC) was used to measure the UV-Vis-NIR absorption spectra of the samples at room temperature. The detail of the instruments is given in chapter II. Here in the Fig. 5.8, we show the typical absorption spectra of PTCDI-Ph.

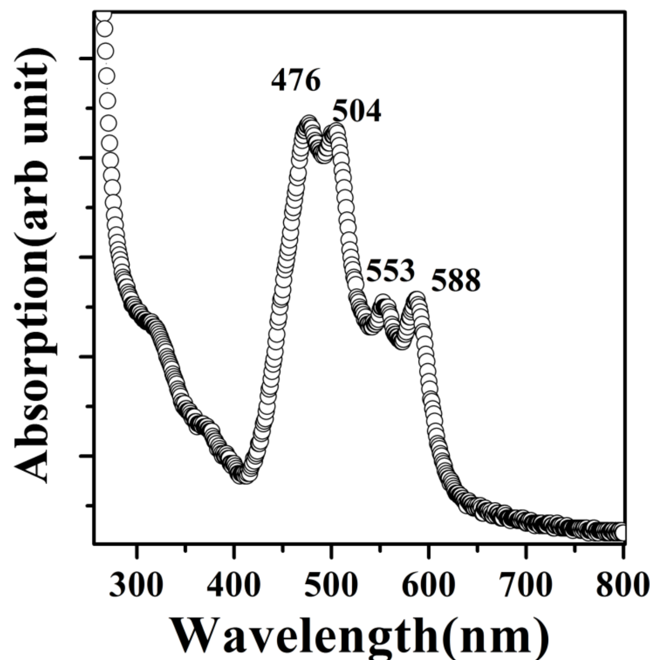

Fig. 5.8: UV-Vis absorption spectroscopy of PTCDI-Ph film.

The absorption spectrum is very similar to the material in solution phase. The main absorption peaks arises at wavelength 476nm and 504nm. These absorption corresponds to π-π* transition.[21, 26-28] Chen et.al. shows that the peaks in the absorption spectra of PTCDI-Ph in DMF solution are at 524, 488 and 457nm.[21] The first two peak positions changed slightly in thin film growth but the peak at 457 nm is not observed in the thin film case. Two other less intense peaks centered at 553 nm and 588 nm appear in the thin film. These peaks may arise due to n-π transition.

B. Photoluminescence properties

The luminescence property of the samples was measurement by Steady-state photoluminescence (PL) (Thermo Spectronic, AB2) using a Xenon lamp source at different excitation wavelengths. The room temperature steady state PL spectra are shown in the Fig. 5.9. Two distinct peaks are

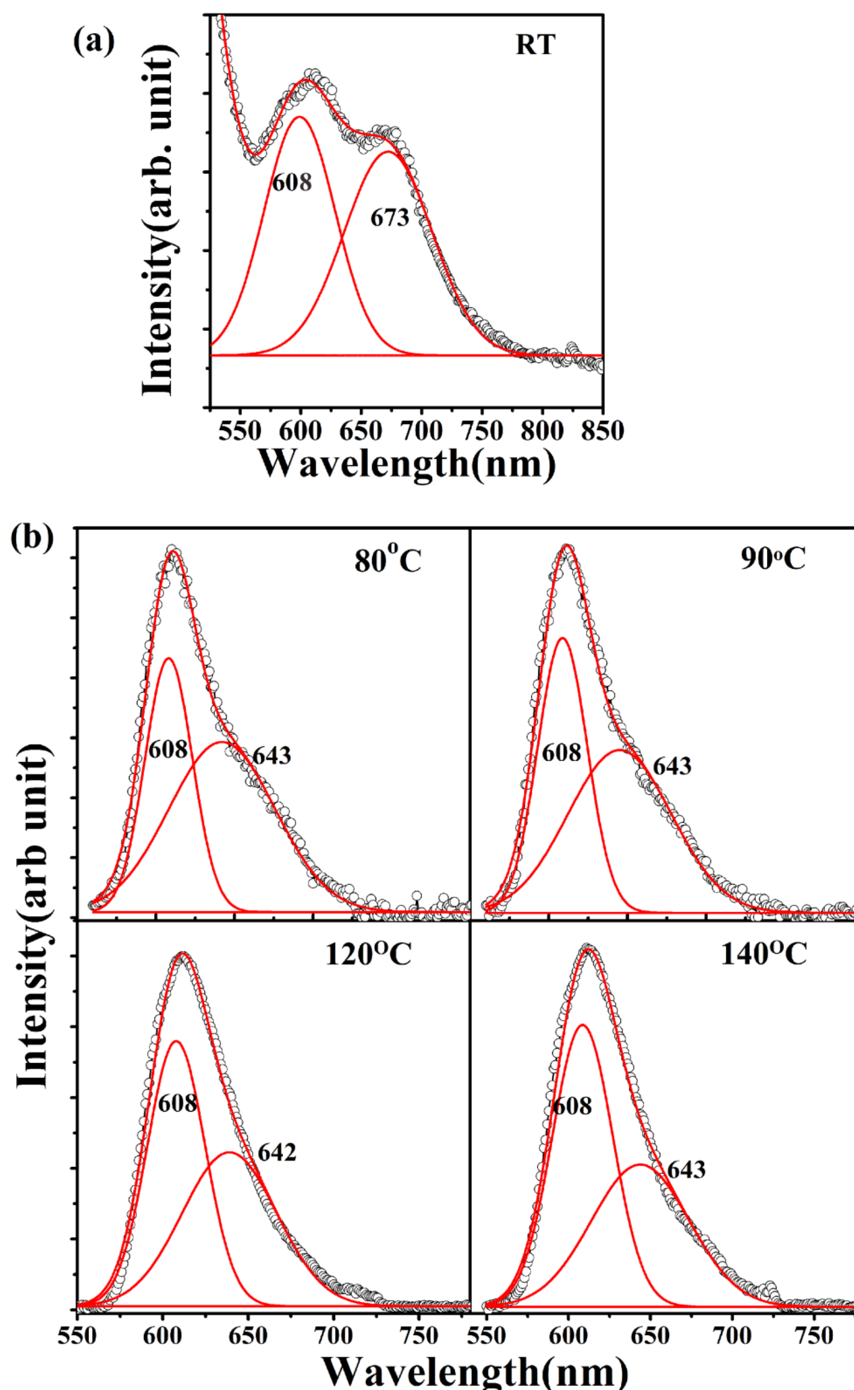

Fig. 5.9: PL spectra of PTCDI-Ph film grown at RT, 80°C, 90°C, 120°C and 140°C. For RT sample two peaks arises at 608 nm and 673 nm, and for all other samples first peak is at 608 nm and second one at ~643 nm.

observed at the wavelength of 608 nm and 673 nm with the excitation wavelength of 475 nm for the sample grown at RT. However, the second peak was not observed for the samples grown at elevated substrate temperature. Furthermore, we have observed another peak at 643 nm

wavelength position. The peak positions were calculated from the Gaussion peak fitting as shown in Fig. 5.9. The ratio of the intensities of these two peaks is calculated and variation of it with respect to substrate temperature is shown in Fig. 5.10. It is clear that the intensity of second peak is decreasing

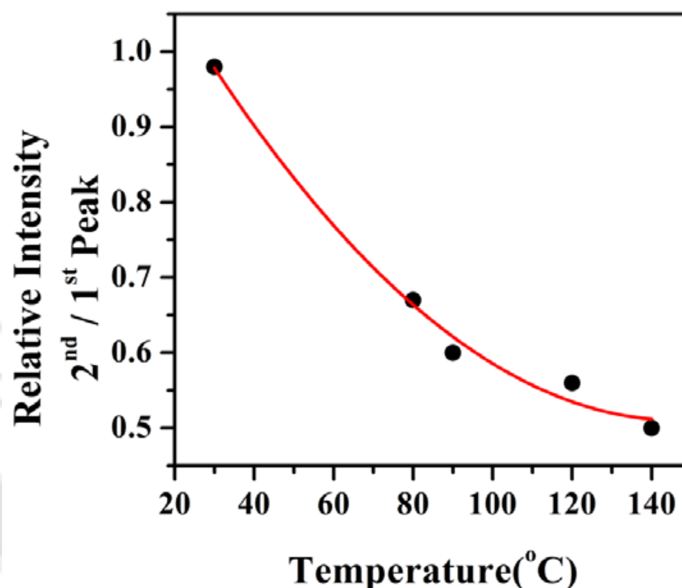

Fig. 5.10: PL intensity variation of the 2nd peak /1st peak with respect to different substrate temperature. With increment of substrate temperature the intensity decreases rapidly.

with substrate temperature. It confirms that the contribution of the state corresponds to 1.93eV observed at 643 nm is decreasing with the substrate temperature. This peak could be representing defect states.

C. Time-Resolved Photoluminescence properties

The steady state PL spectra confirms the presence of two states in the PTCDI-Ph grown film. For further confirmation of the density of the two states, we investigated the lifetime of the excited state and nature of the transition using Time-Resolved Photoluminescence (TRPL) . We studied the PL decay dynamics of the observed band at 640 nm which is shown in Fig. 5.11. We have used 475 nm laser pulse for the excitation using a commercial

fluorimeter (Edinburgh, Life Spec II,) with time resolution better than 50 ps. The decay kinetics of the states at 642 nm is best recovered

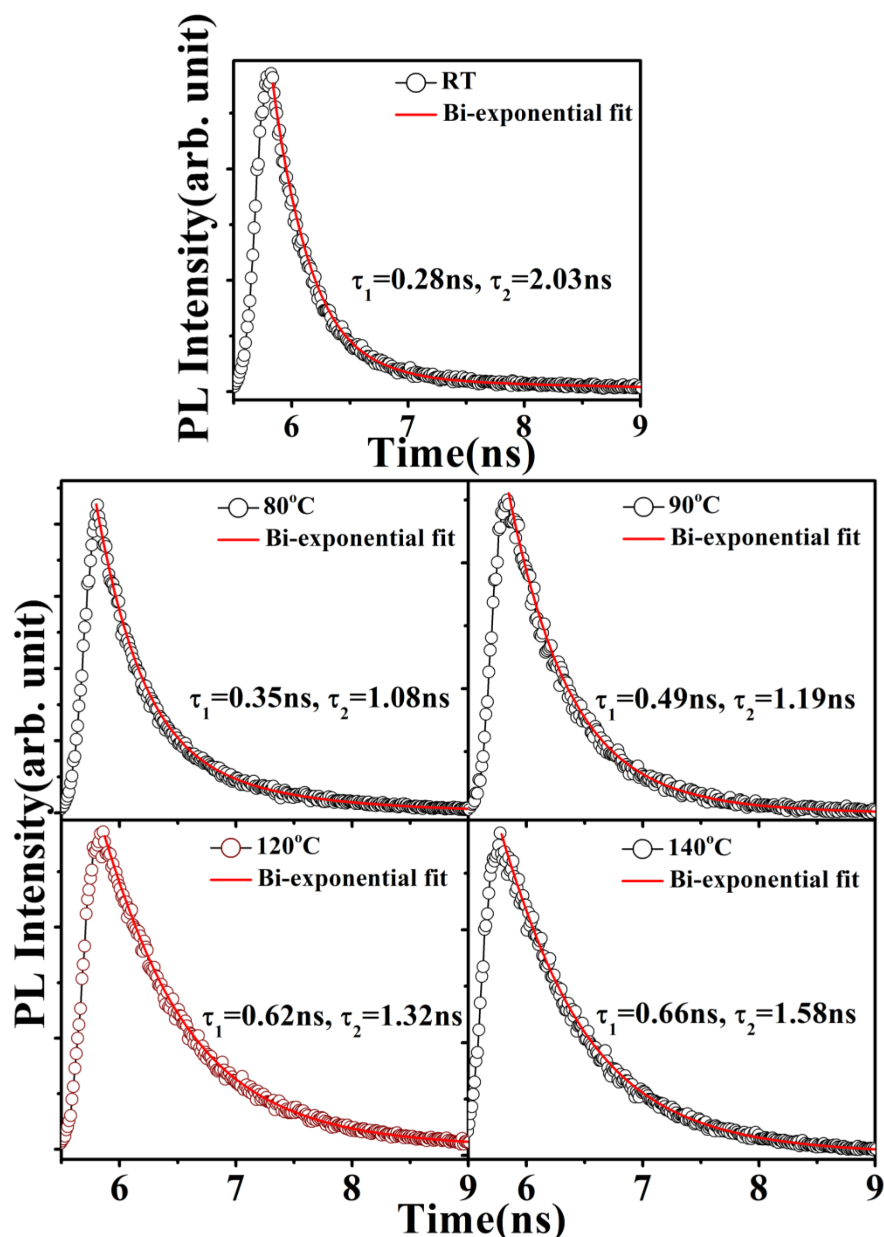

Fig. 5.11: PL decay dynamic spectra of PTCDI-Ph film grown on SiO_2 substrate at room temperature and four elevated temperature. For RT sample decay channel is calculated for 673 nm emission and for all other case 642 nm. Here all the components are fitted by bi-exponential function which is shown by the red line.

by bi-exponential decay function $I=I_0+A_1e^{-t/\tau1}+A_2\ e^{-t/\tau2}$, where τ_1 and τ_2 are the decay time constant. Here 640 nm was chosen to have access of

component of both 608 nm and 643 nm peaks. Therefore, the decay kinetics shows the decay of both the states. Here τ_1 and τ_2 signify the decay of 643 nm and 608 nm states respectively. For RT sample the decay channel is calculated for the emission 673 nm. The first component of the decay time constant is for RT, 80°C, 90°C, 120°C and 140°C are 0.282 ± 0.025 ns, 0.352 ± 0.036 ns, 0.488 ± 0.021 ns, 0.621 ± 0.021 ns and 0.663 ± 0.012 ns, respectively. Interestingly it is found that with the increment of the substrate temperature, the highest contributory component of decay constant (τ_1) is increasing. This signifies that the density of the state corresponding to 640nm emission is decreasing with the increment of substrate temperature. This confirms the result obtained from XRR measurements that the molecular packing improves with substrate temperature. As a result, defect density decreases. Therefore peak originated at 643 nm could be represential defects states. For the case of PTCDA film such behavior of defect states are observed.[29]

5.3.4 Photoresponse of Molecular Terraces

In order to understand the Photoresponse to I-V measurements on their terraces, we have deposited Ag contacts on the films. The typical channel length for this measurement is about 300 μm with contact width is about 1 mm. I-V measurements were carried out both under white light and dark condition. In the Fig. 5.12 we have shown the dark and photocurrent characteristic of thermally grown PTCDI-Ph film. The dark current is seperately shown in the inset of each figure to compare with photocurrent. From the nature of the curve it is clear that up to ~2 volt in both of the cases (Dark and Photo), the current is very small. There is a mismatch of energy of the LUMO state of the PTCDI-Ph (-4.16 eV) and Fermi energy of Ag (-4.52 eV). As a result, there is a formation of extra barrier at then junction due to

band bending. The small current observed up to 2 volt is possibly due to this barrier. We have observed increased dark and photocurrent with substrate temperature. This may be due to the decrease of defect states with increase in substrate temperature.

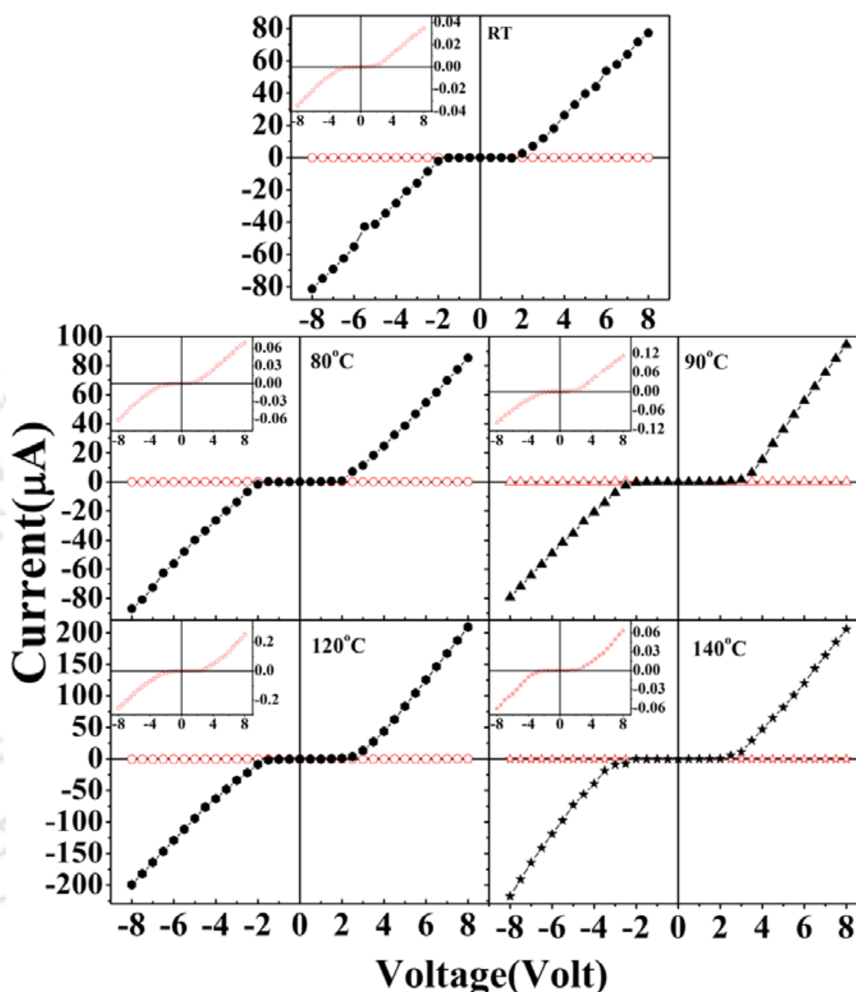

Fig. 5.12: I-V characteristic of PTCDI-Ph grown at RT, 80°C, 90°C, 120°C, 140°C. Each of the inset of the graph shows the enlarged view of dark I-V characteristics. Dark and photocurrent increases with the increasing substrate temperature.

A typical photo current spectra of the sample measured at 4V bias condition is shown in the Fig. 5.13. Broad peaks with intense peak edge at 480 nm arise in the spectra. This broad peak arises due to the band edge

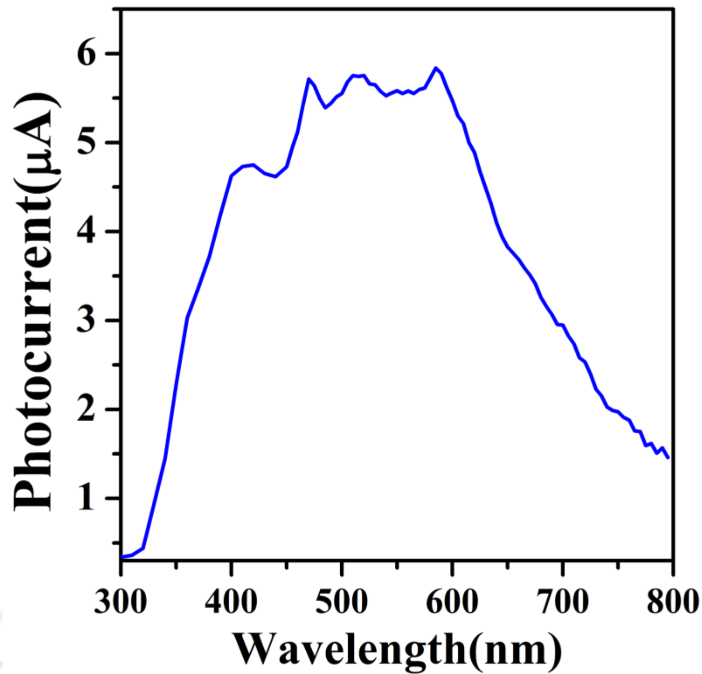

Fig. 5.13: Photocurrent spectra of PTCDI-Ph film grown on SiO_2.

absorption followed by generation of photo carriers (electron-hole pair). The multiple peaks observed in the whole spectra, may arise due to trap or defect state. With the illumination of 150W xenon lamp and intensity of $0.5mW/cm^2$ the photo current increases about 20 times more with respect to dark current. It is clear that the spectra cover the whole visible range. This property of the material can be used to design photo-detector in the visible range.

The photoresponse of the PTCDI-Ph film measured under the excitation of 475nm light is shown in Fig. 5.14. The observed response and reset time

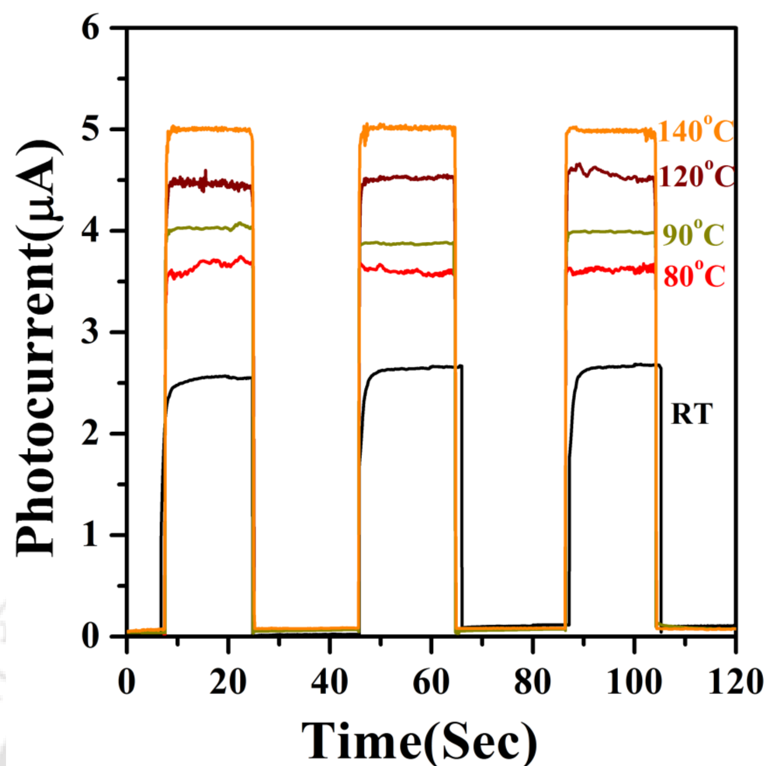

Fig. 5.14: Photoresponse property of PTCDI-Ph film grown on SiO_2 at five different substrate temperatures

of the photoresponse is very fast, as shown in the Fig. 5.15. The maximum photocurrent is increasing with the substrate temperature. This is due to the fact that defect states, which absorb photo carriers, are decreasing at higher temperature as also observed for TCNQ and TTF.[30] Similar fast photoresponse was observed for ZnPc/Py-PDI bi-layer cell[31] and TCNQ, TTF film.[30] In our case the maximum photocurrent was obtained as 2.5mA for RT and 3.62 μA, 4.08 μA, 4.58 μA and 5.14 μA for 80°C, 90°C, 120°C and 140°C respectively. This type of materials with fast photoresponse are suitable for designing optical switch.[30]

5.4 Conclusions

In this chapter, we have studied a comprehensive study of growth kinetics of PTCDI-Ph molecules on SiO_2 substrates. We have calculated the diffusion activation energy for the growth of PTCDI-Ph terraces along the

TH-1132_08612114

length and width of the terraces. Activation energy along the length is 0.21 eV, where as it is 0.34 eV along the width. This observation confirms that molecular interaction along the length of the terraces is stronger than that of along the width. The structural characterization was carried out by means of XRR measurements combining with AFM results. We have found the molecular tilt arrangement, which is about 30° with surface normal, within the film. XRR results also confirm the improvement of molecular arrangement with substrate temperature. That essentially means the defect states due to molecular packing are reduced. Optical characterizations were carried out on the terraces. PL and TRPL measurements confirm the existence of defect states with substrate temperature. This effectively supports the observation from XRR measurements. These molecular terraces show potential for the applications in optical switch. This is because of fast photo response properties of the terraces. Nevertheless, photocurrent spectra covers whole visible range showing great possibility to use this structures as visible range photodetectors.

TH-1132_08612114

5.5 References

1. P. R. L. Malenfant, C. D. Dimitrakopoulos, J. D. Gelorme, L. L. Kosbar, and T. O. Graham, Appl. Phys. Lett. **80**, 2517 (2002).
2. M. M. Shi, H. Z. Chen, and M. Wang, Acta Chim. Sinica **64**, 721 (2006).
3. J. A. A. W. Elemans, R. v. Hameren, R. J. M. Nolte, and A. E. Rowan, Adv. Mater. **18**, 1251 (2006).
4. G. Lu, Y. Chen, Y. Zhang, M. Bao, Y. Bian, X. Li, and J. Jiang, J Am Chem Soc **130**, 11623 (2008).
5. G. Horowitz, Adv. Mater. **8**, 242 (1996).
6. T. Haheider, S. A. Benning, M. W. Lauhof, H. S. Kitzerow, H. Bock, M. D. Watson, and K. Mullen, Mol. Cryst. Liq. Cryst. **413**, 2597 (2004).
7. A. Yakimov and S. R. Forrest, Appl. Phys. Lett. **80**, 1667 (2002).
8. C. W. Tang, Appl. Phys. Lett. **48**, 183 (1986).
9. A. J. Breeze, A. Salomn, D. S. Ginley, B. A. Gregg, H. Tillmann, and H. H. Horhold, Appl. Phys. Lett. **81**, 3085 (2002).
10. R. S. Loewe, K. Tomizaki, W. J. Youngblood, Z. Bo, and J. S. Lindsey, J. Mater. Chem. **12**, 3438 (2002).
11. K. Tomizaki, R. S. Loewe, C. Kirmaier, J. K. Schwartz, J. L. Retsek, D. F. Bocian, D. Holten, and J. S. Lindsey, J. Org.Chem. **67**, 6519 (2002).
12. B. A. Jones, M. J. Ahrens, M.-H. Yoon, A. Facchetti, T. J. Marks, and M. R. Wasielewski, Angew. Chem. Int. Ed. **43**, 6363 (2004).
13. T. Zukawa, S. Naka, H. Okada, and H. Onnagawa, J. App. Phys. **91**, 1171 (2002).
14. P. Ranke, I. Bleyl, J. Simmerer, D. Haarer, A. Bacher, and H. W. Schmidt, Appl. Phys. Lett. **71**, 1332 (1997).
15. J. Z. Sun, Chin. Chem. Lett. **16**, 1201 (2005).

TH-1132_08612114

16. C. W. Struijk, et al., J Am Chem Soc **122**, 11057 (2000).
17. M. P. O'Neil, M. P. Niemczyk, W. A. Svec, D. Gosztola, G. L. Gaines, and M. R. Wasielewski, Science **257**, 63 (1992).
18. M. Schneider, J. Hagen, D. Haarer, and K. Mullen, Adv. Mater. **12**, 351 (2000).
19. J.-M. Lehn, Proc. Natl. Acad. Sci. **99**, 4763 (2002).
20. S. Xu, J. Sun, D. Ke, G. Song, W. Zhang, and C. Zhan, J. Coll. Inter. Sci. **349**, 142 (2010).
21. H. Z. Chen, M. M. Ling, X. Mo, M. M. Shi, M. Wang, and Z. Bao, Chem. Mater. **19** (2007).
22. T. N. Krauss, E. Barrena, D. G. d. Oteyza, X. N. Zhang, J. n. Major, V. Dehm, F. Wu¨rthner, and H. Dosch, J Phys Chem C **113**, 4502 (2009).
23. ImageJ, web: rsb.info.nih.gov/ij/.
24. L. Huang, F. Zhu, C. Liu, H. Wanga, Y. Geng, and D. Yan, Org. Electron. **11**, 195 (2010).
25. Y. Chen, L. Chen, G. Qi, H. Wu, Y. Zhang, L. Xue, P. Zhu, P. Ma, and X. Li, Langmuir **26**, 12473 (2010).
26. M. SilBrai, W. a. Hadel, R. R. Saws, S. Husain, K. Krogh-Jespemn, J. D. Westbrook, and G. R. Bird, J. Phys. Chem. **96**, 7988 (1992).
27. R. A. Cormier and B. A. Gregg, Chem. Mater. **10**, 1309 (1998).
28. S. Xu, J. Sun, D. Ke, G. Song, W. Zhang, and C. Zhan, J. Colloid Interface Sci. **349**, 142 (2010).
29. A. Y. Kobitski, G. Salvan, H. P. Wanger, and D. R. T. Zahn, Appl. Surf. Sci **179**, 209 (2001).
30. B. Mukherjee and M. Mukherjee, Org. Electron. **12**, 1980 (2011).
31. D. K. Susarova, P. A. Troshin, D. Höglinger, R. Koeppe, S. D. Babenko, R. N. Lyubovskaya, V. F. Razumov, and N. S. Sariciftci, Sol. Energy Mater. Sol. Cells **94**, 803 (2010).

TH-1132_08612114

Chapter VI

Self-assembled growth to organic ribbons

6.1 Introduction

In this chapter, we have discussed the study of growth of organic ribbon like structures grown on SiO_2 substrates. Here we used 4 - (4-n, n-dimethylaminophenylethynyl) - n - (2-propynyl) - 1, 8 napthalimide ($^{4\text{-DMAPE}}$NI) molecules to grow these structures. $^{4\text{-DMAPE}}$NI molecules can be stacked with π–π and CH-π interactions along one direction. As results, long ribbon like structures formation is observed. Details growth mechanism is discussed. Optical and electrical properties of the ribbons are also discussed.

6.2 Experimental Details

The $^{4\text{-DMAPE}}$NI molecules were synthesized and subsequently cleaned before we use them for the growth of ribbons by thermal evaporation techniques. The structure of the molecule and the dimensions are shown in Fig. 1.10. The length of the molecule is 16.48Å. The typical base pressure of the evaporation chamber is ~ 10^{-7} mbar. We have used Si(100) substrate with native oxide layer. The substrates were cleaned using methanol, acetone and

TH-1132_08612114

di-ionized water following the standard procedure of cleaning semiconducting substrates which is described in chapter II section 2.1.1. To study the kinetics of the growth, we have used different substrate temperatures such as room temperature (RT), 60°C, 80°C and 100°C. The sublimation temperature of this molecule is found to be 250°C. We have maintained the constant deposition flux of the molecules for all the samples. Morphology and the structure of the grown films is studied using field emission scanning electron microscopy (FESEM, Sigma, Zeiss, Oberkochen, Germany) and transmission electron microscopy(TEM) with selected area electron diffraction (SAED), UV-VIS-NIR absorptions measurements at room temperature were carried out using commercial spectrometer (Shimadzu 3010PC). A micro Raman spectrometer with 488 nm Ar^+ laser (Jobin Yvon, Lab Ram HR800) was used to collect photoluminescence (PL) of the organic structures. Photoluminescence excitation was measured by steady state PL (Thermo Spectronic, AB2) using Xenon Lamp at different excitation wavelengths. A microprobe station was used to study the electrical and opto-electrical properties of the samples. Contacts were made using Ag deposition. Photoresponse was measured using a picometer (Model 6487, Keithley, Aurora Road, Cleveland, Ohio) under the illumination of monochromatic UV light intensity of approximately 0.5mW/cm^2 in ON and OFF conditions. Light was tightly focused on to the sample to make sure that it illuminates the active region of sample between the two contacts. The spectral range of excitation was 350-850 nm.

6.3 Results and Discussions

6.3.1 Study of morphology

$^{4\text{-DMAPE}}$NI molecules were grown on SiO_2 substrate using thermal evaporation technique while substrates were kept at different temperatures

such as RT, 60°C, 80°C and 100°C during the growth. Fig. 6.1 shows the representative SEM images of the above samples. We have observed the

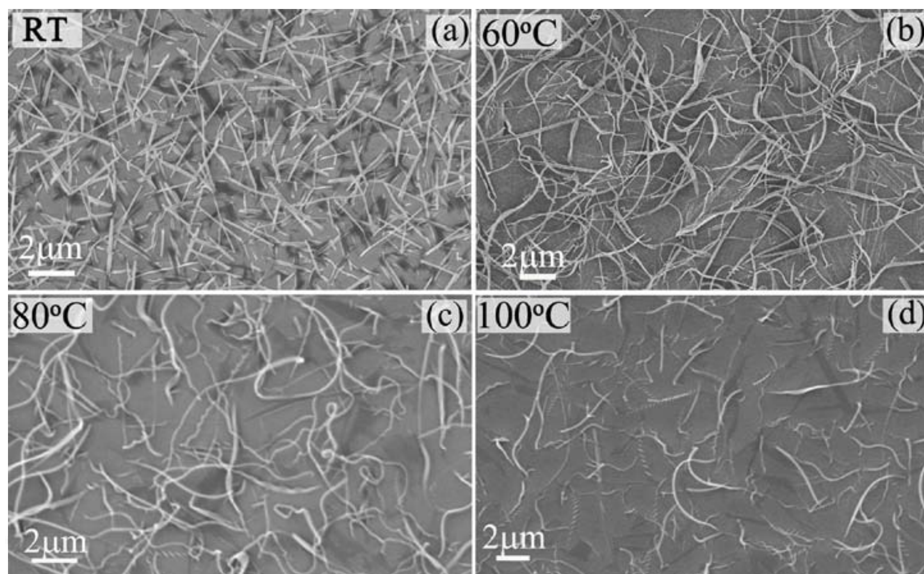

Fig. 6.1: SEM image of $^{4\text{-DMAPE}}$NI ribbon deposited on Si substrate at (a) Room Temperature, (b) 60°C, (c) 80°C and (d) 100°C. All of the cases it forms ribbon type structure.

formation of ribbon like structures, as it is clear from the SEM images. Apparently, the molecules grow a wetting layer on the substrates. The ribbons were formed on top of the wetting layer. However, we can easily see that the length of the ribbons increases with substrate temperature and therefore, the mass transport occurs from the films to the ribbons once the ribbons start forming. The dark areas in the films are essentially the regions from where mass was transported to the nearby ribbons. Fig. 6.2 shows a simple possible growth model to explain how the ribbons were formed. The length of the ribbons was increased with substrate temperature. Due to the increase in substrate temperature, the diffusion of the molecules on the films increases. These molecules could be coming from the effusion cells during the growth or the diffusion of the mass to the ribbons from the films. As a result, the length of the wires increases with substrate temperature. We have measured the evolution of length and width of the ribbons.

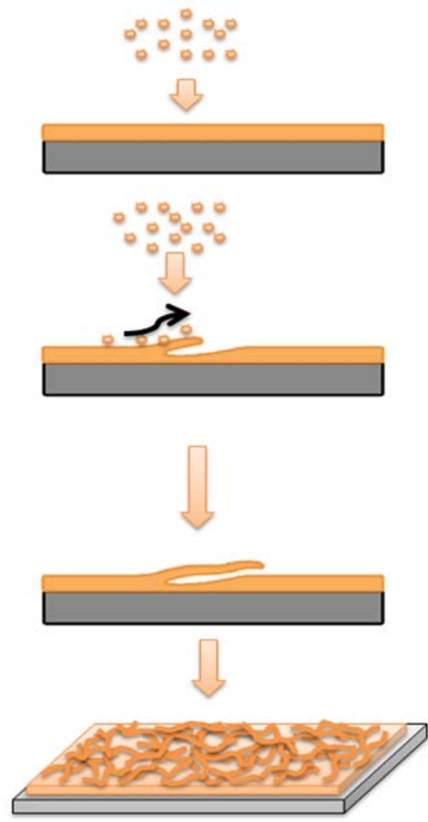

Fig. 6.2 : Schematic diagram showing the growth of organic ribbons.

Fig. 6.3 shows the variation of the length with substrate temperature. It is clear that length

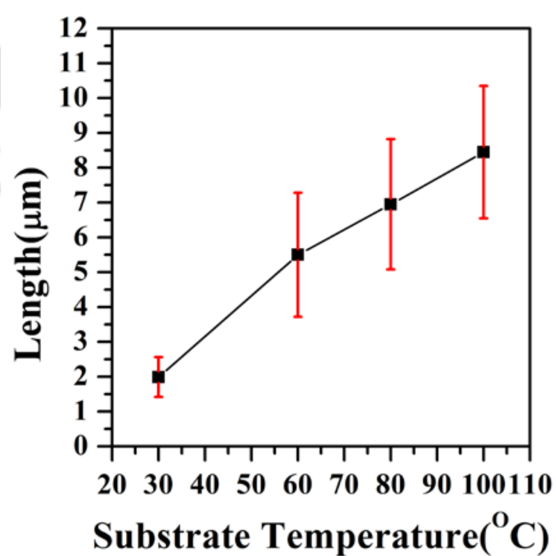

Fig. 6.3: Length variation of the organic ribbon with different substrate temperature. With the increment of substrate temperature the length of the ribbon is increasing.

increases as the substrate temperature increases. We have increased the substrate temperature up to 100°C. This is due to the fact that the desorption of the molecules from the substrate during growth increases and we cannot grow the films beyond 100°C substrate temperature. We have observed the growth of about 8 μm long ribbons at 100°C substrate temperature. However, more interestingly the ribbons did not grow along the width, which is shown in Fig. 6.4. As a result, the ribbons were grown only along

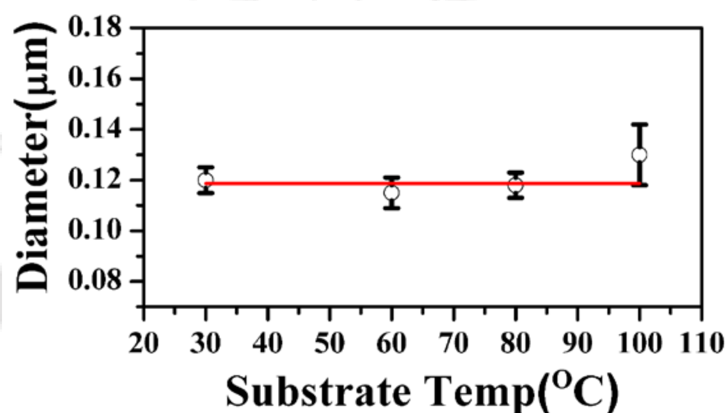

Fig. 6.4: Diameter variation of the ribbon grown at different substrate temperature. The average diameter observed is 0.12 μm.

the length with substrate temperature keeping the width fixed. It is clear from the SEM results that the ribbons are connected with the substrate at one edge. Therefore, the molecules landed onto already formed ribbons can diffuse along the length of the ribbons and the length grows. On the other hand, molecules from the wetting layer can also diffuse to grow length of the ribbons. In order to calculate the activation energy of these diffusion processes, we have used Arrhenius plot of the length (l_r) of the ribbons with respect to temperature as ln(l_r) vs 1/T and calculated the activation energy from the slope as shown in Fig. 6.5. The calculated activation energy for the diffusion of the molecules along the length of the ribbons as well as for the diffusion of the molecules from the wetting layer is 0.21 eV. This values is

TH-1132_08612114

closer the to activation energy found for the diffusion of the organic molecules.[1] Depending upon the bonding nature if we calculate the bonding

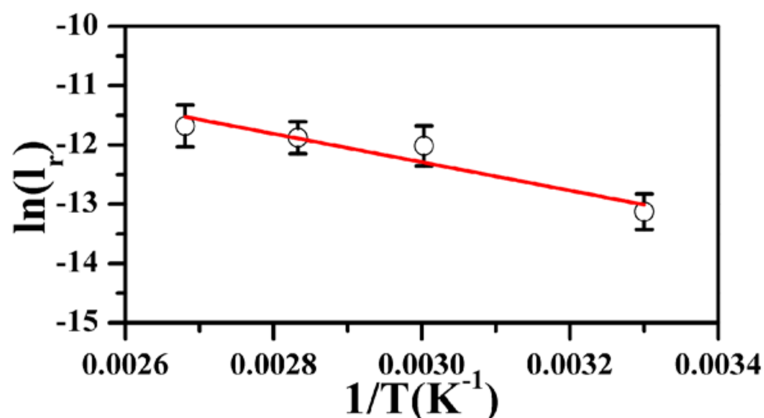

Fig. 6.5: Arrhenius plot of the organic molecule. The activation energy of the molecule is 0.21eV calculated from the slope of the curve.

strength of the molecule in two direction then we can see that in one direction, the bonding strength is more in comparable to other direction. In the Fig 6.6 we show schematically how the molecules are packed in both directions.

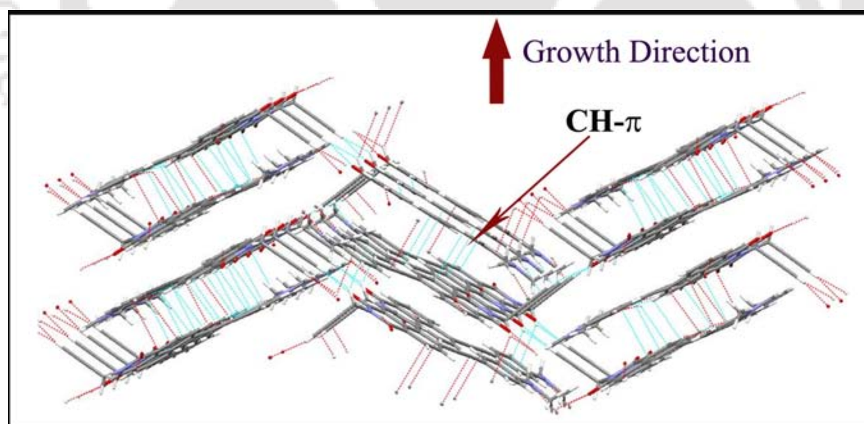

Fig 6.6: Schematic diagram of the molecular packing.

In Fig. 6.7(a) shows the TEM image of the ribbons. Selected area electron diffraction (SAED) taken from the ribbons are shown in Fig. 6.7(b). Sharp diffraction spots confirm that the ribbons are single crystal in nature. We calculated the lattice spacing of the molecules from the diffraction spot is 3.42 Å. The elongated diffraction spots observed in the

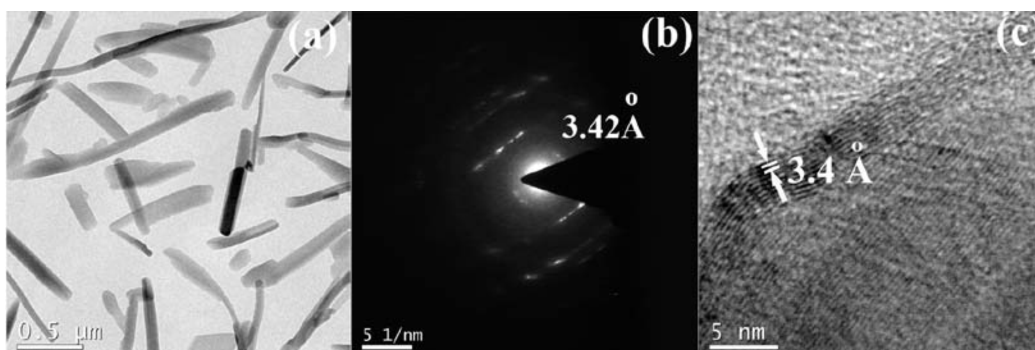

Figure 6.7: (a) TEM image of the nanostructure, (b) SAED pattern of nanostructure and (c) HRTEM of the nanostructure. From the SAED pattern it is clear that ribbons are in crystalline nature.

SAED pattern may be due the overlapping of multiple ribbons. In the high resolution TEM (HR-TEM) the molecular arrangement is clearly visible(Fig. 6.7(c)). The calculated lattice constant confirms the value calculated from the theoretical calculation. In Fig. 6.8 we showed the calculated packing scheme of the molecules. The calculated interlayer spacing obtain from the Fig 6.8 is 3.31Å. This is closer to the value obtain from SAED pattern.

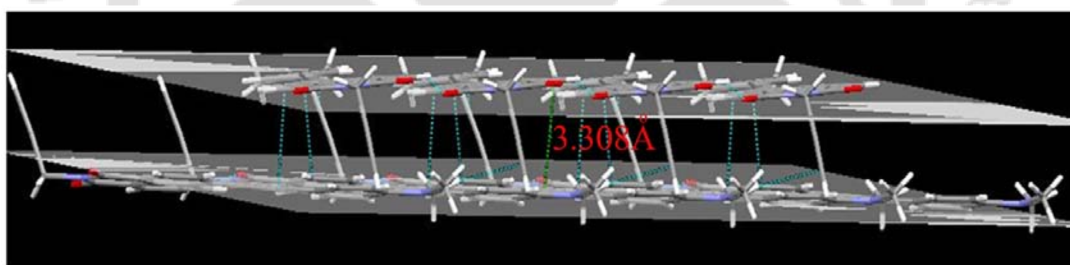

Fig. 6.8: Schematic diagram of the molecular packing. The inter-planer distance for packing from theoretical calculation is 3.31Å

6.3.2 Optical characterizations

In order to study the optical and opto-electrical response of the ribbons we have measured absorption, emission and photocurrent from the samples.[2] Fig. 6.9(a) shows the absorption spectrum. Broad absorption spectrum is

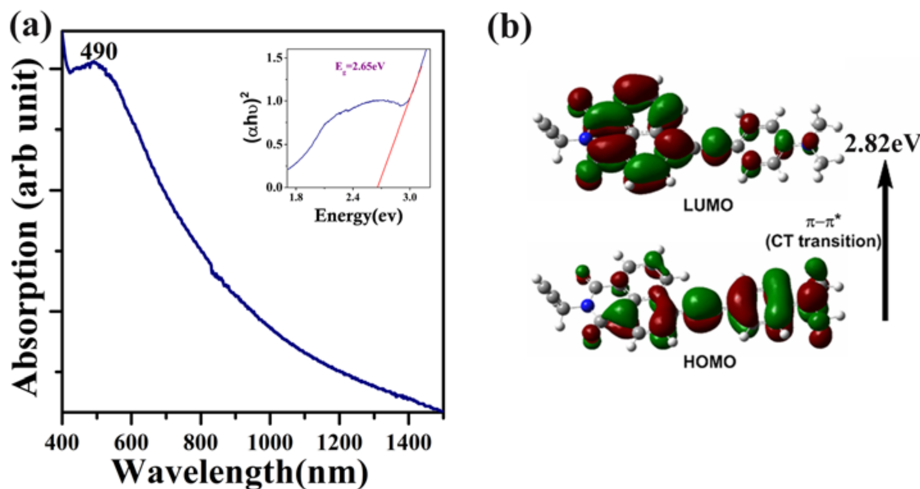

Fig. 6.9: UV/Visible absorption spectra of the self assembled [4-DMAPE]NI ribbons. The absorption peak edge comes around 490 nm.

observed in the UV region centered at 490 nm. The optical band gap obtained from the absorption study is about 2.65 eV. This corresponds to the $\pi-\pi^*$ transition. Fig. 6.9(b) shows the HOMO-LUMO transition levels obtained from the DFT calculations. The calculated value for $\pi-\pi^*$ transition from is about 2.82eV which confirms our measured value.

Using Cyclic voltammetry (CV) analysis for [4DMAPE]NI molecule the energy difference between the lowest unoccupied molecular orbital (LUMO) and the highest occupied molecular orbital (HOMO) are determining the efficiency. The oxidation and reduction of an organic molecule involve electron transfers and CV measurements can be used to determine the potential change during redox process.[3-8] The position of the LUMO level comes from the experiment is -3.568eV.

In Fig. 6.10 (a)-(d) shows the PL spectra collected of the ribbons. A strong emission peak is observed when excited with 488 nm laser source.

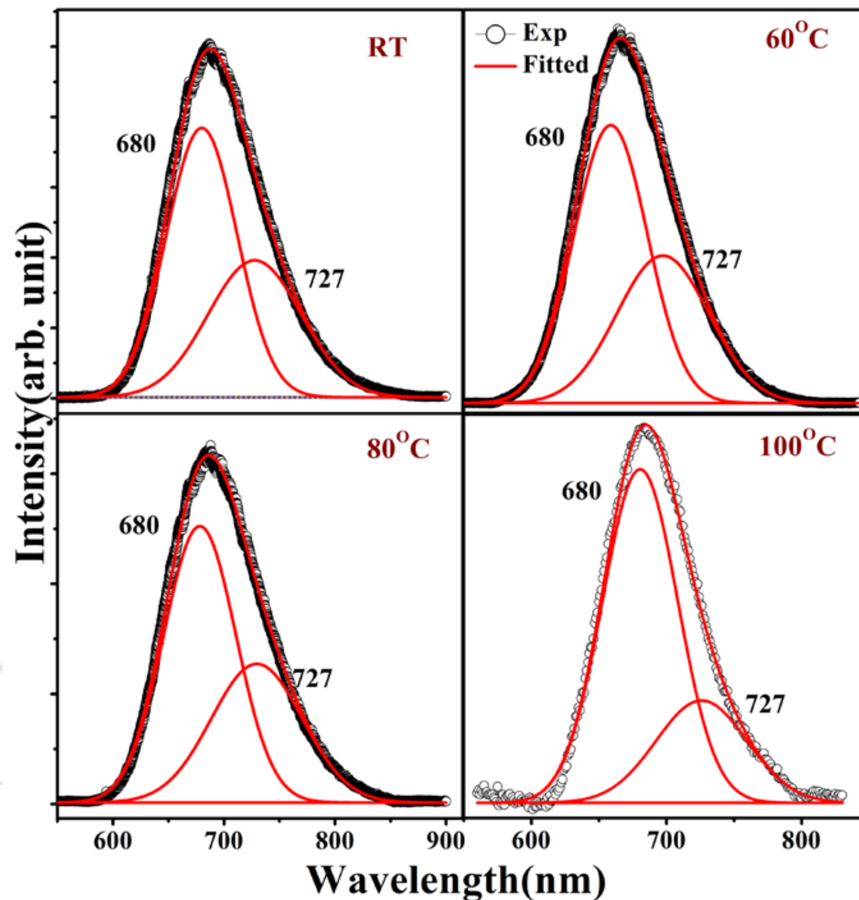

Fig. 6.10: Photo luminescence spectroscopy of Self assembled ribbon grown at (a) RT, (b) 60°C, (c) 80°C and (d) 100°C. The solid lines are the fitted line with Gaussian function.

This peak was de-convoluted by Gaussian function into two peaks. First peak is at 680 nm while the second peak is at 727 nm. The first peak is due to the bound excitonic recombination and the second emission is may be due to the transition into a state generated due to the packing of the molecules.

Fig. 6.11(a) shows the PL intensities I_{680} and I_{727} with substrate temperature. The PL intensity for 680 nm peak is increasing whereas for 727 nm peak is decreasing. We have shown the temperature dependence of PL

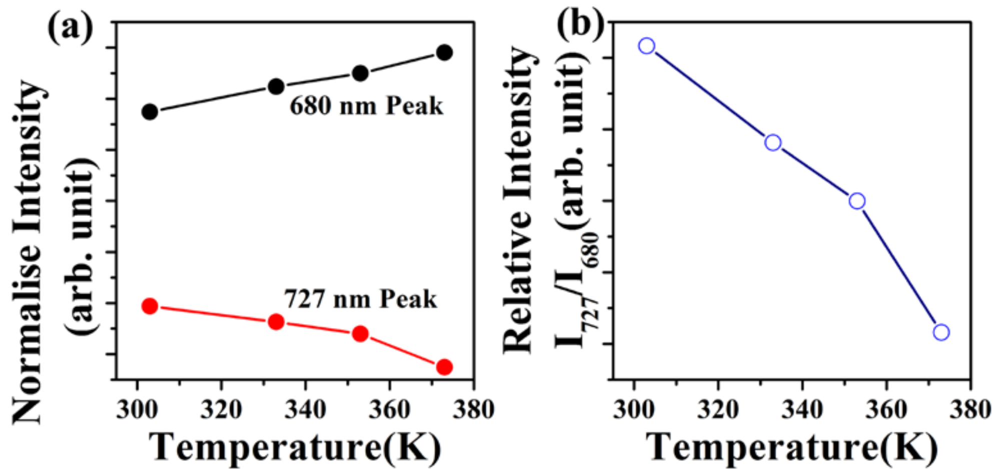

Fig. 6.11: (a) Variation of PL intensity normalized by total intensity for the peaks at 680 nm and 727 nm. In the case of 680 nm peak, intensity is increasing with substrate temperature and for 727 nm peak, intensity is decreasing. (b) relative intensity variation of the intensity for 727 nm and 608 nm peak with different substrate temperature. With temperature increment it is decreasing.

intensity ratio I_{727}/I_{680} in Fig. 6.11(b).[9] PL intensity is essentially proportional to the density of states at the conduction band and transition probability. The ratio I_{680}/I_{727} is decreasing with growth temperature. This indicates that density of states corresponding to the state 727 nm decreases with substrate temperature. This state may be representing the defect states. It is expected to have better molecular arrangements in the ribbon as growth temperature increases and therefore, one can expect to have fewer defects in the ribbons.

We have studied the photoconductivity on the ribbons. Fig. 6.12 (a-b) show the representative dark and photo current taken from the samples grown on RT and 60°C substrate temperature. This clearly shows the huge

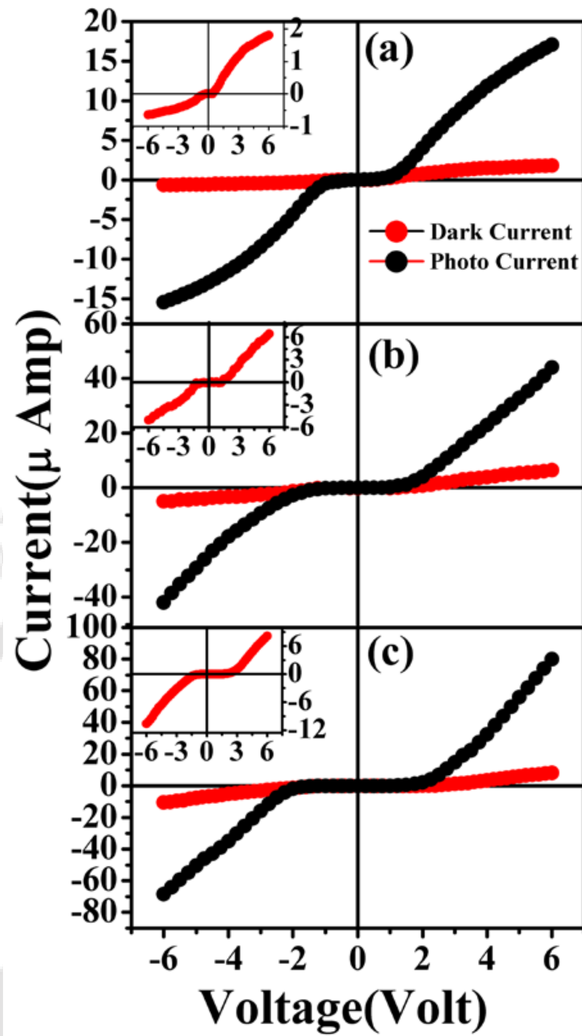

Fig. 6.12: Current-Voltage characterization of Self assembled ribbon grown at (a) RT, (b) 60°C, (c) 80°C, inset of the each graph expanding view of corresponding dark current characteristics.

change in the photo current in compare to dark current after exposing the ribbons into white light. We have observed the similar effect for other samples as well. We have studied the spectral variation of photocurrent to find out the particular wavelength of the light for which maximum photocurrent can be obtained. Fig. 6.13 shows the variation of photocurrent with respect to wavelengths. The measurement was carried out with 4 V bias

TH-1132_08612114

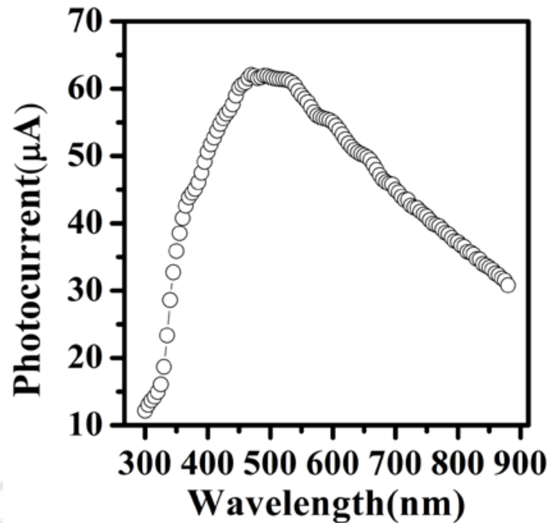

Fig. 6.13: The photocurrent spectra of the $^{4\text{-DMAPE}}$NI ribbons. The peak edge comes around 480 nm.

voltages when we have measureable current. A broad peaks centered at 480 nm was observed. At this wavelength, current increased about 5 fold to its initial value.

We have measured the photocurrent with 480 nm light. Photocurrent measured under this wavelength using ON and OFF mode is shown in Fig. 6.14. We have only measure photocurrent for three samples grown up to 80°C substrate temperature. The significant desorption of the molecules are observed at 100°C and above and therefore, we have used substrate temperature up to 100°C. As a result, the density of the ribbons was very less and photocurrent measurement was not possible to carry out for this samples. When light is ON, photocurrent increases very fast initially and then saturates. When light is OFF, we observed a huge persistence photocurrent[10-13] and it takes about 14 hours to come back to initial current before light was ON. However, Fig. 6.14 shows the data only up to 2.5 hours.

TH-1132_08612114

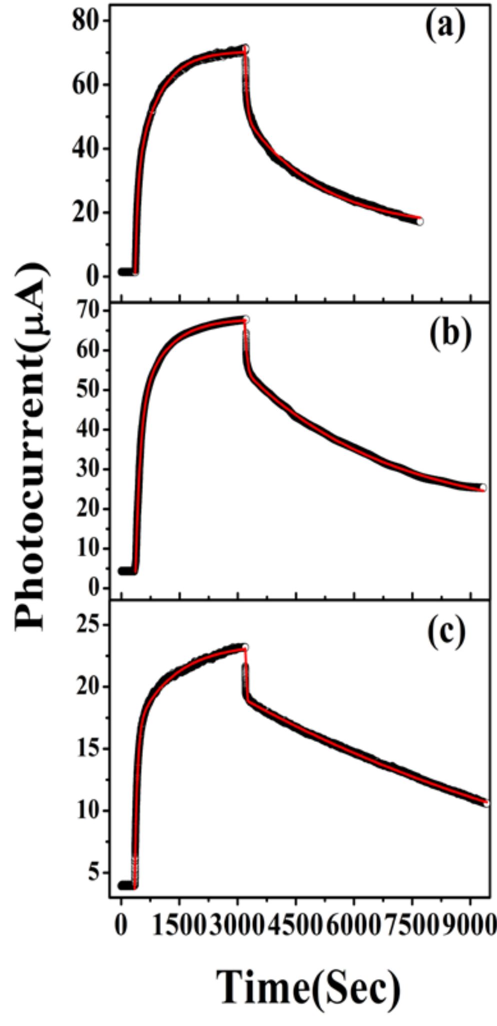

Fig. 6.14: The photocurrent growth and decay behaviors of self assembled growth of $^{4\text{-DMAPE}}$NI nanoribbons grown at (a) RT, (b) 60°C, (c) 80°C . The solid curve is the fitted line. Responses are measured at 4 volt bias and 480 nm wavelength light.

In order to understand the decay and growth of photocurrent, we have used following growth and decay equation to fit photocurrent.

$$\text{Growth:} \qquad I_{ph}(t) = I_1 + A_1(1- e^{-t/\tau 1}) + A_2(1-e^{-t/\tau 2})$$

$$\text{Decay:} \qquad I_{ph}(t) = I_{ph}(\infty) + A_3 e^{-t/\tau 3} + A_4 e^{-t/\tau 4}$$

Where, I_1, A_1, A_2, A_3 and A_4 are positive constant and $I_{ph}(\infty)$ refers to the photocurrent after infinitely long time of decay experiment, which is

essentially is the dark current. The τ_1, τ_2, are the rise time constant and τ_3, τ_4 are the Decay time constant. Fitted parameters are summarized in table 6.1.

Deposition Temperature	Rise Time(Sec)				Decay Time(Sec)			
	τ_1	Error	τ_2	Error	τ_1	Error	τ_2	Error
30°C(RT)	62.87	0.23	594.71	1.31	47.82	0.54	1959.83	10.39
60°C	115.31	0.45	721.61	4.38	46.12	0.49	3792.43	19.65
80°C	64.77	0.25	1030.16	7.90	10.91	0.14	11194.12	78.63

Table 6.1: The growth and decay time constant variation of different sample

There is essentially a rapid process of photo generation and recombination of electron-hole pairs and a slow process of electron capture at the surfaces states. Therefore, we have used two rise time constants in the fitting. When light is off, Two mechanism are involved in the whole process. After illumination the electron-hole pairs are generated. These excited electrons are transferred from heights occupied molecular orbital (HOMO) to the lowest unoccupied molecular orbital (LUMO). As a result we get the certain increment of current. Some of the electrons are captured[14] by trap state[15] which is nearer to LUMO and allow thermal transition from LUMO (or vice versa) and assist an equilibrium process. As a result we get the saturation in current. The transition mechanism is shown by the schematic diagram in Fig. 6.15.

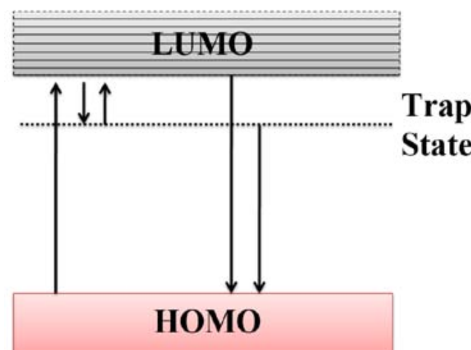

Fig. 6.15: Schematic diagram of the possible transition of electron between HOMO, LUMO and Trap or Donor state.

At the time of light termination the charge carrier in LUMO are captured by the recombination center and increase the capture cross section in HOMO state. As a result we see initially fast decay. As the concentration of the photo-generated holes is less than trapped electrons (equal to the photo-excited electron), the total electron cannot captured by the holes very fast. So the residual trapped electron cannot find the necessary hole for recombination and slowly captured by hole.[16] This is the second component of the decay. As a result huge amount of persistent photocurrent is observed. There are two main factors that contribute high photo persistent current of these nanostructures have been recognized as (1) the large surface-to-volume ratio and the presence of deep level surface trap states in the ribbon greatly prolongs the photo carrier lifetime and (2) reduced dimensionality of the active area in the ribbon shortens the carrier transit time. Combination of long lifetime and short transit time of charge carrier can result in substantial persistence photocurrent.[17-28] Due to large surface-to-volume ratio, the trapping surface states drastically increase the photocurrent. It is expected to increase the current further with the increase of the length of the ribbons.

6.4 Conclusions

In this chapter we have comprehensively studied the growth of $^{4\text{-}DMAPE}$IN organic ribbons on SiO_2 substrates. These molecules are stacked using $\pi-\pi$ and CH-π interactions. As a result, long 1D structures of ribbon shaped are formed. The growth kinetics of formation of the ribbons is studied by controlling the diffusion of the molecules during growth by varying growth temperatures. We have determined the activation energy (0.21 eV) due to the diffusion of the molecules. The mass transport to grow the ribbons essentially contains diffusion of molecules as well as the direct

TH-1132_08612114

mass transport from the wetting layer. Interestingly, the ribbons grow along the length keeping width constant. This could be due the poor inter molecular interaction between molecules along the width of the ribbons. As a result, the growth along the width saturates at a certain width. PL measurements confirm the existence of defects states, which improve with the substrate temperatures. Huge persistent photocurrents are observed from the ribbons. This persistency stays up to 14 hours. This is due the deep level surfaces states, which trap electrons and release them slowly as the discharge channel is also short. Due to higher surface to volume ratio of ribbons, density of these trap states are increases with substrates temperature as length of the ribbons increases along. As a result, persistent current increases with substrate temperature. This shows potential for the applications in optical memory devices. [29, 30]

TH-1132_08612114

6.5 References

1. N. I. Craciun, J. Wildeman, and P. W. M. Blom, Phys Rev Lett **100**, 056601 (2008).
2. B. Mukherjee and M. Mukherjee, Org. Electron. **12**, 1980 (2011).
3. X. Mu, W. Song, Y. Zhang, K. Ye, H. Zhang, and Y. Wang, Adv. Mater. **22**, 4905 (2010).
4. Z. Zhou, J. L. Brusso, and S. Holdcroft, Chem. Mater. **22**, 2287 (2010).
5. L. Perrin and P. Hudhomme, Eur. J. Org. Chem. **2011**, 5427 (2011).
6. M. R. Molla and S. Ghosh, Chem. Mater. **23**, 95 (2011).
7. Z. Chen, Y. Zheng, H. Yan, and A. Facchetti, J Am Chem Soc **131**, 8 (2009).
8. Z. Wei, H. Xi, H. Dong, L. Wang, W. Xu, W. Hu, and D. Zhu, J. Mater. Chem. **20** 1203 (2010).
9. M. Kaneda, K. Orihara, H. Aizawa, T. Katsumata, S. Komuro, and T. Morikawa, in *SICE-ICASE International Joint Conference*, Bexco, Busan, Korea, 2006), p. 1586.
10. J. Z. Li, J. Y. Lin, H. X. Jiang, J. F. Geisz, and S. R. Kurtz, Appl. Phys. Lett. **75**, 1899 (1999).
11. J. S. Brooks, T. Tokumoto, E.-S. Choi, D. Graf, N. Biskup, and D. L. Eaton, J. Appl. Phys. **96**, 3312 (2004).
12. K. Huang and Q. Zhang, Nanoscale Res. Lett. **6**, 52 (2011).
13. P. Lutsyk, K. Janus, M. Mikołajczyk, J. Sworakowski, B. B. ski, and M. Tłaczała, Org. Electron. **11**, 490 (2010).
14. L. X. He, K. P. Martin, and R. J. Higgins, Phys. Rev. B **36**, 6508 (1987).
15. S. Tanida, K. Noda, H. Kawabatab, and K. Matsushigea, Synth. Met **160**, 1574 (2010).
16. H. K. Yadav, K. Sreenivas, and V. Gupta, Appl. Phys. Lett. **96**, 223507 (2010).

TH-1132_08612114

17. R. H. Bube, *Photoelectronic Properties of Semiconductors* (Cambridge University Press, Cambridge, 1992).
18. A. Rose, *Concepts in PhotoconductiVity and Allied Problems* (Interscience Publishers, New York, 1963).
19. J. S. Jie, W. J. Zhang, Y. Jiang, X. M. Meng, Y. Q. Li, and S. T. Lee, Nano Lett. **6**, 1887 (2006).
20. G. J. Hu, L. Zhang, N. Dai, L. Y. Chen, and M. C. Tamargo, Solid State Comm. **111**, 631 (1999).
21. A. Thander and B. Mallik, Solid State Comm. **121**, 159 (2002).
22. S. Karan, D. Basak, and B. Mallik, Current Appl. Phys. **10**, 1117 (2010).
23. S. Mondal and A. K. Raychaudhuri, Appl. Phys. Lett. **98**, 023501 (2011).
24. J. Nayak, J. Kasuya, A. Watanabe, and S. Nozaki, J. Phys.: Condens. Matter **20** 195222 (2008).
25. C. Leighton and I. Terry, Phys. Rev. B **56**, 6689 (1997).
26. P. M. Mooney, J. App. Phys. **67** (1990).
27. R. A. Linke, T. Thio, J. D. Chadi, and G. E. Devlin, Appl. Phys. Lett. **65**, 16 (1994).
28. Z. Rivera-Alvareza, L. Herna´ndez, M. Becerrila, A. Picos-Vegaa, O. Zelaya-Angela, R. Ramı´rez-Bonb, and J. R. Vargas-Garcı´a, Solid State Comm. **113**, 621 (2000).
29. T. W. Kim, Y. Yang, F. Li, and W. L. Kwan, NPG Asia Mater. **4**, 1 (2012).
30. A. Star, Y. Lu, K. Bradley, and G. Gruner, Nano Lett. **4**, 1587 (2004).

Chapter VII

Summary and Conclusions

This thesis has pursued the understanding of growth kinetics and mechanism of technological relevant organic semiconductors of Perylene and Naphthalene derivatives at different dimensionality for optimum implementation into organic devices. Essentially two molecules from Perylene derivatives and one molecule from Naphthalene derivatives were used.

The preparation and characterization of the organic semiconductors forming various architectures was in the focus of this work. By means of atomic force microscopy (AFM) and ex-situ X-ray reflectivity (XRR), the 3D structural properties of Perylene and Naphthalene derivatives thin film growth on SiO_2 and Ag on Si(111)-(7×7) were revealed. The 1D nano ribbons of ^{4DMAPE}NI on SiO_2 substrates with various substrate temperatures were elucidated by the use of scanning electron microscopy (SEM) and transmission electron microscopy (TEM). For the optical and optoelectrical properties, absorption spectroscopy, photoluminescence spectroscopy and photo response measurements were carried out.

TC-PTCDI-C_8 and PTCDI-Ph are the two molecules used in this work from Perylene group. ^{4DMAPE}NI molecule was chosen from Naphthalene

TH-1132_08612114

derivatives. Ag on Si(111)-(7×7) system was considered as a model system where flat-top mound formation was observed as observed in the case of TC-PTCDI-C_8 molecule. We have explored growth of mounds, long terraces and ribbons.

TC-PTCDIC_8 films grown on SiO_2 substrates showed 3D flat-top mound formation at elevated substrate temperature (T=75°C). However, room temperature grown samples do not show any such formation but small grain formation was observed. We have observed stationary to non stationary growth transition followed by 2D layer to 3D mound formation. The thickness of the layer is two molecular layer height with layer thickness is about 18.3Å. Thicker samples show mounds. The molecular layer spacing was calculated from AFM as well as XRR fitting. The vertical growths of the mounds are found to be slower than lateral growth and rate was found to be 0.02. As a result flat-top mound formation was observed.

In order to understand flat-top mound formation, we studied Ag on Si(111)-(7×7) surface which also forms such structures. The formation of this structure is due to the electronic growth by forming quantum well structures within the films. However, TC-PTCDIC_8 mound formation is due to limited diffusion of the molecules by the step edges barrier. The kinetics of the growth of Ag film was studied at room temperature with different coverages. Interestingly, we have observed the rate of vertical growth is slower than lateral growth and the rate in this case is also found to be 0.02 like TC-PTCDI-C_8 mound growth. Faster vertical growth represent in both the cases that the tendency to grow smooth film is higher. However, due to growth kinetics the film becomes rough. Different scaling exponents are calculated for Ag growth. We have observed three different roughness scaling exponents indicating three different growth mechanisms maintaining same growth and dynamic exponents. TC-PTCDI-C_8 and Ag system were

TH-1132_08612114

chosen for comparison as they form similar kinds of surface morphology. However, the growth mechanism for these two systems is completely different. In order to understand the similarity of flat to mound formation, two different system with different growth mechanism were considered.

PTCDI-Ph forms long molecular terraces on SiO_2 substrates at elevated substrate temperature. However, room temperature grown samples do not show any such formation. We have observed the growth of long terrace formation with varying substrate temperature. From the growth kinetics study, we have calculated activation energy for this type of the growth which indicated the higher activation energy along the width at the terraces than along the length. This confirms the unidirectional growth. Structural properties of these terraces are studied by means of XRR and AFM measurements. Photoconductivity measurement is also carried out for the organic flat top island or terraces. This shows the promise to use these structures in optical switching devices.

^{4DMAPE}NI molecules shows the formation of ribbons on SiO_2 substrates. The detailed growth mechanism was studied through molecular packing. The length of the ribbons increases with substrate temperature. This essentially means a possible molecular mass transport into the ribbons. Interestingly, we found that they do not grow width-wise with substrate temperature. Here also we have calculated the activation energy. This ribbons show huge persistent photocurrent. This essentially due to large deep level surface states that capture electrons and release slowly. As a result persistency increases with substrate temperature as length of the ribbons increase.

In this thesis, we have studied the growth kinetics of different self-assembled structures at different dimensionality. Some open questions could be tackled within this work but at the same time, new unsolved questions

TH-1132_08612114

arose which might pave the way to interesting studies in the near future. In the following, some of the most intriguing issues are listed.

In case of flat top mounds, TC-PTCDI-C_8 as well as Ag showed similar relationship with the rate of vertical growth vs lateral growth. This is indeed an interesting observation for flat top mound formation in-spite of different growth mechanisms. However, it would be interesting to find out the physical reasons of such similarities. A theoretical solid on solid model can be proposed to grow flat top mounds to get insight into this observation.

It would be of great interest to understand the detailed growth mechanism of the long terraces of PTCDI-Ph molecules. In order to successfully implement the structures into electronic device fabrication, it would be very important to have the control on the growth of these terraces with specific directionality. For a more comprehensive description of the involved interactions, different substrates might be also employed.

$^{4\text{-DMAPE}}$IN molecules showed promise to be a molecule for opto-electronic application such as organic memory devices, due to huge persistence photocurrent. However, controlled growth of these nanoribbons is necessary to successfully implement the ribbons in to devices. In addition, it would be interesting to understand molecular interactions, which lead to form unidirectional growth with keeping width fixed. In this regards, effect of substrate interaction on the growth could be explored.

TH-1132_08612114